UTS UNIVERSITY OF TECHNOLOGY SYDNEY

Characterisation of High-Temperature Superconducting Material under Rotating Magnetic Fields

by Wafa Ali Soomro

Thesis submitted in fulfilment of the requirements for the degree of

Doctor of Philosophy

under the supervision of Professor Youguang Guo, Associate Professor Hai Yan Lu, and Professor Jian Guo Zhu

University of Technology Sydney
Faculty of Engineering and IT

May 2023

Title of the thesis:

Characterisation of High-Temperature Superconducting Material under Rotating Magnetic Fields

Ph.D. Candidate:

Wafa Ali Soomro

Email: wafa.a.soomro@student.uts.edu.au

Principal Supervisor:

Professor Youguang Guo

Email: youguang.guo-1@uts.edu.au

Co-Supervisor:

Associate Professor Haiyan Lu

Email: haiyan.lu@uts.edu.au

Co-Supervisor:

Professor Jian Guo Zhu

Email: jianguo.zhu@sydney.edu.au

Address:

School of Electrical and Data Engineering

Faculty of Engineering and Information Technology

University of Technology Sydney, 15 Broadway, Ultimo, NSW 2007, Australia

Certificate of Original Authorship

I, Wafa Ali Soomro, declare that this thesis is submitted in fulfilment of the requirements for the award of Doctor of Philosophy, in the School of Electrical and Data Engineering at the University of Technology Sydney.

This thesis is wholly my own work unless otherwise referenced or acknowledged. In addition, I certify that all information sources and literature used are indicated in the thesis.

This document has not been submitted for qualifications at any other academic institution.

This research is supported by the Australian Government Research Training Program.

Signature: Production Note:
Signature removed prior to publication.

Date: 27th May 2023

Acknowledgements

I would like to express my heartfelt gratitude to my supervisor, Professor Youguang Guo, for his unwavering support, guidance, and encouragement throughout my PhD journey. His expertise, feedback and supervision have been instrumental in shaping my research and enabling me to reach this milestone.

I am also deeply grateful to my Co-supervisors, Associate Professor Hai Yan Lu and Professor Jian Guo Zhu for their invaluable feedback, insights, and suggestions that helped me refine my research and improve its quality.

I am fortunate to have collaborated with an outstanding group of colleagues and research collaborators who provided valuable support, stimulating discussions, and intellectual exchange. In particular, I would like to thank Dr. Boyang Shen, and Professor Jianxun Jin for their contributions to my research.

I would also like to thank the Technical Staff of the school, Mr. Brett Lowder, Dr. Mike Zhong, and Dr. Kevin Cook for their assistance in the execution of the experimental work.

I also owe a debt of gratitude to my family and friends, especially my Father, Professor Dr. Akbar Ali Soomro for their unconditional love, encouragement, and support throughout my academic journey. Without their support, this achievement would not have been possible.

Finally, I would like to acknowledge the financial support provided by Faculty of Engineering and IT, and Australian Research Council which enabled me to pursue my Ph.D. studies.

Thank you all for being an integral part of my academic journey.

List of Publications

During my PhD candidature at University of Technology Sydney (UTS), I have published six peer reviewed international scientific articles (4 journal articles and 2 conference articles) from this thesis.

Published:

1. **Soomro, W.A**.; Guo, Y.; Lu, H.; Jin, J.; Shen, B.; Zhu, J. AC Loss in High-Temperature Superconducting Bulks Subjected to Alternating and Rotating Magnetic Fields. Materials 2023, 16, 633. (DOI: https://doi.org/10.3390/ma16020633)
2. **Soomro, W.A**.; Guo, Y.; Lu, H.; Jin, J.; Shen, B.; Zhu, J. Experimental Setup for Measurement of AC Loss in HTS under Rotating Magnetic Field. Energies 2022, 15, 7857. (DOI: https://doi.org/10.3390/en15217857)
3. **Soomro, W.A**.; Guo, Y.; Lu, H.; Jin, J.; Shen, B.; Zhu, J. Numerical Investigation of High-Temperature Superconducting-Coated-Conductors Subjected to Rotating Magnetic Fields. Solids 2022, 3, 569-577. (DOI: https://doi.org/10.3390/solids3040036)
4. **Soomro, W.A**.; Guo, Y.; Lu, H.; Zhu, J.; Jin, J.; Shen, B. Three-Dimensional Numerical Characterisation of High-Temperature Superconductor Bulks Subjected to Rotating Magnetic Fields. Energies 2022, 15, 3186. (DOI: https://doi.org/10.3390/en15093186)
5. **Soomro, W. A**., Guo, Y., Lu, H. Y., & Jin, J. X. (2020, October). Advancements and Impediments in Applications of High-Temperature Superconducting Material. In 2020 IEEE International Conference on Applied Superconductivity and Electromagnetic Devices (ASEMD) (pp. 1-4). IEEE. (DOI: https://doi.org/10.1109/AUPEC52110.2021.9597734)
6. **Soomro, W. A**., Guo, Y., Lu, H. Y., Zhu, J. G., Jin, J. X., & Shen, B. (2021, September). Numerical Investigation of AC Loss in HTS Bulks Subjected to Rotating Magnetic Fields. In 2021 31st Australasian Universities Power Engineering Conference (AUPEC) (pp. 1-5). IEEE. (DOI: https://doi.org/10.1109/AUPEC52110.2021.9597734)

Abstract

High-temperature superconducting (HTS) materials enables the development of compact, lightweight, and efficient electrical machines, leading to significant size reduction and improved machine efficiency. A wide range of applications, including superconducting motors, generators, transformers, and technologies like superconducting fault current limiters and superconducting magnetic energy storage, have been explored. However, the commercialization of HTS technology faces challenges due to dissipative interactions occurring when these materials are exposed to alternating magnetic fields. This results in AC loss, also known as power dissipative loss, caused by the displacement of vortices within the material. This power dissipation can impose additional strain on cryocoolers. Factors such as geometric structure, magnetic field orientation, and current density distribution significantly impact this power dissipation. Thus, it is crucial to thoroughly study and characterize the electromagnetic behaviour of HTS bulk materials to ensure the feasibility of commercial superconducting applications. HTS materials only exhibit superconductivity at cryogenic temperatures, necessitating the inclusion of cryogenic cooling units, also known as cryocoolers, in practical and commercial applications. However, AC loss can compromise the stability of cryogenic systems and affect overall device efficiency. Therefore, a comprehensive understanding of the AC loss process and magnitude is essential for the design of new superconducting machines. While most studies have focused on measuring AC loss in one-dimensional alternating magnetic fields generated by transport currents or external magnetic excitations, this study investigates the properties of HTS materials, particularly AC loss, under rotating magnetic fields. Numerical modelling techniques based on finite element analysis (FEA) and H-formulation are employed to analyse the fundamental electromagnetic properties of HTS bulk materials and conductors. The study presents color-coded maps illustrating flux density distribution and examines the demagnetization of HTS-trapped field magnets under rotating magnetic fields. Moreover, a novel experimental setup is introduced to measure AC loss in HTS materials under rotating magnetic fields. The experimental results are compared with those obtained from FEA-based H-formulation, demonstrating consistency between them. The study also explores AC loss under various scenarios, such as different amplitudes and frequencies, and finds that losses are higher under rotating magnetic fields compared to one-dimensional alternating fields. The findings of this study provide a comprehensive understanding of the material properties of HTS when subjected to rotating magnetic fields, offering insights into the design of large-scale HTS applications. The results are valuable for

further characterizing HTS materials and designing cryogenic cooling systems for HTS machines, advancing the practical implementation of HTS technology.

Table of Contents

List of Figures

List of Tables

Abbreviations

HTS	High-Temperature Superconductors
CCs	Coated conductors
AC Loss	Alternating current loss
1D	One-dimensional
2D	Two-dimensional
3D	Three-dimensional
LTS	Low-Temperature Superconductors
YBCO	Yttrium barium copper oxide
BSCCO	Bismuth strontium calcium copper oxide
1G	First generation
2G	Second generation
DC	Direct current
HFCL	HTS fault current limiter
SMES	Superconducting magnetic energy storage
MW	Mega watt
LSM	Linear synchronous motor
SMC	Soft magnetic composite
PDE	Partial differential equations
FEA	Finite element analysis
FEM	Finite element method
SQUIDS	Superconducting quantum interference devices
LN2	Liquid Nitrogen
IBAD	Ion beam assisted deposition
SST	Square specimen tester
VSM	Vibrating sample magnetometers
RSM	Root mean square
FPGA	Field-programmable gate array
UTS	University of Technology Sydney

Note: Abbreviations that are not listed are explained where they appear first.

Nomenclature

B	Magnetic flux density
H	Magnetic field strength
μ_0	Permeability of vacuum
ρ	Resistivity
χ	Susceptibility
λ	Penetration depth
E	Electric field
m_s	Free carrier mass
n_s	Number of super-electrons per unit volume
J	Current density
B_a	External applied magnetic flux density
θ	Phase power factor
ξ	Coherence length
B_{c1}	Lower critical field
B_{c2}	Upper critical field
κ	Ginzburg-Landau parameter
F_L	Lorentz force
J_c	Critical current density
T_c	Critical Temperature
M	Magnetisation
K_H	Coil coefficient of H sensing coil
V_H	Voltage induced in H sensing coil
V_{B_i}	Voltage induced in B sensing coil
K_B	Coil coefficient of B sensing coil
A_H	Cross-sectional area
P_r	Rotational core loss
P_t	Total core loss
P_h	Hysteresis loss
ρ_m	Mass density
H_a	Applied magnetic field strength
μ_r	Relative permeability

E_0	characteristic electric field
Q	AC loss
J_{c0}	Critical current density
n	Numerical model power factor
$B_{1D(alt)}$	One-dimensional alternating field
$B_{2D(rot)}$	Two-dimensional rotating magnetic field
B_0	amplitude of the magnetic flux density
ω	Angular frequency
$\emptyset$	Phase shift
$\Omega\ SC$	Superconducting domain
$\Omega\ NSC$	Non-superconducting domain
H_m	Maximum field strength

Note: Symbols that are not listed are explained where they appear first.

CHAPTER 1 **Introduction**

1.1 Background and Significance

Recently, there have been significant advancements in the manufacturing and commercial availability of long lengths of High-Temperature Superconducting (HTS) materials [1.1]. This progress has fuelled the utilization of HTS materials in various large-scale power applications such as motors [1.1], transformers [1.2], fault current limiters [1.3], power cables [1.4], maglev trains [1.5], wind generators [1.1], and ship propulsion [1.6]. HTS materials offer the potential for increased machine efficiency and substantial size reduction, enabling the design of compact, lightweight, and efficient electrical machines [1.2]. The discovery of high-temperature superconductivity more than three decades ago paved the way for extensive research on utilizing HTS materials in the development of cutting-edge electric power appliances, aiming to replace conventional ones. This includes novel devices like superconducting magnetic energy storage and superconducting fault current limiters [1.3]. The exceptional current-carrying capability of HTS coated-conductor wires, with nearly zero loss in DC and low losses in AC conditions, makes them a feasible choice for developing electric devices with reduced dimensions, lighter weight, and higher efficiency. Continuous research on material properties and advancements in manufacturing technologies have resulted in the availability of high-quality HTS wire in long lengths from multiple manufacturers, which has further accelerated efforts towards the commercialization of HTS devices.

From the design perspective, all the HTS machines are designed and built based on a high magnetic field achieved by either superconducting coils or windings. Conversely, the use of superconducting wire in power system applications is problematical due to dissipative interactions which occurs during the exposure of superconductor to an alternating magnetic field or currents. This phenomenon is referred as superconducting alternating current (AC) loss, which is produced by the motion of vortices inside the superconducting material [1.7]. The AC loss is generally categorised as ‘magnetisation loss’ which is purely magnetic hysteresis behaviour of superconductor, ‘transport loss’ which dissipates when alternating transport current imposes an alternating self-field on a conductor in the absence of an applied field.

Furthermore, while designing practical and commercial applications, a cryogenic cooling unit or a cryo-cooler is installed which extracts the corresponding heat load for maintaining a constant temperature during the process. In contrast, the AC losses can complicate the stability of the cryogenic system, which affects the overall efficiency of the

device. Therefore, a deep understanding of mechanism and magnitude of AC losses is enormously important for the design and development of new superconducting machines.

AC loss can be referred as the core loss, power loss or energy loss or simple energy waste when electrical power is dissipated in the form of heat due to the change in the magnetic field [1.8]. Therefore, it is important to predict the losses in order to design high-efficiency electrical machines. In case of a rotating electrical machines the magnetic field varies with time in the three-dimensional space [1.9], which leads to a complexity in estimation of core loss as there is a presence of alternating and rotating magnetic field at the same time [1.10]. It is reported that the rotating magnetic field can be the major contributor in rotational core losses of electrical machines and the amount of this loss may be about two times of the alternating core loss [1.11].

Previously, all the HTS measurements and modellings of properties were considered under one-dimensional (1D) alternating AC magnetic fields by either the transport current or from external excitations. Therefore, this research mainly focuses on the effect of 2D and 3D rotating magnetic fields on the HTS properties, such as hysteresis and overall AC losses.

1.2 Aims and Objectives

The aim of this research is to characterise the properties of high-temperature superconducting material for the design of high-performance electromagnetic devices like transformers and rotating electrical machines. Following are the objectives of the research.

1. To analyse and theoretically understand the physical mechanism and mathematically characterise the HTS properties for the design of high-performance electrical appliance.
2. To modify the existing 2D magnetic measurement system at UTS for HTS property measurement.
3. To systematically measure the electromagnetic properties of HTS materials under various 1D alternating and 2D rotational flux density patterns.

1.3 Research Contributions

This research will contribute to an important gap in the knowledge with the property characterisation of high-temperature superconducting (HTS) materials under two-dimensional (2D) rotational magnetic field. Most researchers have only concentrated their studies under material properties under one-dimensional (1D) alternating magnetic field, but no one has

investigated the 2D rotational magnetic properties of HTS materials so far. The study focuses on analysing and characterizing the basic electromagnetic properties of HTS bulk using numerical modelling techniques. The study investigates the behaviour of HTS material when exposed to rotating magnetic fields in different planes, and presents the typical current density distribution, AC loss distribution, and demagnetisation. A systematic investigation of AC loss is performed by numerical modelling technique and HTS bulk samples are subjected to various alternating and rotating flux density patterns. The electromagnetic behaviour of HTS CCs is also studied by applying rotating magnetic fields to the stack of HTS CCs. The study presents a new experimental setup for measuring AC loss in HTS material when exposed to rotating magnetic fields, and the results are compared with the modelling results. A detailed investigation of AC loss measurement under various scenarios is performed and the results are analysed at different frequencies. The results show that the losses are higher in the case of exposure under rotating magnetic fields and will be helpful in designing future large-scale HTS applications.

1.4 Thesis Structure

There are total eight chapters of this thesis. A brief outline of each chapter is described as follows:

Chapter 1 presents the background of the study, which highlight the importance of the research topic and contributions.

Chapter 2 presents a detailed literature survey on the previous works in the research area. The chapter also includes theoretical concepts and applications of superconductivity. Furthermore, the concept of the AC loss is also elaborated along with different ways to measure the loss in the superconductors.

Chapter 3 presents a theoretical background and of the numerical modelling using finite element-based H-formulation. The methodology of the two-dimensional and three-dimensional numerical models is also presented.

Chapter 4 presents a detailed numerical investigation of the AC loss in HTS bulks under rotating magnetic fields, where the HTS sample is exposed to various rotating magnetic flux density vectors in XOY, YOZ and XOZ planes.

Chapter 5 presents a numerical investigation of AC loss in HTS coated conductors. A homogenous bulk model is used to perform the numerical analysis where the physical layers of the tape is washed out.

Chapter 6 presents a new experimental technique to measure the AC loss in superconductors under rotating magnetic fields. In this study, an existing singe sheet tester is modified and proposed to be used for the AC loss measurement.

Chapter 7 presents an experimental investigation of AC loss in HTS sample under the rotating magnetic fields. Two different specimens are used to compare the AC loss in HTS samples.

Lastly, Chapter 8 presents the conclusion of the study, challenges and impediments in the research and future research directions.

1.5 References

[1.1] U. Bong *et al.*, "A design study on 40 MW synchronous motor with no-insulation HTS field winding," *IEEE Transactions on Applied Superconductivity,* vol. 29, no. 5, pp. 1-6, 2019, doi: 10.1109/TASC.2019.2908548.

[1.2] J. X. Jin *et al.*, "Enabling high-temperature superconducting technologies toward practical applications," *IEEE Transactions on Applied Superconductivity,* vol. 24, no. 5, pp. 1-12, 2014, doi: 10.1109/TASC.2014.2346496.

[1.3] J. X. Jin *et al.*, "HTS power devices and systems: principles, characteristics, performance, and efficiency," *IEEE Transactions on Applied Superconductivity,* vol. 26, no. 7, pp. 1-26, 2016, doi: 10.1109/TASC.2016.2602346.

[1.4] D. I. Doukas, "Superconducting transmission systems: review, classification, and technology readiness assessment," *IEEE Transactions on Applied Superconductivity,* vol. 29, no. 5, pp. 1-5, 2019, doi: 10.1109/TASC.2019.2895395.

[1.5] D. Fangliang, Z. Huang, Q. Derong, H. Luning, W. Wei, and J. Zhijian, "Design and analysis of a small-scale HTS magnet used in a linear synchronous motor for future high-speed superconducting maglev applications," in *Proceedings of 2018 IEEE International Conference on Applied Superconductivity and Electromagnetic Devices (ASEMD)*, 2018: IEEE, pp. 1-2.

[1.6] H. Moon, Y. Kim, H. Park, M. Park, and I. Yu, "Development of a MW-class 2G HTS ship propulsion motor," *IEEE Transactions on Applied Superconductivity,* vol. 26, no. 4, pp. 1-5, 2016, doi: 10.1109/TASC.2016.2536660.

[1.7] M. D. Ainslie, C. W. Bumby, Z. Jiang, R. Toyomoto, and N. Amemiya, "Numerical modelling of dynamic resistance in high-temperature superconducting coated-conductor wires," *Superconductor Science and Technology,* vol. 31, no. 7, p. 074003, 2018/06/06 2018, doi: 10.1088/1361-6668/aac1d3.

[1.8] H. Toda, K. Senda, and M. Ishida, "Effect of material properties on motor iron loss in PM brushless DC motor," *IEEE Transactions on Magnetics,* vol. 41, no. 10, pp. 3937-3939, 2005.

[1.9] Y. Guo, J. Zhu, D. Dorrell, H. Lu, and Y. Wang, "Development of a claw pole permanent magnet motor with a molded low-density soft magnetic composite stator core," in *Proceedings of 2009 IEEE Energy Conversion Congress and Exposition*, 2009: IEEE, pp. 294-301.

[1.10] Y. Okada and H. Dohmeki, "Examination about the stator structure of the brushless DC motor manufactured in the soft magnetic composite," in *Proceedings of 2009 International Conference on Electrical Machines and Systems*, 2009: IEEE, pp. 1-4.

[1.11] H. Huang, C. Zhang, and S. Yan, "Calorimetric measurement of AC losses of superconducting magnet," *Acta Physica Temperature Humilis Sinica,* vol. 3, no. 1, pp. 42-46, 1981.

CHAPTER 2 **Literature Review**

2.1 Superconductivity

The discovery of superconductivity dates back to April 8th, 1911, when Heike Kamerlingh-Onnes was studying the resistance of solid mercury at very low temperatures. He used liquid helium to cool the mercury [2.1]. At 4.2 K, he discovered that the resistance of the solid mercury suddenly vanished at that temperature [2.1-2.3]. Since that time, there has been a growing interest in superconductivity as it offers answers to a wide range of problems. In recent years, significant progress has been made in the field of current engineering applications, including superconducting motors, superconducting transmission lines, current limiters, and magnetic resonance imaging (MRI).

2.1.1 Meissner Effect

The Meissner effect was first observed by Walther Meissner and Robert Ochsenfeld [2.4] in 1933, twenty-two years after the discovery of superconductivity by Kamerlingh-Onnes. This phenomenon is known as the Meissner effect, which states that a superconducting metal never permits a magnetic flux density to reside within its structure [2.4]. Meissner's effect is not consistent with the theoretical ideal conductor's behaviour ($\sigma = \infty$).

Figure 2.1 provides an in-depth contrast between a perfect conductor and a superconductor. The magnetic behaviour of a perfect conductor is shown in the left (red) box, whereas that of a superconductor is shown in the right (green) box. Starting with (a) and (b), a specimen has no resistance when no magnetic field is present; (c) a magnetic field is applied to the specimen; (d) the magnetic field is removed; (e) and (f) the specimen has no resistance when a magnetic field is applied; (g) the applied magnetic field is removed. It can be shown that a perfect conductor and a superconductor are both capable of expelling the magnetic field from the interior geometry of the material when the sample is cooled before the application of the magnetic field (this is referred to as zero field cooling) [2.4]. In contrast, if a magnetic field is applied to a specimen before cooling, an ideal conductor will retain the magnetic field within its geometry after cooling, while a superconductor will still expel the magnetic field from its inner geometry once the sample has been cooled below its T_c. The Meissner effect is responsible for the magnetic expulsion in a superconductor, while Lenz's law is responsible for the magnetic expulsion in a perfect conductor.

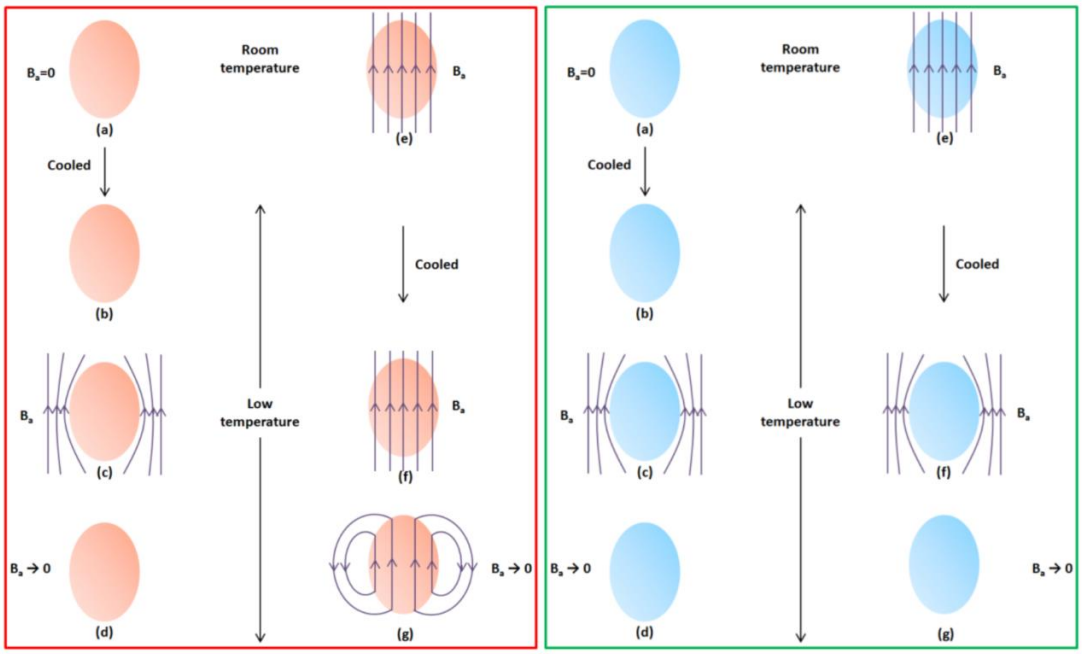

Figure 2.1 (Left) Magnetic behaviour - a perfect conductor. (Right) Magnetic behaviour - a superconductor [2.4]

The Meissner Effect, which involves the expulsion of a magnetic field from the body of a superconductor, can give rise to the following implications:

$$B = \mu_0(H + M) = 0 \tag{2.1}$$

where B represents the magnetic flux density, μ_0 represents the permeability of vacuum, H represents the magnetic field strength, and M represents the magnetisation. Equation (2.1) gives:

$$H = -M \tag{2.2}$$

Consequently, the susceptibility:

$$\chi = \frac{dM}{dH} = -1 \tag{2.3}$$

Assuming that a superconductor has the optimum resistivity:

$$\rho = 0 \tag{2.4}$$

A superconductor's diamagnetism is due to the surface shielding current, which produces a magnetic field equal in magnitude but opposite in direction to the external field

[2.5]. As a result, the two magnetic fields cancel each other out, allowing for the complete expulsion of the magnetic field and resulting in a zero magnetic field inside the superconductor.

2.1.2 The London Theory

Since the surface current density generated by super electrons is not infinite, the magnetic field required to induce ideal diamagnetism in a superconductor must penetrate the material to a certain depth [2.5, 2.6].

The penetration depth, represented by λ, can be determined through fundamental electrodynamics principles. In the following paragraphs, we will introduce the London Theory, which is based on the concept that the penetration depth fluctuates according to the super current density (n_s) [2.5, 2.6].

In a superconductor, super-electrons face no impediment to their motion. This presupposes that a steady electric field E exists at the surface of the superconductor and that electrons accelerate steadily under the influence of this field.

$$m_s \dot{v} = Eq \tag{2.5}$$

where m_s is free carrier mass, v is carrier velocity, q is carrier charge (superelectron or copper-pairs), and the dot on the top of v indicates time derivative (i.e. the acceleration) [2.24]. Then, the super current density can be written as:

$$J = n_s v q \tag{2.6}$$

where n_s is the number of super-electrons per unit volume. Haas Lorentz indicated in 1925 that the electrodynamic screening length λ would be [2.25].

$$\lambda = \sqrt{\frac{{m_s}^2}{\mu_0 n_s q}} \tag{2.7}$$

Rearrange (2.5), (2.6), and (2.7) as follows:

$$E = \frac{m_s \dot{v}}{q} = \frac{m_s \dot{j}}{n_s q^2} = \mu_0 \lambda^2 \dot{j} \tag{2.8}$$

where $\dot{J}$ is the current density's time derivative. Taking the curl on the both sides in equation (2.8), one has:

$$\nabla \times E = \mu_0 \lambda^2 \nabla \times \dot{J} \tag{2.9}$$

Utilising the Maxwell Equations:

$$\nabla \times E = -\dot{B} \tag{2.10}$$

$$\nabla \times B = \mu_0 J \tag{2.11}$$

where $\dot{B}$ represents the time derivative of the magnetic flux density. Equation (2.9) can be rearranged:

$$\dot{B} + \lambda^2 \nabla \times \nabla \times \dot{B} = 0 \tag{2.12}$$

For the second term:

$$\nabla \times \nabla \times \dot{B} = -\nabla^2 \dot{B} \tag{2.13}$$

Equation (2.12) can be converted as:

$$\dot{B} = \lambda^2 \nabla^2 \dot{B} \tag{2.14}$$

The solution to Equation (2.14) must meet the diamagnetism condition:

$$\dot{B}(x) = \dot{B}_a e^{\left(-\frac{z}{\lambda}\right)} \tag{2.15}$$

where B_a is the external applied magnetic flux density, $B_a = \mu_0 H_a$.

The criterion for a perfect conductor, according to Equation (2.15), is $B(x) = 0$ when $z >> \lambda$. Nevertheless, a superconductor is more than a perfect conductor [2.7]. H. London and F. London conducted the temporal integration of Equation (2.15), transformed this equation with a static magnetic flux density B, and set the value of the extra unknown integration constant to zero. They observed that [2.7, 2.8]:

$$B(x) = B_a e^{\left(-\frac{z}{\lambda}\right)} \tag{2.16}$$

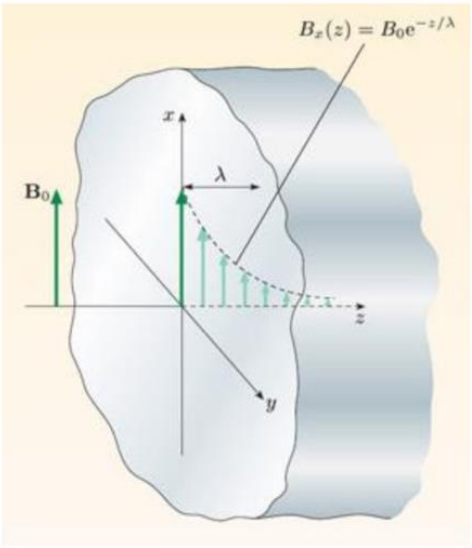

Figure 2.2: London penetration depth: the penetration of a magnetic field into a superconductor [27].

According to the London Theory, Figure 2.2 depicts how the magnetic field penetrates a superconductor. Within a range of λ near the surface, the magnetic field decreases exponentially, whereas the superconductor's core is devoid of a magnetic field [2.7, 2.8]. The Meissner Effect is mathematically explained by the London Theory [2.6]. Equation (2.16) accurately explains the Meissner Effect, whereby a superconductor placed in a static external magnetic field generates spontaneous supercurrents in the surface layer, creating an opposing field within the sample. This opposing field can effectively cancel out the applied field inside the superconductor [2.6].

2.1.3 Ginzburg-Landau (GL) Theory

The Ginzburg-Landau Theory, proposed by Ginzburg and Landau in 1950, has been instrumental in the progress of superconductivity. This theory provides a thermodynamic, phenomenological explanation of superconductivity [2.8, 2.9]. The Ginzburg-Landau Theory sheds light on the long coherence length observed in certain superconductors, such as low-temperature superconductors (LTS). Additionally, it clarifies why high-temperature superconductors (HTS) have a shorter coherence length [2.9, 2.10].

The Ginzburg-Landau Theory is based on a few basic assumptions that explain superconductivity on the basis of a complex order parameter ϕ, and it may be represented as the products of a modulus $|\phi|$ and a phase factor θ:

$$\phi = \sqrt{n_s}\exp(i\theta) \tag{2.17}$$

Ginzburg and Landau proposed that a superconductor's free energy density (F_s) can be represented as a function of complex order parameters, derived from the Landau free energy density [9]:

$$F_s = F_n + \alpha|\phi|^2 + \frac{\beta}{2}|\phi|^4 + \frac{1}{2m}|(-i\hbar\nabla - 2eA)\phi|^2 + \frac{B^2}{2\mu_0} \tag{2.18}$$

Equation (2.18) includes temperature-dependent functions α and β, where A represents the magnetic potential (vector), $\hbar$ is the Planck constant, and e and m are the charge and mass of the particles described by ϕ.

$$\alpha\phi + \frac{\beta}{2}|\phi|^2\phi + \frac{1}{2m}(-i\hbar\nabla - 2eA)^2\phi = 0 \tag{2.19}$$

In order to minimize changes in the parameter ϕ and magnetic potential A that affect free energy, the first Ginzburg-Landau equation utilizes the derivative of Fs with respect to ϕ.:

$$J = \frac{e}{m}[\phi^*(-i\hbar\nabla - 2eA)\phi] + c.c. \tag{2.20}$$

The Ginzburg-Landau Equations have several useful implications, including their prediction of two characteristic lengths for a superconductor [2.7, 2.9, 2.10]. The coherence length ξ is particularly important, as it characterizes the extent of thermodynamic fluctuations during the superconducting ($T < T_c$) phase.

$$\xi = \sqrt{\frac{\hbar^2}{4m\alpha(T)}} \quad (T < T_c) \tag{2.21}$$

$T > T_c$ refers to the normal phase, which is given by:

$$\xi = \sqrt{\frac{\hbar^2}{4m\alpha(T)}} \quad (T > T_c) \tag{2.22}$$

The penetration depth λ is predicted in the second prediction, which is provided by:

$$\lambda = \sqrt{\frac{m}{4\mu_0 e^2 \phi^2}} \tag{2.23}$$

As mentioned before, ϕ represents the equilibrium quantity for the order parameter in the absence of an electromagnetic field, while λ denotes the depth to which an external magnetic field can penetrate a superconductor [2.8, 2.9].

2.1.4 Low T_c and High T_c Superconductors

Numerous studies have been conducted since Kamerlingh-Onnes' first discovery of superconductor, and scientists are continually on the lookout for greater critical temperature (Tc) superconductors [2.11]. Thereafter, critical temperatures were used to categorise superconductors as either low Tc or high Tc [2.1, 2.11]. Metallic and alloy compounds were the first class of superconductors to be identified. Niobium has the greatest critical temperature (9.3 K) for a pure metal, necessitating the use of liquid helium (H_e) as the cryogen [2.1, 2.12]. However, there are several metallic compounds and alloys that retain their superconducting condition at far greater temperatures. As an example of a high-temperature superconductor, lanthanum-barium-copper oxide ceramic ($LaBaCuO_4$) had its critical temperature (T_c) determined at 30 K. Since then, two distinct types of superconductors have been identified [2.2, 2.13] as in Table 2.1:

Table 2.1: Difference between LTS and HTS

Low Temperature Superconductors (LTS)	**High Temperature Superconductors (HTS)**
T_c is lower than 30 K	T_c is higher than 30 K

In recent years, a large number of HTSs based on copper oxide have been found and exploited in research and engineering, such as $YBa_2Cu_3O_7$ ("YBCO" or "Y123") and $Bi_2Sr_2CaCuO_8$ ("BSCCO" or "Bi2212") [2.26, 2.35]. At atmospheric pressure, the critical temperature of YBCO is 93 K and that of BSCCO is 105 K. The compound $HgBa_2Ca_2Cu_3O_3$, with a critical temperature of 135 K at atmospheric pressure [2.14], has the highest-known T_c.

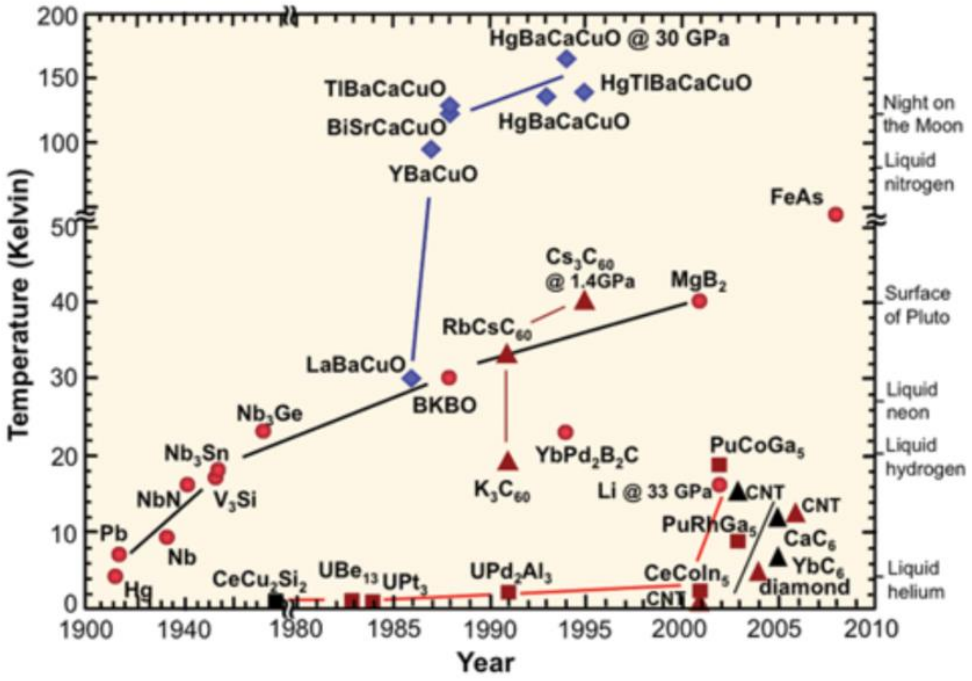

Figure 2.3: Timeline for the discovery of superconducting materials and the development of the critical temperature [2.15]

$LaBa_2CuO_{4-x}$ was the first High Temperature Superconductor discovered by Bednorz and Muller in 1986 [2.16], for which they were awarded the Nobel Prize in Physics in 1987. The first HTS material utilised to manufacture HTS wires was BSCCO. 1987 saw the discovery of YBCO, a superconducting material with a T_c greater than the boiling point of liquid nitrogen (77 K) [2.7, 2.17]. The invention of YBCO considerably enhanced the performance of HTSs, and its production method has already been industrialised [2.18].

In 2001, Jin *et al.* discovered magnesium diboride [2.19]. Among non-copper oxide superconductors, MgB_2 has the highest critical temperature (T_c) of up to 39 K [2.19, 2.20]. Due to its low cost and the fact that magnesium and boron are abundant, there has been renewed interest in MgB_2 for use in power applications [20]. A new class of superconductors was discovered in 2008, which is composed of a family of iron-based materials that exhibit superconducting properties [2.20, 2.21].

Figure 2.4 shows the relationship between magnetic field and temperature for the five key superconductors used in industry, and their essential properties are outlined in Table 2.2.

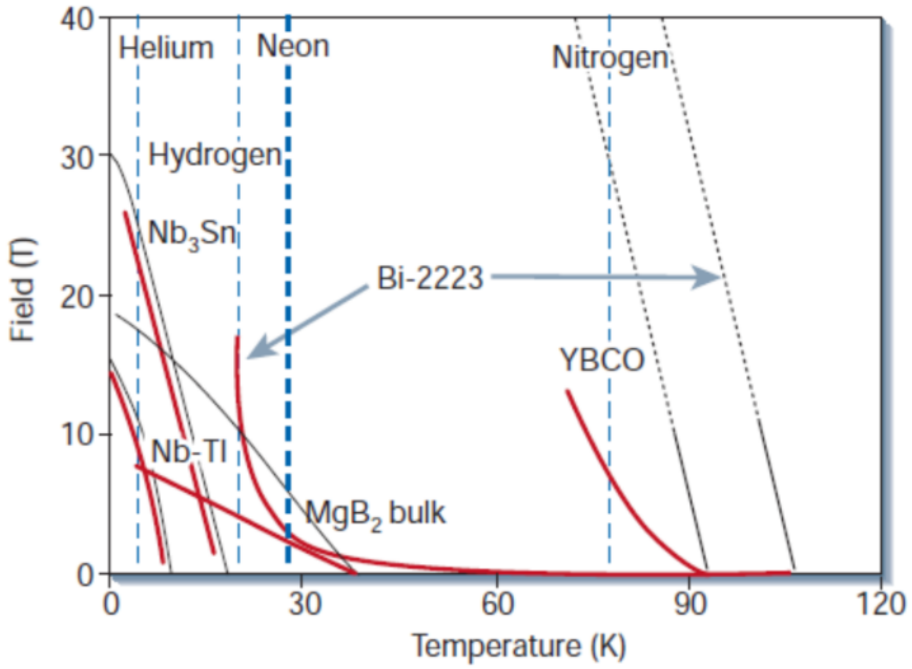

Figure 2.4: Magnetic flux density vs temperature curves for five main commercial superconductors [2.21].

Table 2.2: Basic parameter for five common superconductors

Materials	**Tc (K)**	**$\mu_0 H_c2$ (T)**	**$\mu_0 H_c1$ (T)**	**Coherence Length (nm)**	**Penetration Depth (nm)**	**Critical Current (A/mm^2)**
NbTi	9	12 (4K)	10.5 (4K)	4	240	~ $4x10^5$
Nb_3Sn	18	27 (4K)	24 (4K)	3	65	~ 10^6
MgB_2	39	15 (4K)	8 (4K)	6.5	140	~ 10^6
YBCO	92	>100T (4K)	>5T (4K)	1.5	150	~ 10^7
Bi-2223	108	>100T (4K)	>0.2 (4K)	1.5	150	~ 10^6

2.1.5 First Generation (1G) and Second Generation (2G) HTSs

BSCCO is also referred to as First Generation High Temperature Superconductor (1G HTS) material [2.22]. As demonstrated in Figure 2.5 (a), 1G HTS employs the structure of a multifilamentary composite [2.23]. The cross-section of 1G HTS filaments is approximately elliptical, as depicted in Figure 2.5 (b). Generally speaking, there are two types of BSCCO that are transformed into wires (via the powder-in-tube process): $Bi_2Sr_2CaCu_2O_8$ (BSCCO-2212) and $Bi_2SrCa_2Cu_3O_{10}$ (BSCCO-2223) [2.26, 2.47]. 1G HTS has served as the foundation for the first demonstrations of electrical power devices [2.23].

The method of depositing YBCO superconductor on metal tapes coated with multiple buffering layers, also known as the coated conductor approach, is a promising technique for producing YBCO superconducting tape [2.24]. YBCO tapes are categorized as Second-Generation High Temperature Superconductors (2G HTS) and can be made more flexible by utilizing this approach. Figure 2.5 (a) illustrates the importance of the biaxial texture of Second-Generation High Temperature Superconductors (2G HTS) in achieving a high current-carrying capacity [2.13]. Nowadays, several companies such as Superpower, American Superconductor, European Advanced Superconductors, Fujikura, and Nexans Superconductors produce YBCO 2G HTS tapes [2.7, 2.18, 2.23, 2.24].

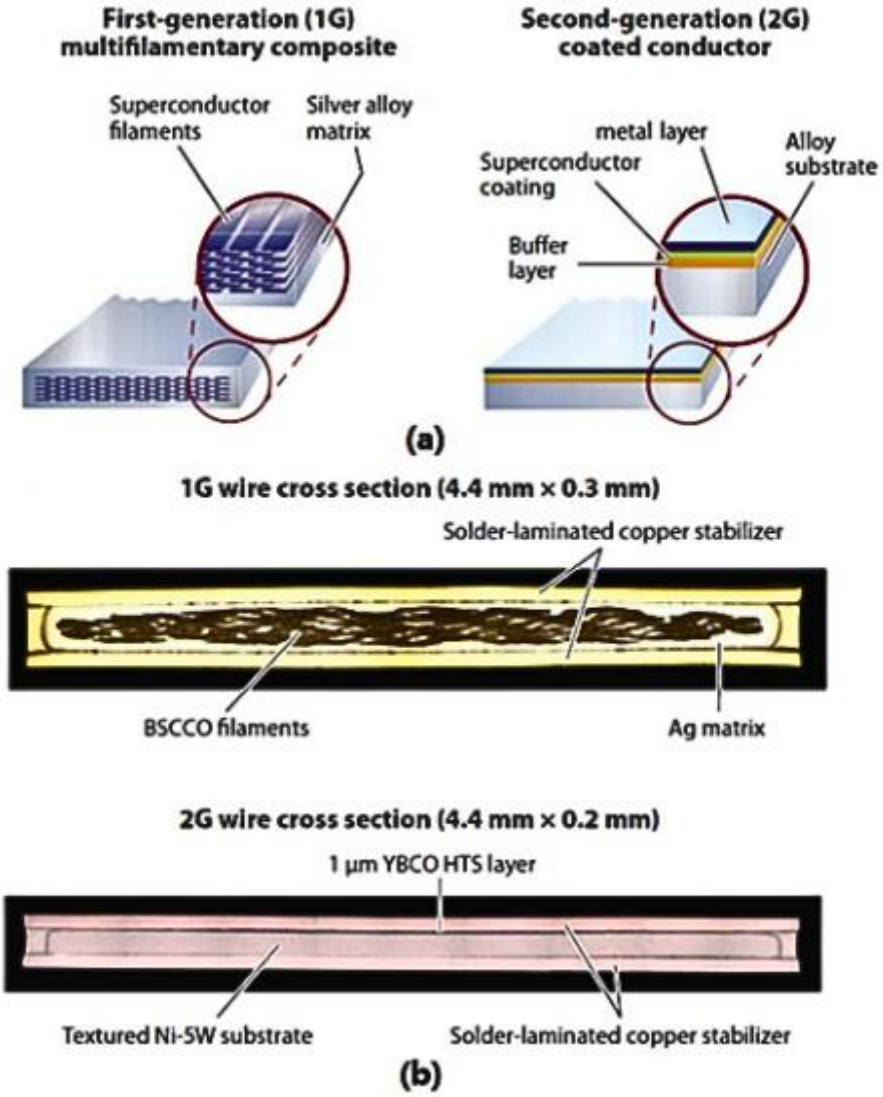

Figure 2.5: (a) Schematic and (b) Cross-section of 1G HTS and 2G HTS wires [2.23].

2.1.6 Type I and Type II Superconductors

As discussed in the previous section, superconductors transition into the Meissner State when subjected to an external magnetic field. Nonetheless, this state becomes unstable when the external field surpasses a specific threshold. While Type I superconductors return to their normal state, Type II superconductors go through a mixed state when the critical magnetic field is exceeded [2.5, 2.6]. Type I superconductors are therefore those that have only the superconducting state and the normal state. The three states of Type II superconductors are superconducting, mixed, and normal [2.5, 2.25]. Figure 2.6 illustrates the distinction between Type I and Type II superconductors.

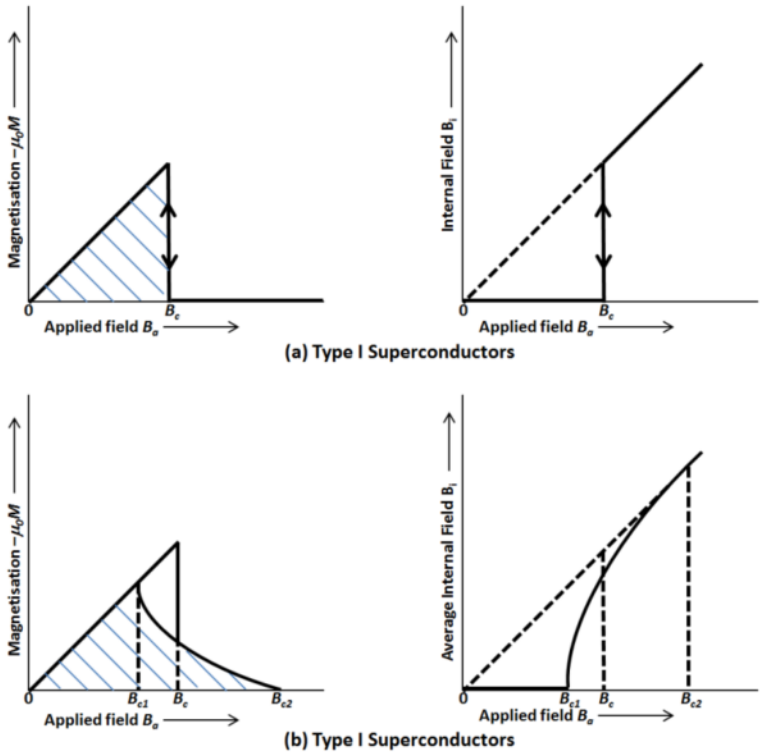

Figure 2.6: Magnetisation and internal field of type I and type II superconductors [2.25].

In Figure 2.6 (a), superconductors of Type I, B_c denotes the critical field. Once the externally supplied field exceeds B_c and the magnetic flux concurrently permeates the entire sample, the superconductor quickly reverts from the Meissner State to its normal state. The magnetisation of the sample similarly falls to zero, resulting in the internal magnetic field equalling the external magnetic field [2.5]. The majority of these Type I superconducting materials are metals and metalloids [2.5].

Type II superconductors have two critical fields: the lower critical field (B_{c1}) and the upper critical field (B_{c2}) [2.5]. Once the external field surpasses B_{c1}, the superconductor partially admits quantized flux, resulting in a mixed state where the magnetisation of the superconductor decreases gradually as the external field grows. When the external field surpasses B_{c2}, the magnetisation of the superconductor becomes zero. At the upper critical field, B_{c2}, the external and internal fields are equivalent [2.5].

The Ginzburg-Landau parameter κ can be computed using London penetration depth λ and coherence length ξ as shown in Figure 2.7 [2.5].

$$\kappa = \frac{\lambda}{\xi} \tag{2.24}$$

Table 2.3: Distinction between type I and type II superconductors

Type I Superconductors	Type II Superconductors
$k < \frac{1}{\sqrt{2}}$	$k > \frac{1}{\sqrt{2}}$

The difference κ between type I and type II superconductors is extremely large as in Table 2.3. Type I superconductors, such as lead, have a value of κ = 0.48, while type II superconductors, such as YBCO, based on copper, have a value of κ = 95 [2.5, 2.6].

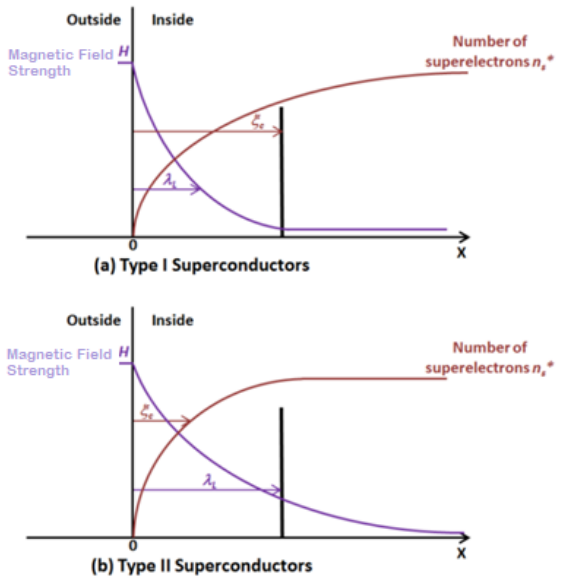

Figure 2.7: Type I and Type II superconductors: relationship between the penetration depth λ and coherence length ξ [2.5].

The Ginsburg-Landau theory characterises superconducting vortices in the mixed state with exactitude. In general, the size of these vortices is relatively small, and a Type II bulk contains millions of vortices [2.5, 2.27].

2.1.7 BCS Theory

The microscopic quantum mechanical theory of superconductivity, known as the BCS theory, is named after its originators J. Bardeen, L. Cooper, and R. Schrieffer. They were the first to propose this theory [2.6, 2.8].

The BCS theory postulates that a pair of electrons, referred to as Cooper pairs [2.24], carries the supercurrent. These pairs are more stable than individual electrons and can better withstand material lattice vibrations [2.6]. The stability of a Cooper pair's attraction to its mate allows it to encounter less resistance. In consequence, Cooper pairs traversing the material lattice are less impacted by thermal vibrations below the critical temperature [2.6, 2.28].

The BCS theory provides a comprehensive explanation of the physical connections between the energy gap E, at temperature T and the critical temperature T_c, as well as the Meissner Effect [2.24, 2.59]. The BCS theory accurately describes the physical behaviour of superconductors, simple alloys, and elements that function at low temperatures. However, the theory does not precisely correspond to the physical phenomena observed in other types of materials that exhibit superconductivity. The BCS theory is incapable of explaining the physical occurrence of high-temperature superconductors [2.28].

2.1.8 Flux Pinning

The mixed state of Type II superconductors is crucial for many of their applications, which require them to produce high currents under strong magnetic fields [2.29]. These practical Type II superconductors are known as hard superconductors, which distinguishes them from their idealized counterparts.

In an ideal Type II superconducting sample, the mixed state implies that some flux has penetrated the sample, which is oriented perpendicularly [2.8, 2.30]. Flowing electrical currents produce a Lorentz force density between the current and vortices:

$$F_L = J \times B \tag{2.25}$$

According to Equation (2.25), the flow of vortices through a superconductor must be perpendicular to both the direction of the current and the magnetic field since the currents are fixed by the boundaries [2.31]. The movement of vortices generates an electric field.

$$E = B \times v \tag{2.26}$$

The generation of an electric field, parallel to the current, due to vortex motion in a superconductor creates electrical resistance [2.8]. Vortex motion results in the dissipation of heat in the material, which could be attributed to two primary factors. The first factor involves the creation of electric fields by moving vortices that could transfer energy from the electric field to the lattice and generate heat by accelerating unpaired electrons [2.32]. The second factor relates to the variation in the Cooper pair density across space, which rises from zero at the vortex centre to infinity at its edges [2.32].

In a perfect type II superconductor, the movement of vortices is unimpeded, so that even minor random currents can cause vortex motion and energy dissipation, leading to a transport current of zero [2.32]. However, to make type II superconductors practical, they must be able to sustain significant critical currents, which create substantial Lorentz forces [2.33]. This requires a strong pinning force to counteract the Lorentz forces and prevent vortex motion [2.32, 2.33]. To achieve such pinning, impurities and defects can be introduced into the material, creating what are known as hard superconductors.

Since magnetic fields are confined within the volume of a superconducting material, hard superconductors can support extremely large electrical currents. In fact, once a direct current (below the critical current) passes through a hard superconductor, it immediately demonstrates the property of being lossless [2.34]. However, under AC conditions, vortices within the hard superconductor must move in response to changes in the magnetic field. An obstruction is characterised by the pinning force, and overcoming it is an irreversible procedure [2.34]. For hard superconductors, the accompanying power dissipation is a hysteresis loss, as will be detailed in the next sections.

2.2 Applications of Superconductivity

Recently, the manufacturing and commercial availability of HTS wires and tapes in long lengths has seen significant progress. This has led to the increased utilisation of HTS material in various large-scale power applications. The use of HTS material offers a boost in machine efficiency, as well as a substantial decrease in size and volume, resulting in the ability to design electrical machines that are compact, lightweight, and efficient. Additionally, superconductivity opens up new possibilities, such as superconducting fault current limiters

and magnetic energy storage [2.35]. HTS material has proved to be an economical superconductor compared to low Tc materials and, due to the economical cryogenic cooling, which has increased its prospects into the practical power applications. In terms of material properties, high critical current density, high irreversibility field and high mechanical strength are some of the major advantages.

In comparison to normal conductor HTS has the ability to carry higher current with almost zero losses in DC and lower losses in AC conditions. The copper coil in conventional machines typically operates with a current density of 3-5 A/mm^2, on the other hand the HTS wire can be operated at 200 A/mm^2 [2.36]. These characteristics make HTS material feasible to develop electric devices with smaller dimensions, reduced weight and high efficiency. Continuous research on material properties and advancements in the manufacturing technologies have led the market availability of high quality HTS wire in long lengths from a number of manufacturers. This achievement has triggered the efforts in commercialisation of HTS devices. Some of the properties and benefits of HTS material against individual applications are highlighted in Table 2.4.

Table 2.4: HTS properties and benefits against applications

Benefits	**Property**	**Application(s)**
Higher Efficiency	R=0	Motors, Generators, Cables, Transformers
Higher Power Density	J_c	Motors, Generators, Cables, Transformers
Novel Opportunities	R=0 Dm/dB<0 Transition	SMES Magnetic Bearings Fault Current Limiters, Switches

The cost of the material is still a challenge which is a major hurdle in the development and commercialisation of HTS technology. Economic feasibilities and case studies are required for individual applications. Apart from the engineering prospective, environmental part of HTS applications must be studied. HTS offers potential benefits in energy conservation and emission reduction as compared to the conventional machines.

2.2.1 HTS Power Systems

2.2.1.1 HTS Fault Current Limiters

In any power system, there are high chances of shorted circuits. HTS fault current limiter (HFCL) effectively reacts to limit the fault with various additional features such as automatic recovery, automatic protection, no over-voltage and low resistance during routine operation. It maintains its superconducting state during the normal state of operation, and returns to the normal state in case of any surge or fault where the current flow is reduced passively. HFCL has two main categories: resistive type HFCL and inductive type HFCL, which offer high resistance and high impedance respectively as per the operational demand. HFCL enables the innovative design of electric grids exploiting the sudden transitions of superconducting material from no-resistance or negligible impedance to instantaneous limitation.

With the commercial availability of the HTS material, development of large scale HFCLs has been possible. Many prototypes and samples have been designed and tested including medium voltage and high voltage, but the first commercial resistive HFCL was developed by Nexans in 2009 [2.37]. Recently a 220 kV/1.5 kA resistive type fault current limiter has been developed and tested limiting the current up to 63 kA_{rms} up to duration of 100 ms [2.38].

2.2.1.2 HTS Transformers

The HTS transformers are differentiated from conventional counterparts in terms of their winding characteristics, where HTS wires or tapes are used instead of copper or aluminium. HTS transformers bring the benefits of being lighter in weight and considerably smaller units along with lower life cycle cost, less hazards and reduced environmental pollution. Furthermore, they also offer the novel features such as overload ability and fault current limiting function [2.39].

Research on HTS transformer is mainly focused on reducing the AC loss, which is the main impediment to fulfil higher efficiency because of the cooling penalty. A number of power transformers have been built and tested. A 24.9 kV/4.16 kV, 5/10 MVA utility power transformer was tested by Waukesha Company in 2005. A three phase HTS power transformer was manufactured with rating of 630 kVA, 10 kV/0.4 kV and it has been in the operation at HTS power substation in Baiyin, China since 2011 [2.40].

With the novel features like high current density and low energy loss in the superconducting state along with the feature of self-acting resistance in quenching state, HTS windings enable the possibilities of various special transformers such as hybrid transformers, traction transformers, pulse transformers and fault current limiter transformers.

2.2.1.3 HTS Transmission Systems

With the growth in the population, the current power system will require further extension in order to meet the load requirements of the future. HTS cables have been in the spot to respond to such requirement. The superconductors can carry very high current with low resistance which allows to transmit more power than conventional cable. A number of demonstration projects have been executed to promote superconducting technology in transmission system [2.41]. In early 2000s, Korea initiated the research on the development of superconducting cables. Consequently, they were able to develop and conduct the successful tests on 23 kV to 154 kV superconducting cables for AC as well as DC [2.42, 2.43]. Furthermore, KEPCO, Korea's electric utility company initiated its first commercial project using a 23 kV three core tri-axial superconducting transmission cable [2.44].

Superconducting cables have the ability to transmit up to six time more power than conventional transmission cables with similar capacity. In spite of such advantages, HTS cables require massive capital investment, which is a major obstacle in their commercialisation. A recent study was carried out on the economic feasibility study for using HTS cable in UK's electrical distribution network, which showed that HTS power transmission solution required 75% more investment than conventional cables [2.45]. However, various studies are still being conducted to further evaluate the feasibility and to enable the market penetration of superconducting cables.

2.2.1.4 Superconducting Magnetic Energy Storage (SMES)

There are various problems in the transmission lines, such as the surge current due to lightning, inrush current due to switching of electrical equipment or a simple bird short circuit creating instability in the overall power system. In order to improve the ability to exchange active power and reactive power in conventional power system, energy storage systems are incorporated in the system. The examples of such energy storage systems are fly wheels, super capacitors, batteries and most recent SMES. These devices are used to create the stability in the system having the ability to absorb/transfer large power [2.46]. Availability of

superconducting material in recent years has encouraged the development of SMES. Although its development seems expensive as it is required in large quantity to manufacture SMES coil but it has good prospects in terms of power system stability. Hybrid SMES is also under investigation where superconducting and conventional energy storage systems are combined to reduce the overall capacity cost [2.47].

2.2.2 HTS Rotating Machines

2.2.2.1 HTS Motors

HTS motors have been considered for wide range of applications, and experimental works have been carried out on aerospace, naval as well as on industrial applications mostly of synchronous type. Most of the HTS motors are designed with superconducting material in their rotor part in order to supply high air-gap magnetic flux density which brings high power density in motors. However, machines with HTS bring challenges such as manufacturing, maintenance, and refrigeration. Apart from the mechanical characteristics, the high magnetic flux density in the rotor coil will disturb the critical current of HTS tapes which results in an increase of operational temperatures to 20-30 K causing a massive additional cooling cost.

There have been significant progresses in research on HTS synchronous motors over the past years. Doosan Heavy Industries designed and fabricated a 1 MW HTS synchronous motor, and its performance test was reported in [2.48]. General Electric also tested a 1 MW HTS machine for Air Force Research Lab (AFRL) [2.49]. A 36.5 MW HTS motor for ship propulsion was manufactured in the United States, and the machine successfully passed factory tests at no load as well as on full load [2.50]. A concept design of linear synchronous motor (LSM) for high speed railway application was presented in [2.51], while a small scale HTS LSM prototype has been installed in railway bogie [2.52].

Apart from the synchronous motors, there have been significant works in the induction motors as well. HTS induction motors overcome problems such as integrity of rotor dynamic seal and mechanical strength especially at high speed operation [2.53]. A Japanese group developed a 20kW induction/synchronous fully superconducting motor having HTS windings in stator as well as in rotor part to achieve maximum torque density and power [2.54].

2.2.2.2 HTS Wind Generators

Conventional generators with copper winding in the rotor and stator part face problems in terms of low output power density and low efficiency especially when high capacity power

generation is considered. Since HTS offers much higher critical current density and power density, the weight and volume of large-scale power generators can be reduced significantly by incorporating HTS windings in stator as well as rotor parts. Copper coils in conventional machine usually have current density between 3 and 5 A/mm^2, while in superconductors, that current density may be increased up to 200 A/mm^2 [2.36]. As a result, higher induction current can be drawn in HTS coils which leads to the possible axial dimension reduction of generator of the same power.

A lot of research is being carried out to investigate the HTS wind power solutions in terms of conceptual designs, component demonstration and prototypes. However, a complete setup of full scale operational HTS wind generator demonstration has not been reported. A demonstration of pole pair segment of MW class direct driven HTS wind turbine was conducted in HTS-GEN project [2.55]. Most recently, the Eco-Swing project was launched which was funded by EU Horizon 2020 program. In this program the world's first MW class direct driven HTS generator was manufactured and the generator was installed in a commercial wind turbine near the Western coast of Denmark, and the project is under basic experimental stage [2.56].

2.3 AC loss of in HTS Coated Conductors

AC loss is important when superconductors operate under AC magnetic field or AC currents. These AC losses generate thermal dissipation which affects the overall performance and efficiency of the device. A typical commercial superconductor, e.g. ReBCO-coated HTS material, has different layers of material in addition to the superconducting materials, such as magnetic material, substrates and buffers [2.57] as shown in Figure 2.8. These individual layers can significantly contribute towards the total loss subject to different operating conditions. These categories are defined below.

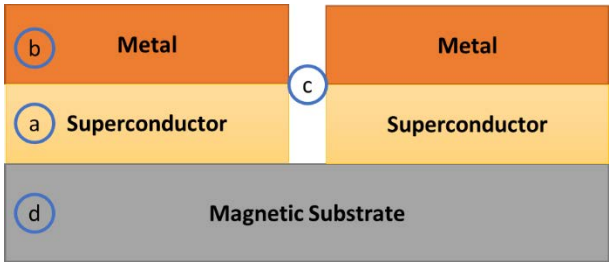

Figure 2.8: Illustration of various loss influences in HTS: (a) hysteresis loss in superconductors, (b) eddy current loss in metallic part, (c) coupling loss amongst filaments, and (d) ferromagnetic loss in magnetic substrate [2.24].

2.3.1 Hysteresis Loss

Among the various loss contributions, hysteresis loss is the largest part in superconductors. It is generated by the saturation and variations of magnetic flux when a superconductor is subjected to an external magnetic field [2.58] as shown in Figure 2.9 (a).

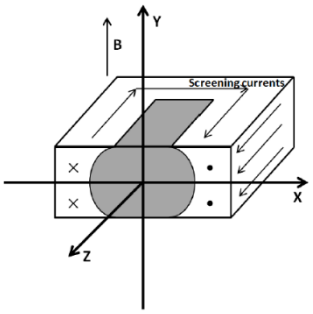

(a)

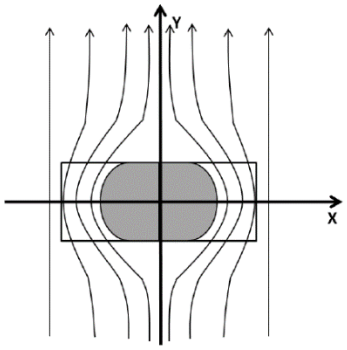

(b)

Figure 2.9: Illustrations of hysteresis loss when HTS sample is subjected to external magnetic field magnetic field [2.24].

As the magnetic field changes, it affects the flux-line patterns and internal magnetic field. Then according to Faraday's law, an electric field is induced by the varying magnetic field inside the material. The electrical field strength E can be described below, where *B* is the magnetic flux density.

$$\nabla \times E = -\frac{\partial B}{\partial t} \tag{2.27}$$

As shown in Figure 2.9 (a), the electric field inside the material energies screening currents which are demonstrated as arrows [2.58]. Moreover, as per the Ampere's law, the induced screening current defines the magnetic field distribution inside the superconductor. Then the magnetic flux density *B* can be described as below, where *J* is the current density.

$$\nabla \times B = \mu_0 J \tag{2.28}$$

From the above equations the local power density can be calculated as $E \times J$. The energy which is supplied by the power source through external magnetic field, is required for depinning of the vortices and flux lines movement, and the overall process is a dissipative process generating heat which must be removed by a robust cryogenic system [2.58].

Figure 2.9 (b) represents the case when there is magnetic flux density B around the HTS sample, assuming that the sample is cryogenically cooled and under a magnetic field changing at a constant rate. There exists homogeneous magnetic field strength *H*, created by the external magnetic field. Magnetisation given by the screening current can be represented as *M*. Thus, the local magnetic field which surrounds superconductor can be described as $\mu_0(H + M)$. The screening currents strain to shield the internal structure of superconductor from magnetic field variations [2.58]. *M* and *H* are oriented to be opposite to each other in the centre where local magnetic flux density is lower than $\mu_0 H$. When $y = 0$, *M* and *H* are oriented as parallel to each other, at this point the magnetic flux density is higher than $\mu_0 H$ [2.58]. Since *B* is external magnetic field which is outside the superconductor, *M* must be equal to zero. Therefore, it can be stated as:

$$B = \mu_0 H \tag{2.29}$$

There also exists a magnetic movement inside the superconducting sample with can be denoted as m, which can be calculated from the distribution of screening currents. Hence, the AC loss of superconducting region can be calculated by the integration of $B \times dm$ or $m \times dB$ for a single cycle of magnetic field.

When a current flow through a superconductor, it creates a self-generated magnetic field, which is known as the self-field. Under AC conditions, the AC self-field penetrates into the superconductor during each cycle. This variation in the AC self-field inside the superconductor can lead to hysteresis loss, even in the absence of any external magnetic field [2.59].

2.3.2 Coupling Loss

When a normal conductor is subjected to an external AC magnetic field, eddy currents are generated in the conductor. However, in superconductors, a different kind of eddy current is produced, which is composed of multiple filaments embedded in a normal material. As shown in Figure 2.10, a composite superconducting material with two filaments is depicted in grey colour. When a magnetic field is directed perpendicular to the plane, an electrical loop is formed, which induces electrical currents as indicated by arrows in the loop [2.60].

Theoretically, there is almost zero resistance inside superconducting filaments except at the joints of the composites which resists the flow of current. This cross current is called coupling current. This process generates additional power dissipation which is demonstrated as coupling loss [2.58].

In order to reduce the coupling current AC loss, the coupling current must be maintained below the critical current of the superconductor material.

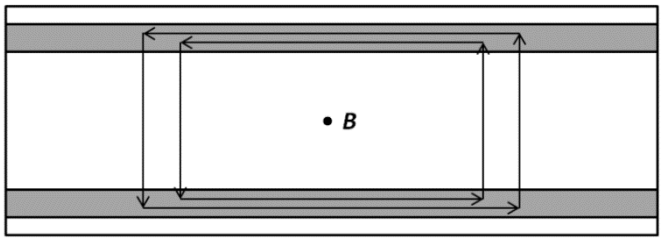

Figure 2.10: Illustration of coupling AC loss in composite conductor [2.60].

2.3.3 Ferromagnetic Loss

The superconducting material is deposited on the magnetic or ferromagnetic substrates [2.23] as in Figure 2.9. This part of the material also contributes to the overall loss in HTS tapes or wires which must be taken into consideration. The magnetic component usually contributes to the total AC loss in superconductors in two ways [2.23]:

- It modifies the magnetic characteristics within the material, similar to the iron core found in superconducting motors.
- It contributes to the overall loss in the magnetic substrates by producing additional iron loss or core loss.

Therefore, it is equally crucial to consider the contribution of magnetic components when estimating the AC loss in superconductors.

2.3.4 Eddy Current Loss

When a metal is subjected to an external AC magnetic field, the resulting eddy-current losses typically generate power dissipation through resistive or Joule heating effects [2.57].

Although eddy current losses are usually insignificant at low or moderate operating frequencies, they must be considered when designing high-frequency applications, as suggested by some studies. A superconducting tape with a copper stabilizer of 50 μm, critical current (self-field) of 260 A and operated at 60 Hz AC up to its critical current, generates the eddy-current loss with the factor of 5 mW/m in the copper stabilizer [2.61]. While with the same conditions, the corresponding total hysteresis loss is estimated to be 380 mW/m, which is 23 times more than the eddy-current loss, proving that it creates much impact at higher power frequencies. Furthermore, the eddy-current loss creates a significant impact while working at low operating temperatures (such as 4.2 K), because metal resistivity decreases significantly at these temperatures [2.57].

2.4 Recent Developments in AC Loss Characterisation

The application potential of 2G HTS coated conductors is considered highly promising due to their high current density and comparatively elevated operating temperature. Thanks to their wide and thin geometrical structure, the power loss, or heat, is easily dissipated under AC conditions. AC losses are critical in the efficiency and economic feasibility of HTS power applications [2.62]. Therefore, finding a way to reduce the AC loss has been a key research focus in the HTS material research. When the HTS material is under AC magnetic field, a constant screening current or eddy current flowing in the wide surface of second generation HTS material contributes to the magnetisation losses, and hence it is related to the width of the conductor [2.62]. Commercial 2G HTS material is available with width of 2 mm ~ 12 mm. Apparently reducing the width of conductor can be a natural way to reduce the AC losses. Subdividing the YBCO layer of conductor into narrow filaments was first proposed by Carr *et al.* [2.63], where the striations are achieved by laser ablation [2.64, 2.65]. In striation process superconducting thin films are separated and electrically isolated, which leads to substantial reduction of the losses. However, practically still there is some imperfection in the separation of strips where striation leaves conductive bridges between strips, causing current to flow freely [2.66]. The reduction of AC loss of striated multifilament YBCO coated conductor (CC) has also been discussed at various frequencies and a degradation of about 40% has been found due to laser striation process [2.66-2.69]. AC loss reduction has also been reported on multifilament

YBCO coils but it is not as much as expected. Xing *et al.* [2.70] reported 20% reduction in AC loss by multifilament method in comparison with non-striated YBCO coils. Moreover, a detailed review on how filaments can reduce the AC losses in HTS CC has been mentioned in [2.71]. When the multifilament YBCO conductor is subjected to AC fields, a coupling current flows between the filaments in the copper stabilizer layers, which increases the overall losses. In order to reduce the coupling losses, a fully transposed 2G HTS cable, e.g. Roebel Cables, has been proposed in [2.72]. Reduction of AC losses in Roebel cables has been studied, maintaining the critical current through the process and demonstrating the possibility of increased transport current [2.73, 2.74]. Multifilament Roebel cables are also developed for the further reduction of AC losses [2.75].

Furthermore, a new technique has also been reported called soldered-stacked-square (3S) 2G HTS wire [2.76], in which 2G HTS conductors are cut into 1 mm wide pieces and are soldered together to form a stack of wire. The reduction of AC loss on solenoid coil using 3S 2G HTS wire was reported in [2.62], which shows that the 3S wire is able to reduce the AC losses by 80% with the flexibility of adjusting critical current for different applications. Hence, 3S wires have the credentials of becoming a powerful technique with high efficiency, facilitating the development of 2G HTS power applications.

An HTS coated conductor (CC) is a composite material which consists of magnetic material and metallic material where each of the materials accounts for the significant non-negligible AC loss depending upon the frequency. The traditional theoretical approach to overcome this problem is to divide the AC losses of HTS CC operating below its critical current into three main categories. Hysteresis losses are due to magnetic flux penetration and movement in the material, ferromagnetic losses are due to the magnetic hysteresis in the magnetic material and eddy current losses are observed when current is induced by varying local magnetic field in the metallic material [2.34, 2.77]. All of these losses reveal different frequency dependences. The hysteresis and ferromagnetic losses per cycle are not dependent on the frequency, but on the other hand eddy current losses per cycle increase proportionally with the increase in frequency [2.78]. Therefore, the AC losses per cycle of an HTS coated conductor being the sum of these contributions should increase.

There have been a lot of researches to complete the theoretical behaviour with respect to frequency in HTS CCs. Studies have specified that in HTS CC, the transport AC loss per cycle decreases at first then increases consistently with respect to the frequency [2.79, 2.80]. Experimental and numerical results reveal that the hysteresis losses per cycle are predominant at very low frequencies [2.81, 2.82]. Furthermore, Thakur *et al.* [2.83] mentioned the influence

of the frequency dependent critical current in the Norris equation. Their results show that the hysteresis losses per cycle decrease with the frequency as factor of $f^{-2/n}$, where n is the exponent of *E-J* power law. This factor is true for AC currents even below the critical currents as well as at low frequencies up to 400 Hz.

Several studies have been performed both numerically and experimentally on transport AC losses of HTS CCs at higher frequencies up to 1 kHz with different magnetic substrates. It was discovered that HTS CCs with magnetic substrate have comparatively higher transport losses than those having non-magnetic substrate, and the enrichment of substrate magnetism can increase both hysteresis and eddy current losses [2.78, 2.84]. Chen *et al.* [2.85] analytically calculated the transport AC losses of an HTS core with a copper shell and proposed that the current in the metallic materials should not be defined as the eddy current, but there was not any experimental evidence. Furthermore, numerical and experimental studies were carried out on the frequency dependent AC losses of Bi2223-Ag-sheathed tapes with frequencies up to 2.5 kHz. These studies confirmed that due to increase in frequency, the eddy current per cycle also increases linearly [2.86, 2.87]. This phenomenon has also been verified recently with a comparative experiments of transport AC losses in HTS CC tapes with and without copper stabilisers with frequencies up to 1 kHz and up to 10 kHz numerically [2.88]. All the experiments above were conducted only the frequencies up to 2.5 kHz, this might be due the difficulty of obtaining the precision of AC losses at higher frequencies [2.85].

In a recent study, Zhou *et al.* [2.89] extended the measurement of transport AC losses having magnetic substrate up to 15 kHz and used a spiral voltage loop arrangement in order to achieve the desired measurement precision. They claimed that the theoretic description of frequency dependent AC losses is inadequate especially at much higher frequencies. Furthermore, after a certain "transition frequency" the AC losses per cycle in HTS CCs do not increase but decrease continuously [2.89]. These results have never been reported before, proving that the existing work on frequency dependent AC losses in HTS CCs requires further investigation in order to design and optimise new superconducting electrical devices.

2.5 AC Loss Measurement

In order to measure the AC loss of the superconductors experimentally, there are three common methods: the electric method [2.90], the magnetic method [2.90], and the calorimetric method [2.91]. These methods have been described below along with their advantages and limitations.

2.5.1 Electrical Method

When an AC source transmits the current, the superconductor dissipates some of the energy due to flux creep or self-field loss [2.91]. The energy q_{trans} dissipated during each AC cycle is known as the transport loss. Transport AC loss is expected to be a resistive load and can be estimated through electrical method where the voltage in-phase with current is measured [2.92]. Generally, the current signal is very large while the voltage is very weak, because superconductors operates at very high currents and very small resistance. Due to nonlinear characteristics, the AC loss voltage signal does not have a correct sine waveform, and therefore it is very difficult to measure the AC loss by the voltage signal that should be separated from noise. To eliminate the noise from the voltage signal, lock-in amplifier technique is used where a cancel coil is installed to reduce the noise. The reference current is derived through a non-inductive type resistor which is connected in series with superconductor. The AC loss measurement by electrical method [2.93] is shown in Figure 2.11. All the parameters such as the current (I), the voltage (V) and the phase difference (θ) between the current and voltage are measured using lock-in amplifier technique, and then the AC loss can be estimated by $I \times V \cos\theta$. Although this method provides high level of sensitivity along with a wide range, the measured values cannot be verified. Additionally, the electrical measurement can be easily disturbed by a strong magnetic field.

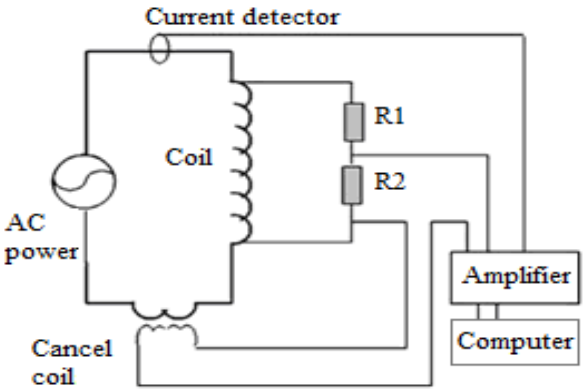

Figure 2.11: AC loss measurement with electrical method and magnetic method [2.93].

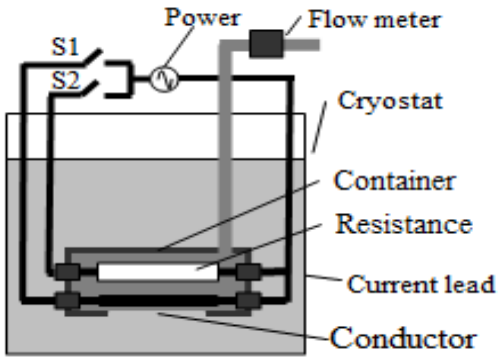

Figure 2.12: AC loss measurement through calorimetric method [2.94].

2.5.2 Magnetic Method

When the superconductor is exposed to the AC magnetic source, energy is dissipated in the superconductor as a result of hysteresis or coupling losses q_{magn}. The magnetic energy dissipated in one cycle is referred as the magnetisation loss [2.91]. The magnetic movement variation in the superconductor is measured by the voltages of the pickup coils around the sample [2.95]. The accuracy of magnetic measurements may be influenced by the detection of small AC transport currents through the magnetic method, as it introduces an additional magnetic field to the superconductor sample that is not caused by the external magnetic field.

2.5.3 Calorimetric Method

The calorimetric method has been described in four distinct approaches: quantifying the amount of evaporated liquid nitrogen from the cryostat, measuring the temperature increase of the superconductor, detecting the temperature difference in the flowing liquid nitrogen, and monitoring the level of liquid nitrogen in the cryostat [2.94], as in Figure 2.12, which shows the schematic diagram of calorimetric method measuring system.

The calorimetric method has the advantage of being insensitive to undesired magnetic field disturbances or alternating currents. Nevertheless, the thermal effects from the external environment, such as Ohmic dissipation in the current leads or heat leakage from the cryostat, may impact the accuracy of the calorimetric method [2.91].

2.6 Importance of Electromagnetic Properties of HTSs Under Rotating Magnetic Field

It can be noticed that all the measurement and modelling techniques presented in the literature were all under one-dimensional (1D) alternating magnetic fields generated by the

transport current in the HTS material itself or through external excitations. In 1D fields, the magnetic flux density vector, B, is restrained to flow in same direction as magnetic field strength, H. However, in power system applications such as three-phase transformer or motors, the magnetic field is generally rotating with a two-dimensional pattern, where *B* and *H* are in different direction, or three-dimensional (3D) pattern, where *B* and *H* are not even in same plane. Studies shows that the power loss caused by 2D or 3D rotating fields mat be different from that caused by 1D alternating magnetic fields. [2.96, 2.97]. Comparison of measured alternating and purely 2D rotational core losses of a soft magnetic composite block sample is shown in Figure 2.13 [2.96].

The impact of a rotating field is found to result in approximately double the loss generated by an equivalent peak-valued alternating field at mid-range flux density. However, when the flux density reaches saturation, the loss caused by the rotating field substantially reduces to levels significantly lower than that caused by an alternating field.. Furthermore, as mentioned in section 2.3 the loss in the HTS material is purely hysteresis loss. Therefore, the effect of rotating magnetic fields on HTS properties, e.g. the hysteresis, must be investigated in order to design the HTS rotating machines.

In 1990, it was reported by Fiorillo and Rietto that rotational core loss in SiFe under various frequency ranges up to 50 Hz comprises of rotational hysteresis, classical eddy current and other anomalous losses which may be similar to alternating core loss [2.98]. This phenomenon was also validated by [2.99] by presenting the core losses of induction motor. In order to calculate the rotational hysteresis loss under an elliptical rotating magnetic flux, linear interpolation has been considered between alternating core losses and purely circular core losses. Various experimental results show that the measured core losses were 20% more than the calculated ones. In 1992, Zhu *et al.* determined the core loss of a motor with permanent magnet using the finite element method incorporating the rotational effects, but due the unavailability of the rotational hysteresis loss data of the material, alternating hysteresis could only be calculated [2.100]. In this study as well, the measured losses were 15% higher than the calculated ones. The improvements were further continued in the rotational hysteresis and the discrepancy was further reduced to less than 10% [2.101].

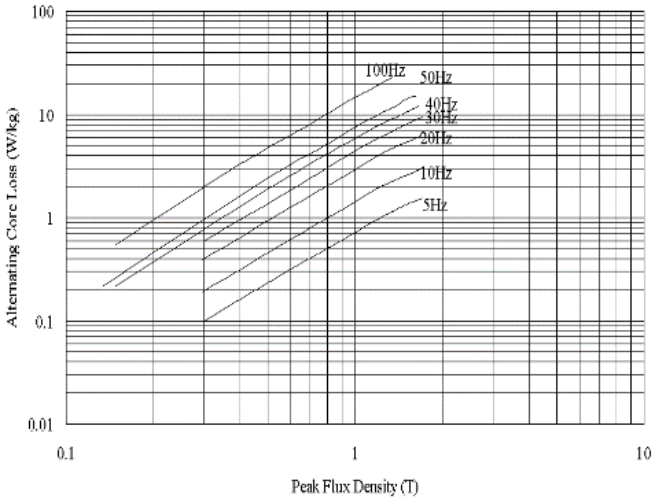

(a)

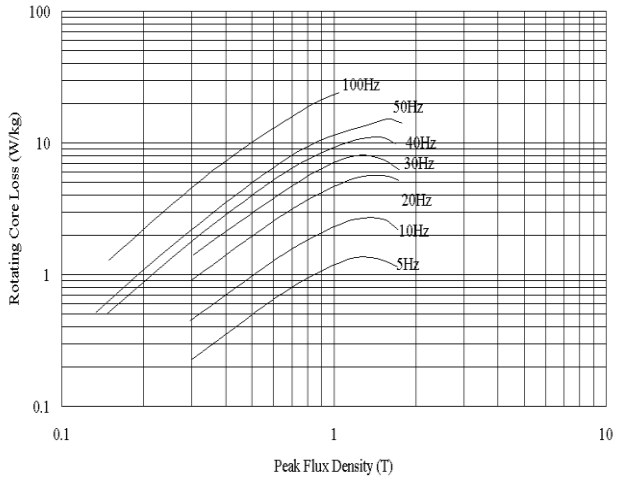

(b)

Figure 2.13: Measured core losses of soft magnetic composite sample with (a) alternating & (b) circularly rotating fluxes [2.96]

Various studies had been performed in the rotational core losses of magnetic material, and researchers have dealt more with rotational hysteresis. The dependence of the alternating and rotational hysteresis loss was first determined for the hard and soft irons using hysteresis measuring apparatus in the year of 1896 [2.102]. The rotational hysteresis loss in both materials is more than alternating hysteresis loss under a range of magnetic flux densities up to 70% of the saturation value. Furthermore, the rotational hysteresis loss is decreased and dropped to zero when the flux density is saturated while on the other hand the alternating core loss remains increasing [2.102] as in Figure 2.14.

For any magnetic material, small area of the hysteresis loop is essential as it reflects the magnetic energy loss per unit volume. It is possible to measure the hysteresis loop area of any magnetic material under rotating and alternating magnetic fields. Both types of the losses can

be measured and calculated by obtaining the magnetic field strength H and magnetic flux density B [2.103].

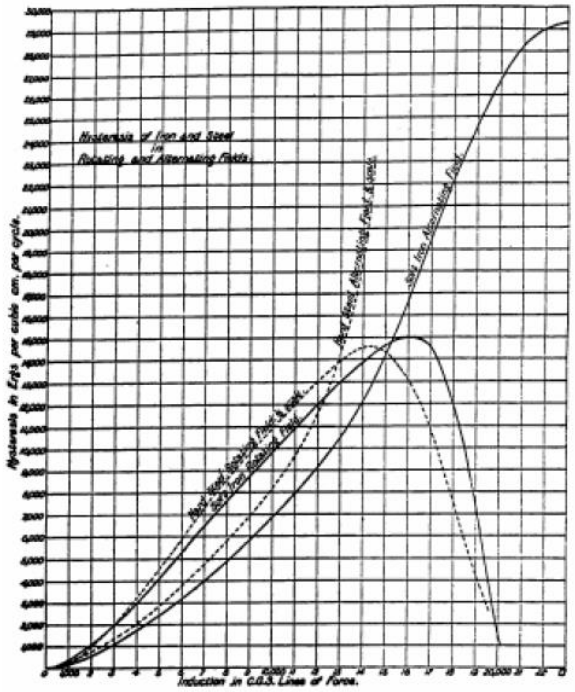

Figure 2.14: Comparison of rotational hysteresis of iron and steel by Baily in 1896 [102]

2.7 Conclusions

This chapter covers the review of advancements in the characterisation and properties modelling of HTS particularly the AC loss along with the Theoretical concepts of superconductivity. Various types of losses have been discussed which contributes towards the total AC losses which shows that the hysteresis losses are the major contributor in the AC losses. Various methods of AC loss measurement are also presented. Moreover, it is identified that the HTS AC loss under the rotating magnetic field is not explicitly presented in the literature, therefore a need for the detailed analysis on this topic is observed. Furthermore, studies have shown that the corresponding AC loss under the rotating magnetic field can be computed by measuring the magnetic flux density and magnetic fields strength.

2.8 References

[2.1] P. A. Abetti and P. Haldar, "One hundred years of superconductivity: science, technology, products, profits and industry structure," *International Journal of Technology Management,* vol. 48, no. 4, pp. 423-447, 2009.

[2.2] D. van Delft, "History and significance of the discovery of superconductivity by Kamerlingh Onnes in 1911," Physica C: Superconductivity, vol. 479, pp. 30-35, 2012.

[2.3] M. N. Wilson, "100 years of superconductivity and 50 years of superconducting magnets," IEEE Transactions on Applied Superconductivity, vol. 22, no. 3, article 3800212, 2012.
[2.4] D. Domínguez, E. Jagla, and C. Balseiro, "Phenomenological theory of the paramagnetic Meissner effect," Physical review letters, vol. 72, no. 17, p. 2773, 1994.
[2.5] C. Rey and A. Malozemoff, "Fundamentals of superconductivity," in Superconductors in the Power Grid: Elsevier, 2015, pp. 29-73.
[2.6] J. Bardeen, L. N. Cooper, and J. R. Schrieffer, "Theory of superconductivity," Physical Review, vol. 108, no. 5, p. 1175, 1957.
[2.7] Z. Zhong, "A study of Critical Currents and Quench in 2G Superconductors under varying magnetic fields," PhD Thesis, University of Cambridge, 2015.
[2.8] M. Zhang, "Study of second-generation high-temperature superconducting coils," University of Cambridge, 2013.
[2.9] L. P. Gor'kov, "Microscopic derivation of the Ginzburg-Landau equations in the theory of superconductivity," Sov. Phys. JETP, vol. 9, no. 6, pp. 1364-1367, 1959.
[2.10] M. Sigrist and K. Ueda, "Phenomenological theory of unconventional superconductivity," Reviews of Modern physics, vol. 63, no. 2, p. 239, 1991.
[2.11] E. Kaldis, E. Liarokapis, and K. A. Müller, High-Tc superconductivity 1996: ten years after the discovery. Springer Science & Business Media, 2012.
[2.12] G. F. Hardy and J. K. Hulm, "The superconductivity of some transition metal compounds," Physical Review, vol. 93, no. 5, p. 1004, 1954.
[2.13] D. C. Larbalestier, "The road to conductors of high temperature superconductors: 10 years do make a difference!," IEEE Transactions on Applied Superconductivity, vol. 7, no. 2, pp. 90-97, 1997.
[2.14] R. Wesche, High-temperature Superconductors: Materials, Properties, and Applications. Springer Science & Business Media, 2013.
[2.15] Wikipedia. "https://en.wikipedia.org/wiki/Superconductivity." (accessed 18 August, 2022).
[2.16] J. G. Bednorz and K. A. Müller, "Possible high Tc superconductivity in the Ba−La−Cu−O system," Zeitschrift für Physik B Condensed Matter, vol. 64, no. 2, pp. 189-193, 1986/06/01 1986, doi: 10.1007/BF01303701.
[2.17] S. Martin, A. T. Fiory, R. Fleming, L. Schneemeyer, and J. V. Waszczak, "Temperature dependence of the resistivity tensor in superconducting Bi 2 Sr 2.2 Ca 0.8 Cu 2 O 8 crystals," Physical Review Letters, vol. 60, no. 21, p. 2194, 1988.
[2.18] D. M. Gann, "Construction as a manufacturing process? Similarities and differences between industrialized housing and car production in Japan," Construction Management & Economics, vol. 14, no. 5, pp. 437-450, 1996.
[2.19] S. Jin, H. Mavoori, C. Bower, and R. Van Dover, "High critical currents in iron-clad superconducting MgB2 wires," Nature, vol. 411, no. 6837, pp. 563-565, 2001.
[2.20] S. Bud'Ko, G. Lapertot, C. Petrovic, C. Cunningham, N. Anderson, and P. Canfield, "Boron isotope effect in superconducting MgB 2," Physical Review Letters, vol. 86, no. 9, p. 1877, 2001.
[2.21] D. Larbalestier et al., "Strongly linked current flow in polycrystalline forms of the superconductor MgB2," Nature, vol. 410, no. 6825, pp. 186-189, 2001.
[2.22] M. W. Rupich et al., "Advances in second generation high temperature superconducting wire manufacturing and R&D at American Superconductor Corporation," Superconductor Science and Technology, vol. 23, no. 1, p. 014015, 2009.
[2.23] A. Malozemoff, "Second-generation high-temperature superconductor wires for the electric power grid," Annual Review of Materials Research, vol. 42, pp. 373-397, 2012.
[2.24] M. W. Rupich, D. T. Verebelyi, W. Zhang, T. Kodenkandath, and X. Li, "Metalorganic deposition of YBCO films for second-generation high-temperature superconductor wires," MRS bulletin, vol. 29, no. 8, pp. 572-578, 2004.
[2.25] G. Blatter, M. V. Feigel'man, V. B. Geshkenbein, A. I. Larkin, and V. M. Vinokur, "Vortices in high-temperature superconductors," Reviews of Modern Physics, vol. 66, no. 4, p. 1125, 1994.
[2.26] H. Eisaki et al., "Effect of chemical inhomogeneity in bismuth-based copper oxide superconductors," Physical Review B, vol. 69, no. 6, p. 064512, 2004.
[2.27] C. Antoine, "Materials and surface aspects in the development of SRF Niobium cavities," 2012.
[2.28] H. Suhl, B. Matthias, and L. Walker, "Bardeen-Cooper-Schrieffer theory of superconductivity in the case of overlapping bands," Physical Review Letters, vol. 3, no. 12, p. 552, 1959.
[2.29] R. M. Scanlan, A. P. Malozemoff, and D. C. Larbalestier, "Superconducting materials for large scale applications," Proceedings of the IEEE, vol. 92, no. 10, pp. 1639-1654, 2004.
[2.30] P. W. Anderson and Y. Kim, "Hard superconductivity: theory of the motion of Abrikosov flux lines," Reviews of Modern Physics, vol. 36, no. 1, p. 39, 1964.

[2.31] R. P. Huebener, "Lorentz Force and Flux Motion," in Magnetic Flux Structures in Superconductors: Extended Reprint of a Classic Text. Berlin, Heidelberg: Springer Berlin Heidelberg, 2001, pp. 121-143.
[2.32] W. Buckel and R. Kleiner, "Superconductivity: Fundamentals and Applications: Wiley-VCH, Weinheim, 2-nd Edition," 2004.
[2.33] V. Dusastre, Materials for sustainable energy: a collection of peer-reviewed research and review articles from Nature Publishing Group. World Scientific, 2010.
[2.34] F. Grilli, E. Pardo, A. Stenvall, D. N. Nguyen, W. Yuan, and F. Gömöry, "Computation of losses in hts under the action of varying magnetic fields and currents," IEEE Transactions on Applied Superconductivity, vol. 24, no. 1, pp. 78-110, 2014, doi: 10.1109/TASC.2013.2259827.
[2.35] J. X. Jin et al., "HTS power devices and systems: principles, characteristics, performance, and efficiency," IEEE Transactions on Applied Superconductivity, vol. 26, no. 7, pp. 1-26, 2016, doi: 10.1109/TASC.2016.2602346.
[2.36] J. Lloberas, A. Sumper, M. Sanmarti, and X. Granados, "A review of high temperature superconductors for offshore wind power synchronous generators," Renewable and Sustainable Energy Reviews, vol. 38, pp. 404-414, 2014/10/01/ 2014, doi: https://doi.org/10.1016/j.rser.2014.05.003.
[2.37] R. Dommerque et al., "First commercial medium voltage superconducting fault-current limiters: production, test and installation," Superconductor Science and Technology, vol. 23, no. 3, p. 034020, 2010/02/22 2010, doi: 10.1088/0953-2048/23/3/034020.
[2.38] S. Dai et al., "Development and test of a 220 kV/1.5 kA resistive type superconducting fault current limiter," Physica C: Superconductivity and its Applications, vol. 565, p. 1253501, 2019/10/15/ 2019, doi: https://doi.org/10.1016/j.physc.2019.06.004.
[2.39] S. Hellmann, M. Abplanalp, S. Elschner, A. Kudymow, and M. Noe, "Current Limitation Experiments on a 1 MVA-Class Superconducting Current Limiting Transformer," IEEE Transactions on Applied Superconductivity, vol. 29, no. 5, pp. 1-6, 2019, doi: 10.1109/TASC.2019.2906804.
[2.40] L. Xiao et al., "Development of the world's first HTS power substation," IEEE Transactions on applied superconductivity, vol. 22, no. 3, pp. 5000104-5000104, 2011.
[2.41] C. Lee et al., "Progress of the first commercial project of high-temperature superconducting cables by KEPCO in Korea," Superconductor Science and Technology, vol. 33, no. 4, p. 044006, 2020.
[2.42] J.-y. Yoon, S. R. Lee, and J. Y. Kim, "Application methodology for 22.9 kV HTS cable in metropolitan city of South Korea," IEEE transactions on applied superconductivity, vol. 17, no. 2, pp. 1656-1659, 2007.
[2.43] B. Yang, J. Kang, S. Lee, C. Choi, and Y. Moon, "Qualification test of a 80 kV 500 MW HTS DC cable for applying into real grid," IEEE Transactions on Applied Superconductivity, vol. 25, no. 3, pp. 1-5, 2015.
[2.44] S. J. Lee, M. Park, I.-K. Yu, Y. Won, Y. Kwak, and C. Lee, "Recent status and progress on HTS cables for AC and DC power transmission in Korea," IEEE Transactions on Applied Superconductivity, vol. 28, no. 4, pp. 1-5, 2018.
[2.45] W. Yuan, S. Venuturumilli, Z. Zhang, Y. Mavrocostanti, and M. Zhang, "Economic feasibility study of using high-temperature superconducting cables in UK's electrical distribution networks," IEEE Transactions on Applied Superconductivity, vol. 28, no. 4, pp. 1-5, 2018.
[2.46] P. F. Ribeiro, B. K. Johnson, M. L. Crow, A. Arsoy, and Y. Liu, "Energy storage systems for advanced power applications," Proceedings of the IEEE, vol. 89, no. 12, pp. 1744-1756, 2001, doi: 10.1109/5.975900.
[2.47] P. Zhao, J. Wang, and Y. Dai, "Capacity allocation of a hybrid energy storage system for power system peak shaving at high wind power penetration level," Renewable Energy, vol. 75, pp. 541-549, 2015.
[2.48] Y. Kwon et al., "Performance test of a 1 MW class HTS synchronous motor for industrial application," Physica C: Superconductivity, vol. 468, no. 15-20, pp. 2081-2086, 2008.
[2.49] K. Sivasubramaniam et al., "Development of a high speed HTS generator for airborne applications," IEEE Transactions on Applied Superconductivity, vol. 19, no. 3, pp. 1656-1661, 2009.
[2.50] B. Gamble, G. Snitchler, and T. MacDonald, "Full power test of a 36.5 MW HTS propulsion motor," IEEE Transactions on Applied Superconductivity, vol. 21, no. 3, pp. 1083-1088, 2010.
[2.51] C. Y. Lee et al., "Conceptual design of superconducting linear synchronous motor for 600-km/h wheel-type railway," IEEE Transactions on Applied superconductivity, vol. 24, no. 3, pp. 1-4, 2013.
[2.52] C.-B. Park, C.-Y. Lee, S. Yoon, and S. Kim, "Development of a small-scale superconducting LSM using Gd-Ba-Cu-O high-temperature superconducting wire," IEEE Transactions on Energy Conversion, vol. 31, no. 4, pp. 1250-1256, 2016.
[2.53] B. Liu, R. Badcock, H. Shu, and J. Fang, "A superconducting induction motor with a high temperature superconducting armature: Electromagnetic theory, design and analysis," Energies, vol. 11, no. 4, p. 792, 2018.

[2.54] D. Sekiguchi et al., "Trial test of fully HTS induction/synchronous machine for next generation electric vehicle," IEEE Transactions on Applied Superconductivity, vol. 22, no. 3, pp. 5200904-5200904, 2011.
[2.55] X. Song et al., "A pole pair segment of a 2-MW high-temperature superconducting wind turbine generator," IEEE Transactions on Applied Superconductivity, vol. 27, no. 4, pp. 1-5, 2017.
[2.56] X. Song et al., "Experimental validation of a full-size pole pair set-up of an MW-Class Direct Drive Superconducting Wind Turbine Generator," IEEE Transactions on Energy Conversion, 2019.
[2.57] F. Grilli, E. Pardo, A. Stenvall, D. N. Nguyen, W. Yuan, and F. Gömöry, "Computation of losses in HTS under the action of varying magnetic fields and currents," IEEE Transactions on Applied Superconductivity, vol. 24, no. 1, pp. 78-110, 2013.
[2.58] M. P. Oomen, "AC loss in superconducting tapes and cables," 2001.
[2.59] W. Norris, "Calculation of hysteresis losses in hard superconductors carrying AC: isolated conductors and edges of thin sheets," Journal of Physics D: Applied Physics, vol. 3, no. 4, p. 489, 1970.
[2.60] B. Shen, "Study of second generation high temperature superconductors: electromagnetic characteristics and AC loss analysis," University of Cambridge, 2018.
[2.61] R. Duckworth, M. Gouge, J. Lue, C. Thieme, and D. Verebelyi, "Substrate and stabilisation effects on the transport AC losses in YBCO coated conductors," IEEE Transactions on Applied Superconductivity, vol. 15, no. 2, pp. 1583-1586, 2005.
[2.62] M. Wang et al., "An effective way to reduce AC loss of second-generation high temperature superconductors," Superconductor Science and Technology, vol. 32, no. 1, p. 01LT01, 2018/11/16 2018, doi: 10.1088/1361-6668/aaee05.
[2.63] W. J. Carr and C. E. Oberly, "Filamentary YBCO conductors for AC applications," IEEE Transactions on Applied Superconductivity, vol. 9, no. 2, pp. 1475-1478, 1999, doi: 10.1109/77.784671.
[2.64] K. Suzuki et al., "Development of scribing process of coated conductors for reduction of AC losses," Physica C: Superconductivity, vol. 468, no. 15, pp. 1579-1582, 2008/09/15/ 2008, doi: https://doi.org/10.1016/j.physc.2008.05.076.
[2.65] R. Nast et al., "Influence of laser striations on the properties of coated conductors," Journal of Physics: Conference Series, vol. 507, no. 2, p. 022023, 2014/05/12 2014, doi: 10.1088/1742-6596/507/2/022023.
[2.66] E. Demenčík et al., "AC magnetisation loss and transverse resistivity of striated YBCO coated conductors," IEEE Transactions on Applied Superconductivity, vol. 25, no. 3, pp. 1-5, 2015, doi: 10.1109/TASC.2014.2381561.
[2.67] N. Amemiya et al., "AC loss reduction of YBCO coated conductors by multifilamentary structure," Superconductor Science and Technology, vol. 17, no. 12, pp. 1464-1471, 2004/11/03 2004, doi: 10.1088/0953-2048/17/12/018.
[2.68] M. Majoros, B. A. Glowacki, A. M. Campbell, G. A. Levin, and P. N. Barnes, "Transport AC losses in striated YBCO coated conductors," Journal of Physics: Conference Series, vol. 43, pp. 564-567, 2006/06/01 2006, doi: 10.1088/1742-6596/43/1/139.
[2.69] O. Tsukamoto and M. Ciszek, "AC magnetisation losses in striated YBCO-123/Hastelloy coated conductors," Superconductor Science and Technology, vol. 20, no. 10, pp. 974-979, 2007/08/29 2007, doi: 10.1088/0953-2048/20/10/014.
[2.70] D. Xing et al., "AC Loss comparison between multifilament and nonstriated YBCO coils designed for HTS propulsion motors," IEEE Transactions on Applied Superconductivity, vol. 27, no. 4, pp. 1-5, 2017, doi: 10.1109/TASC.2017.2669156.
[2.71] F. Grilli and A. Kario, "How filaments can reduce AC losses in HTS coated conductors: a review," Superconductor Science and Technology, vol. 29, no. 8, p. 083002, 2016/07/05 2016, doi: 10.1088/0953-2048/29/8/083002.
[2.72] W. Goldacker et al., "ROEBEL assembled coated conductors (RACC): preparation, properties and progress," IEEE Transactions on Applied Superconductivity, vol. 17, no. 2, pp. 3398-3401, 2007, doi: 10.1109/TASC.2007.899417.
[2.73] N. J. Long et al., "Narrow strand YBCO Roebel cable for lowered AC loss," Journal of Physics: Conference Series, vol. 97, p. 012280, 2008/02/01 2008, doi: 10.1088/1742-6596/97/1/012280.
[2.74] W. Goldacker et al., "Status of high transport current ROEBEL assembled coated conductor cables," Superconductor Science and Technology, vol. 22, no. 3, p. 034003, 2009/01/28 2009, doi: 10.1088/0953-2048/22/3/034003.
[2.75] S. Terzieva et al., "Investigation of the effect of striated strands on the AC losses of 2G Roebel cables," Superconductor Science and Technology, vol. 24, no. 4, p. 045001, 2011/01/27 2011, doi: 10.1088/0953-2048/24/4/045001.
[2.76] Z. Li et al., "Development of a novel soldered-stacked-square (3S) HTS wire using 2G narrow tapes with 1 mm width," IEEE Transactions on Applied Superconductivity, vol. 27, no. 4, pp. 1-4, 2017, doi: 10.1109/TASC.2016.2634326.

[2.77] M. Majoros, L. Ye, A. V. Velichko, T. A. Coombs, M. D. Sumption, and E. W. Collings, "Transport AC losses in YBCO coated conductors," Superconductor Science and Technology, vol. 20, no. 9, pp. S299-S304, 2007/08/23 2007, doi: 10.1088/0953-2048/20/9/s27.

[2.78] G. Liu, G. Zhang, H. Yu, L. Jing, L. Ai, and Q. Liu, "Experimental and numerical study of frequency-dependent transport loss in YBa2Cu3O7–δ coated conductors with ferromagnetic substrate and copper stabilizer," Journal of Applied Physics, vol. 121, no. 24, p. 243902, 2017/06/28 2017, doi: 10.1063/1.4989807.

[2.79] F Gömöry, E Janíková, and J. Šouc, "Resistive losses in a high-tcwire carrying ac current larger than Ic," Superconductor Science and Technology, vol. 15, no. 9, pp. 1345-1352, 2002/08/20 2002, doi: 10.1088/0953-2048/15/9/313.

[2.80] R. Inoue, D. Miyagi, M. Tsuda, and H. Matsuki, "AC loss characteristics in kilohertz frequency band of a high-temperature superconductor coil for a wireless power transmission system," IEEE Transactions on Applied Superconductivity, vol. 27, no. 4, pp. 1-5, 2017, doi: 10.1109/TASC.2017.2658943.

[2.81] M. Polak, J. Kvitkovic, P. Mozola, E. Usak, P. N. Barnes, and G. A. Levin, "Frequency dependence of hysteresis loss in YBCO tapes," Superconductor Science and Technology, vol. 20, no. 9, pp. S293-S298, 2007/08/23 2007, doi: 10.1088/0953-2048/20/9/s26.

[2.82] J. Yuan, J. Fang, P. Qu, G. X. Shen, and Z. H. Han, "Study of frequency dependent AC loss in Bi-2223 tapes used for gradient coils in magnetic resonance imaging," Physica C: Superconductivity, vol. 424, no. 1, pp. 72-78, 2005/08/01/ 2005, doi: https://doi.org/10.1016/j.physc.2005.04.022.

[2.83] K. P. Thakur, A. Raj, E. H. Brandt, J. Kvitkovic, and S. V. Pamidi, "Frequency-dependent critical current and transport ac loss of superconductor strip and Roebel cable," Superconductor Science and Technology, vol. 24, no. 6, p. 065024, 2011/04/21 2011, doi: 10.1088/0953-2048/24/6/065024.

[2.84] G. Liu et al., "Influence of substrate magnetism on frequency-dependent transport loss in HTS-coated conductors," IEEE Transactions on Applied Superconductivity, vol. 27, no. 8, pp. 1-7, 2017, doi: 10.1109/TASC.2017.2748979.

[2.85] D. X. Chen, "AC susceptibility of a long cylinder with a hard superconducting core and normal conducting shell," Superconductor Science and Technology, vol. 17, no. 3, pp. 417-422, 2004/01/20 2004, doi: 10.1088/0953-2048/17/3/020.

[2.86] C. M. Friend, C. Beduz, B. Dutoit, R. Navarro, E. Cereda, and J. Alonso-Llorente, "A European project on the AC losses of Bi-2223 tapes for power applications," IEEE Transactions on Applied Superconductivity, vol. 9, no. 2, pp. 1165-1168, 1999, doi: 10.1109/77.783506.

[2.87] N. Nibbio, S. Stavrev, and B. Dutoit, "Effect of the sheath resistivity and tape geometry on eddy current loss in Bi(2223) tapes," Physica C: Superconductivity, vol. 310, no. 1, pp. 208-212, 1998/12/01/ 1998, doi: https://doi.org/10.1016/S0921-4534(98)00463-8.

[2.88] B. Shen et al., "Investigation and comparison of AC losses on stabilizer-free and copper stabilizer HTS tapes," Physica C: Superconductivity and its Applications, vol. 541, pp. 40-44, 2017/10/15/ 2017, doi: https://doi.org/10.1016/j.physc.2017.07.013.

[2.89] P. Zhou, G. Ma, and L. Quéval, "Transition frequency of transport ac losses in high temperature superconducting coated conductors," Journal of Applied Physics, vol. 126, no. 6, p. 063901, 2019.

[2.90] H. Daffix and P. Tixador, "Electrical AC loss measurements in superconducting coils," IEEE Transactions on Applied Superconductivity, vol. 7, no. 2, pp. 286-289, 1997, doi: 10.1109/77.614486.

[2.91] M. Oomen, "AC loss in superconducting tapes and cables PhD Thesis University of Twente," Enschede, The Netherlands, webpage http://www. ub. utwente. nl/webdoc/docs/tn. shtml, 2000.

[2.92] Y. Chen, "AC loss analysis and measurement of second generation high temperature superconductor racetrack coils," University of Cambridge, 2014.

[2.93] H.-J. Kim et al., "AC loss characteristics of Bi-2223 HTS tapes under bending," Physica C: Superconductivity and its applications, vol. 445, pp. 768-771, 2006.

[2.94] H. Huang, C. Zhang, and S. Yan, "Calorimetric measurement of AC losses of superconducting magnet," Acta Physica Temperature Humilis Sinica, vol. 3, no. 1, pp. 42-46, 1981.

[2.95] J. Šouc, E. Pardo, M. Vojenčiak, and F. Gömöry, "Theoretical and experimental study of AC loss in high temperature superconductor single pancake coils," Superconductor Science and Technology, vol. 22, no. 1, p. 015006, 2008.

[2.96] Y. Guo, J. Zhu, and J. Zhong, "Measurement and modelling of magnetic properties of soft magnetic composite material under 2D vector magnetisations," Journal of magnetism and magnetic materials, vol. 302, no. 1, pp. 14-19, 2006.

[2.97] Y. G. Guo, J. G. Zhu, and J. J. Zhong, "Measurement and modelling of magnetic properties of soft magnetic composite material under 2D vector magnetisations," Journal of Magnetism and Magnetic Materials, vol. 302, no. 1, pp. 14-19, 2006/07/01/ 2006, doi: https://doi.org/10.1016/j.jmmm.2005.08.023.

[2.98] F. Fiorillo and A. Rietto, "Rotational versus alternating hysteresis losses in nonoriented soft magnetic laminations," Journal of Applied Physics, vol. 73, no. 10, pp. 6615-6617, 1993.
[2.99] G. Bertotti and M. Pasquale, "Physical interpretation of induction and frequency dependence of power losses in soft magnetic materials," IEEE Transactions on Magnetics, vol. 28, no. 5, pp. 2787-2789, 1992.
[2.100] J. Zhu, V. Ramsden, and P. Watterson, "Finite element calculation of core losses in motors with nonsinusoidal fields," in Proc. IEEE International Conference of Electrical Machines, 1992, pp. 182-1186.
[2.101] J. Zhu and V. Ramsden, "Core loss modelling in rotational electrical machines," Proc. of ICEMA, vol. 93, pp. 14-16, 1993.
[2.102] F. G. Baily, "The hysteresis of iron and steel in a rotating magnetic field," Philosophical Transactions of the Royal Society of London. Series A, Containing Papers of a Mathematical or Physical Character, no. 187, pp. 715-746, 1896.
[2.103] Y. Guo, J. G. Zhu, Z. W. Lin, and J. J. Zhong, "Measurement and modeling of core losses of soft magnetic composites under 3-D magnetic excitations in rotating motors," IEEE Transactions on Magnetics, vol. 41, no. 10, pp. 3925-3927, 2005.

CHAPTER 3 **Numerical Modelling and Theoretical Analysis**

3.1 Introduction

Several models for determining the AC loss, field distributions and current density of High Temperature Superconductors (HTS) have been developed and are detailed in depth in the sections below.

3.2 Critical State Model

The critical state model is a mathematical model for describing superconducting phenomena, which was developed empirically based on the results of macroscopic superconducting experiments. It is a straightforward method used to model superconductivity [3.1]. The critical state model is the simplest and most commonly used superconductivity model, which assumes that when low magnetic fields or currents are applied, only the outer layer of the superconducting material enters the critical state, while the inner region remains in the virgin (normal) state [3.1, 3.2]. Understanding the engineering applications of superconductivity using the critical state model is a basic approach. There are two critical state models that are widely used, namely the Bean model proposed by C. Bean [3.3] and the Kim model proposed by Y. Kim [3.4], which are briefly described below.

One of the simplest critical state models is the Bean Model, which relies on the following two assumptions [3.3, 3.5]:

- The magnetic field has no effect on the critical current J.
- Whenever a superconductor crosses into its critical state, a critical current of $\pm J_c$ flows through it, whereas in its normal state, no current flows.

The Bean approximation forecasts that the values for shielding or trapped current are either 0 or $\pm J_c$. As depicted in Figure 3.1, the Bean model can be represented by a superconducting slab with an infinitely long y-z plane that is exposed to a z-direction magnetic field. In the presence of a z-directionally applied magnetic field, induced currents will flow over the surface of the geometry. Assuming that the superconductor is indefinitely long in the y-z plane, the surface current in the x- direction is small relative to the y direction. Therefore, it is believed that currents exclusively flow in the y- direction (two-way) [3.3, 3.5].

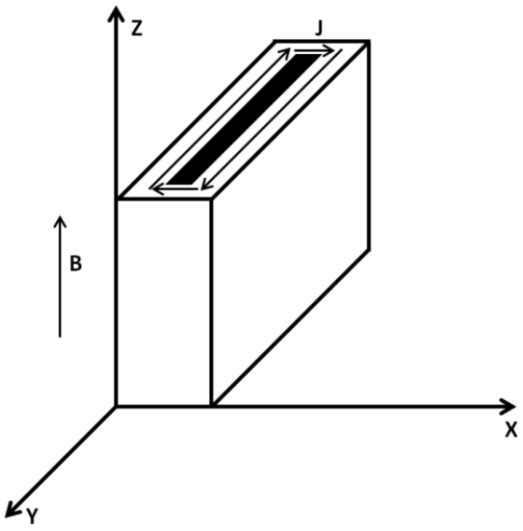

Figure 3.1: Superconducting slab with infinite length in the y-z plane which is in the presence of an applied magnetic field in the z direction.

When an applied magnetic field H_a steadily increases, screening currents are created at the slab's surface and progressively infiltrate the slab's interior. This results in a magnetic field that is perpendicular to the applied field. The deep interior of the slab is insulated from the external field, as shown in Figure 3.2 (a). The slope is the derivative of the critical current with respect to the magnetic field within the slab.

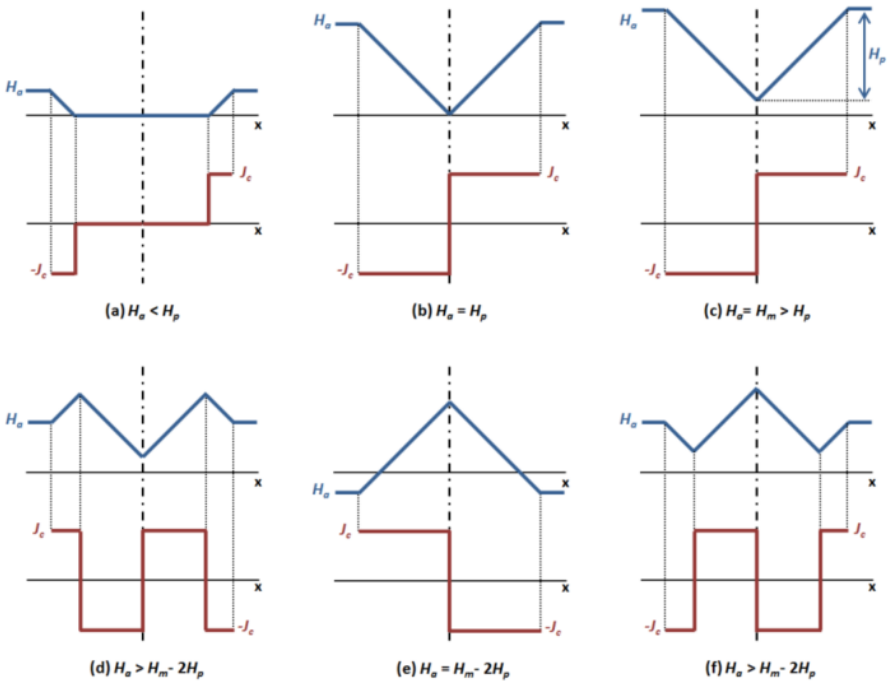

Figure 3.2: Magnetic field and current profiles for the superconducting slab presented in Figure 3.1. [3.3, 3.5]

3.3 The Kim Model

Kim expanded the Bean model in 1962 by integrating temperature and magnetic field, both of which influence the critical current. In the Kim model, the superconducting material's critical current J_c is no longer a constant, but a variable [3.4, 3.6].

$$J_c(B) = \frac{\alpha(T)}{B_0 + B} = J_{c0}(T) = \frac{1}{1 + \frac{B}{B_0}} \tag{3.1}$$

where B_0 is a constant associated with superconducting material:

$$J_{c0}(T) = \frac{\alpha(T)}{B_0} \tag{3.2}$$

The expression for the temperature dependence α could be expressed as:

$$\alpha = \frac{1}{d}(a - bT) \tag{3.3}$$

$$\frac{a}{b} \leq T_c \tag{3.4}$$

where d is a constant that depends on the superconductor's microstructure. There are detailed comparisons between the Bean model and the Kim model in [3.4, 3.6].

3.4 E-J Power Law

While Maxwell's equations are always valid, they need to be adjusted appropriately for use with a physical model using superconducting materials. The critical state model has demonstrated sufficient precision for application to LTSs [3.7]. However, the critical current density J_c for HTS materials is an ill-defined number. Scientists have determined the *E-J* constitutive power law for Type II superconductors based on experimental observations. Currently, the *E-J* power law is the most used method for describing the electrical properties of Type II superconductors, as stated by [3.7, 3.8]:

$$E = E_0 \left(\frac{J}{J_c}\right)^n \tag{3.5}$$

where E_0 is set to be 10^{-4} Vm^{-1}, J_c is the critical current density determined at the moment the electric field reaches E_0, and n is a measurable parameter used to match the *E-J* power equation [3.9] based on experimental findings from material properties and microstructures.

Figure 3.3 depicts the relationship between E/E_0 and J/J_0 for various n values. The pure Ohmic scenario has n = 1, but the critical state model has n =∞. The value of n for Type II superconductors typically falls between 15 and 30. n for N_bT_i ranges from 40 to 80. The standard YBCO value, n = 21, was chosen for the modelling and design in this work [3.10].

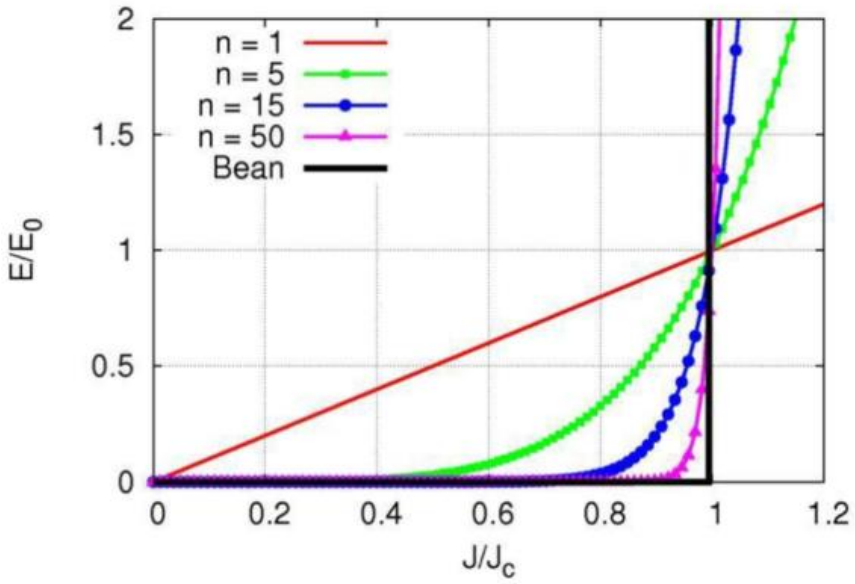

Figure 3.3: *E-J* power law with different *n* factors [3.26].

3.5 General H-Formulation

Maxwell's equations are commonly used to compute the current and magnetic field distribution for conventional electromagnetic problems. Maxwell's equations can still be used to solve superconducting problems, but extra equations are required to describe the material properties. The H-formulation is a technique utilised to characterise superconductivity, which calculates the distribution of induced current and magnetic field within the framework of the *E-J* power law. This method combines Maxwell's equations with the *E-J* power law to expand the framework to a superconducting formulation [3.9, 3.11].

Ampere's Law describes the connection between current and field:

$$\nabla \times H = J \tag{3.6}$$

where H represents the magnetic field strength and J represents the current density. Faraday's Law is expressed as follows:

$$\nabla \times E = -\frac{\partial B}{\partial t} \tag{3.7}$$

By means of the constitution law:

$$B = \mu_0 \mu_r H \tag{3.8}$$

where μ_0 and μ_r are the vacuum permeability and relative permeability of the material respectively. To determine the relationship between electric field and current density, we use the electrical resistivity ρ of specific materials:

$$E = \rho J \tag{3.9}$$

The E-J power law has previously been derived as:

$$E = E_0 \left(\frac{J}{J_c}\right)^n \tag{3.10}$$

In accordance with Equations (3.6) through (3.10), after adjustment:

$$\mu_0 \mu_r \frac{\partial H}{\partial t} + \nabla \times (\rho \nabla \times H) = 0 \tag{3.11}$$

Equation (3.11), which is known as the generic H-formulation, is a single equation with a single known value of *H*.

3.6 Two-dimensional (2D) H-formulation Models

As depicted in Figure 3.4, a plane on paper (x and y plane) is perpendicular to an infinitely long z-direction space. A superconducting long rod (rectangular cross section) is subjected to a uniform y-direction magnetic field (H_y) in the z direction [3.11].

The 2D Cartesian coordinates model consists of two variables whose definitions are $H = [H_x, H_y]$. As depicted in Figure 3.4, the superconductor current, J_z, only flows in the z direction in this 2D model [3.11]. Additionally, the electric field E_z is in the z direction. Therefore, $E_z = \rho J_z$, where ρ is the material's resistivity. For the 2D model, Ampere's Law can be represented as:

$$J_z = \frac{\partial H_y}{\partial x} - \frac{\partial H_x}{\partial y} \tag{3.12}$$

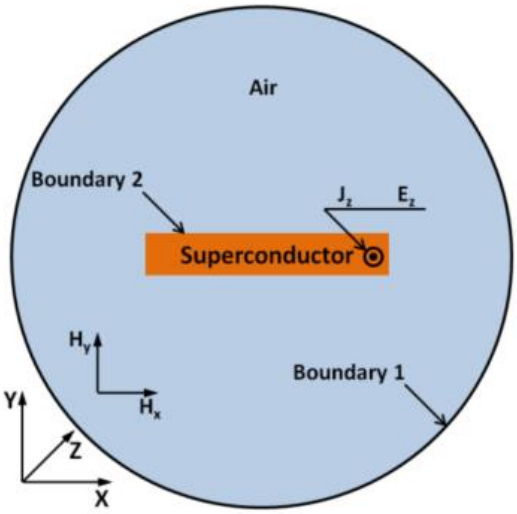

Figure 3.4: Boundaries and subdomains of two-dimensional (2D) H-formulation Models.

Substituting H = [H_x, H_y] in Equation (3.12), we can write Faraday's Law for this model as:

$$\begin{bmatrix} \frac{\partial E_z}{\partial y} \\ -\frac{\partial E_z}{\partial x} \end{bmatrix} = -\mu_0\mu_r \begin{bmatrix} \frac{\partial H_x}{\partial t} \\ -\frac{\partial H_y}{\partial t} \end{bmatrix} \tag{3.13}$$

Using the resistivity relationship Equation (3.10) and the *E-J* power law Equation (3.11), we derive two equations with two unknowns, H_x and H_y, in place of the electric field E_z. This expression resembles Equation (3.12):

$$\begin{bmatrix} \dfrac{\partial\left(E_0\left(\dfrac{\frac{\partial H_y}{\partial x}-\frac{\partial H_x}{\partial y}}{J_c}\right)^n\right)}{\partial y} \\ -\dfrac{\partial\left(E_0\left(\dfrac{\frac{\partial H_y}{\partial x}-\frac{\partial H_x}{\partial y}}{J_c}\right)^n\right)}{\partial x} \end{bmatrix} = -\mu_0\mu_r \begin{bmatrix} \dfrac{\partial H_x}{\partial t} \\ -\dfrac{\partial H_y}{\partial t} \end{bmatrix} \tag{3.14}$$

Equation (3.15), which applies to superconducting materials, contains two partial differential equations (PDEs) and two dependent variables. Besides air, the general ohmic connection is applied to all other normal areas. All of this modelling is possible using FEM tools like COMSOL [3.11].

3.7 Three-dimensional (3D) H-formulation Models

Similar to 2D H-formulation models, 3D models feature three dependent variables for the magnetic field: H_x, H_y, and H_z, in addition to three dependent variables for the 3D current density: J_x, J_y, J_z, as well as the electric field: E_x, E_y, E_z.

The 3D H-formulation model is capable of simulating all common geometries as well as irregularly shaped superconductors. Moreover, 3D models are required to investigate the difficult superconducting problem in which the current and magnetic fields are not perpendicular to each other [3.12, 3.13]. For the 3D model, Ampere's Law can be written as:

$$\begin{bmatrix} J_x \\ J_y \\ J_z \end{bmatrix} = \begin{bmatrix} \dfrac{\partial H_z}{\partial y}-\dfrac{\partial H_y}{\partial z} \\ \dfrac{\partial H_x}{\partial z}-\dfrac{\partial H_z}{\partial x} \\ \dfrac{\partial H_y}{\partial x}-\dfrac{\partial H_x}{\partial y} \end{bmatrix} \tag{3.15}$$

By substituting $H = [H_x, H_y, H_z]$ and $E = [E_x, E_y, E_z]$ into Faraday's Law, it can be written for the 3D model as follows:

$$\begin{bmatrix} \frac{\partial E_z}{\partial y} - \frac{\partial E_y}{\partial z} \\ \frac{\partial E_x}{\partial z} - \frac{\partial E_z}{\partial x} \\ \frac{\partial E_y}{\partial x} - \frac{\partial E_x}{\partial y} \end{bmatrix} = -\mu_0 \mu_r \begin{bmatrix} \frac{\partial H_x}{\partial t} \\ \frac{\partial H_y}{\partial t} \\ \frac{\partial H_z}{\partial t} \end{bmatrix} \tag{3.16}$$

Using the norm terms for *H*, *J* and *E*:

$$H_{norm} = \sqrt{{H_x}^2 + {H_y}^2 + {H_z}^2} \tag{3.17}$$

$$J_{norm} = \sqrt{{J_x}^2 + {J_y}^2 + {J_z}^2} \tag{3.18}$$

$$E_{norm} = \sqrt{{E_x}^2 + {E_y}^2 + {E_z}^2} \tag{3.19}$$

The 3D model *E-J* power law can be defined as:

$$\begin{bmatrix} E_x \\ E_y \\ E_z \end{bmatrix} = E_0 \begin{bmatrix} \frac{J_x}{J_{norm}} \left(\frac{J_{norm}}{J_c}\right)^n \\ \frac{J_y}{J_{norm}} \left(\frac{J_{norm}}{J_c}\right)^n \\ \frac{J_y}{J_{norm}} \left(\frac{J_{norm}}{J_c}\right)^n \end{bmatrix} \tag{3.20}$$

In accordance with Equations (3.16) to (3.21), the 3D-formulation equations can be found with three dependent variables $H = [H_x, H_y, H_z]$, which can also be simulated using FEM software such as COMSOL [3.11].

3.8 Boundary Conditions

When simulating the behaviour of superconductors using numerical methods, accurate specification of boundary conditions is crucial. In the context of high-temperature superconductors (HTS), the choice of boundary conditions at the interface between the superconductor and other materials significantly affects the accuracy and reliability of the

simulations. For instance, in simulations involving HTS coated conductors in contact with normal conductors, appropriate contact interfaces should be defined to facilitate the transfer of physical quantities such as heat, current, or magnetic fields between the materials. The contact interfaces should account for factors such as contact resistance or thermal contact conductance if applicable. Additionally, the selection of boundary conditions depends on the specific phenomena being modelled. For example, when studying the performance of HTS devices, boundary conditions can be set to simulate the appropriate voltage or current inputs. By carefully considering and correctly defining the boundary conditions in simulation software like COMSOL Multiphysics, researchers can accurately capture the behaviour of HTS materials and gain valuable insights into their applications and performance characteristics.

3.9 Conclusions

To measure the AC losses of HTS conductors experimentally, the electrical method is vastly used. While in case of the numerical modelling techniques, the H-formulation FEM model has been used by the majority of researchers due to its strong capability of AC loss estimation for the variety HTS topologies under various operating scenarios and generating accurate results compared to the experimental data. Vast majority of the AC loss models published in the literature have used to COMSOL Multiphysics for the FEM due to its easy implementation.

3.10 References

[3.1] A. Morandi and M. Fabbri, "A unified approach to the power law and the critical state modeling of superconductors in 2D," *Superconductor Science and Technology,* vol. 28, no. 2, p. 024004, 2014.

[3.2] C. E. Sobrero, M. T. Malachevsky, and A. Serquis, "Core microstructure and strain state analysis in MgB2 wires with different metal sheaths," *Advances in Condensed Matter Physics,* vol. 2015, 2015.

[3.3] C. P. Bean, "Magnetisation of hard superconductors," *Physical Review Letters,* vol. 8, no. 6, p. 250, 1962.

[3.4] Y. Kim, C. Hempstead, and A. Strnad, "Critical persistent currents in hard superconductors," *Physical Review Letters,* vol. 9, no. 7, p. 306, 1962.

[3.5] C. P. Bean, "Magnetisation of high-field superconductors," *Reviews of Modern Physics,* vol. 36, no. 1, p. 31, 1964.

[3.6] Y. Kim, C. Hempstead, and A. Strnad, "Magnetisation and critical supercurrents," *Physical Review,* vol. 129, no. 2, p. 528, 1963.

[3.7] I. Falorio, E. A. Young, and Y. Yang, "Flux pinning distribution and EJ characteristics of 2G YBCO Tapes," in *Journal of Physics: Conference Series*, 2014, vol. 507, no. 2: IOP Publishing, p. 022004.

[3.8] J. Rhyner, "Magnetic properties and AC-losses of superconductors with power law current—voltage characteristics," *Physica C: Superconductivity,* vol. 212, nos. 3-4, pp. 292-300, 1993.

[3.9] S. Farinon, G. Iannone, P. Fabbricatore, and U. Gambardella, "2D and 3D numerical modeling of experimental magnetisation cycles in disks and spheres," *Superconductor Science and Technology,* vol. 27, no. 10, p. 104005, 2014.

[3.10] Z. Zhong, "A study of Critical Currents and Quench in 2G Superconductors under varying magnetic fields," PhD Thesis, University of Cambridge, 2015.

[3.11] Z. Hong, A. M. Campbell, and T. A. Coombs, "Numerical solution of critical state in superconductivity by finite element software," *Superconductor Science and Technology,* vol. 19, no. 12, pp. 1246-1252, 2006/10/23 2006, doi: 10.1088/0953-2048/19/12/004.
[3.12] T. Coombs, Z. Hong, Y. Yan, and C. Rawlings, "The next generation of superconducting permanent magnets: The flux pumping method," *IEEE Transactions on Applied Superconductivity,* vol. 19, no. 3, pp. 2169-2173, 2009.
[3.13] M. Zhang and T. Coombs, "3D modeling of high-Tc superconductors by finite element software," *Superconductor Science and Technology,* vol. 25, no. 1, p. 015009, 2011.

CHAPTER 4 Numerical Investigation of AC Loss in HTS Bulks Subjected to Rotating Magnetic Field

4.1 Introduction

Over the past three decades, high-temperature superconductors have shown promising capabilities and possibilities for high-performance large-scale electrical machines [4.1]. HTS bulks fabricated from RE-Ba-Cu-O (RE stands for rare-earth element) by top-seeded melt growth technique have the ability to trap much higher magnetic fields at low temperatures than the traditional permanent magnets. The magnetic flux density trapped in HTS permanent magnets can be significantly increased with the sample size and value of critical current density. Currently, HTS magnets hold the world record of 17.9 T of the trapped magnetic field [4.2]. This distinctive property makes these trapped field magnets suitable candidates for designing compact, light-weight, and energy-efficient electrical machines having outstanding high-power densities [4.3, 4.4] ranging from high-performance electrical motors [4.5] to HTS magnetic levitation [4.6]. Besides the applications in electrical machines, there have been significant advancements in superconducting electronics such as antennae, resonators, as well as active elements like Josephson junctions and superconducting quantum interference devices (SQUIDS) [4.7]. Moreover, with further developments in flexible electronics [4.8, 4.9], the applications of HTS materials have been extended to future flexible electronics for superconductor-based devices [4.10, 4.11]. Furthermore, a recent study has also reported a possible application of superconducting material in high-efficiency magnetic refrigerators [4.12].

However, there is a significant challenge to preserving cryogenic temperature to maintain its superconducting state, which is often achieved using liquid nitrogen (LN2) in type-II superconductors. The commercialisation of HTS is also handicapped due to dissipative interactions that occur during the exposure of the superconductor to an alternating magnetic field. This phenomenon is referred to as superconducting alternating current (AC) loss, which is produced due to the movement of vortices inside the superconducting material, and such heat can create an additional burden on the cryogenic cooling system. This power dissipation is variable with different factors such as the geometry of the material, the direction of the applied magnetic field, and current density distribution inside the material. Therefore, it is essential to investigate the electromagnetic properties of HTS bulks to safeguard the feasibility of these materials.

HTS permanent magnets, when used in rotating machines, can be exposed to alternating as well as rotating magnetic fields. However, most of the electromagnetic investigations in the literature cover the characterisation of HTS bulks subjected to the one-dimensional alternating magnetic field. Various experimental methods reported in the literature, mainly on AC loss, also focus only on one-dimensional exposure due to the unavailability of the robust HTS rotating magnetic property testing system. There are only a few studies reported in the literature, which shed some light on magnetic movement [4.13, 4.14] and levitational force [4.15], but a comprehensive investigation of the AC loss, current density distribution in three-dimensional axes, and trapped field analysis under the rotating magnetic fields are still required. Therefore, the detailed electromagnetic characterisation of HTS bulks under rotating magnetic fields remains unclear and must be investigated in order to fully understand electromagnetic properties for the efficient design of HTS rotating machines.

This investigation presents a three-dimensional (3D) numerical investigation based on finite element analysis (FEA) for the characterisation of HTS bulks subjected to rotating magnetic fields, mainly focusing on current density distribution, AC loss, and trapped field analysis when the HTS sample is exposed to various rotating magnetic flux density patterns in the XOY, YOZ, and ZOX planes.

4.2 Numerical Model Framework

Numerical modelling tools are essential for the development and commercialisation of HTS applications. These models provide the opportunity to predict and reveal all the features and material properties of superconducting materials without rigorous experiments needs, which takes a lot of time and financial resources. In this study, we have adopted 3D H-formulation, which has proved to be one of the most reliable numerical models based on finite element analysis. 3D models have an advantage over two-dimensional (2D) models in terms of higher degrees of freedom to the cross-sectional planes in a complete 3D mesh. The model has been developed using commercial FEA-based software COMSOL Multiphysics with a cubic geometry assuming the sample is cooled to its critical temperature.

4.2.1 H Formulation Model

There are various finite element based numerical models, which can be used to simulate the electromagnetic behaviour of HTS, such as the A-V formulation [4.16] based on magnetic vector potential, the T-Ø formulation [4.17] based on current vector potential and the most commonly used magnetic field-based H-formulation [4.18] which uses the magnetic field

strength as the dependent variable and nonlinear resistivity for considering specific electrical characteristics of superconductors. The H-formulation has been widely used by researchers around the world to model a variety of HTS topologies thanks to its accuracy, excellent convergence, reasonable computing time, and strong consistency with experimental results [4.19, 4.20]. In this study, we have used the well-studied FEA-based H-formulation. The mathematical structure of the H formulation has been described in Section 3.5.

For the conventional material, the resistivity is constant in, but in terms of superconductors, it depends on the current density. Normally, it assumes the form of power law, as follows:

$$\rho = \frac{E_0}{J}\left(\frac{J}{J_c}\right)^{n-1} \tag{4.1}$$

where E_0 is the characteristic electric field strength, J_c is the critical current density, and n represents the steepness of the shift from superconducting to normal state, usually called power factor. As n reaches infinity, the power law approaches the critical state model [4.21], which is commonly known as Bean's critical state model.

The application of an external magnetic field can be set up around the boundary of the sample at the air domain using Dirichlet boundary conditions. Moreover, when J has a parallel component to B, the critical current density is affected by the direction of the current density relative to the magnetic field, resulting in force-free effects. As a result, high-accuracy models with $J_c(B)$ and anisotropy dependency are essential. In order to consider such an isotropic behaviour, Kim's model is also incorporated to account for $J_c(B)$ dependence, as follows (4.2):

$$J_c(B) = \frac{J_{c0}}{\left(1 + \frac{|B|}{B_0}\right)^m} \tag{4.2}$$

In order to compute the AC loss, power dissipation $E \cdot J$ is integrated over the domain of interest, as follows:

$$Q = \frac{2}{T}\int_{0.5T}^{T}\int_{\Omega} E \cdot J \, d\Omega dt \tag{4.3}$$

where Ω represents the domain for calculating AC loss and T is the period of AC signal. The other relevant parameters used in the model are listed in Table 4.1.

Table 4.1: Model Parameters

Parameter	Symbol	Value
Permeability of free space	μ_0	$4\pi \times 10^{-7}$ Hm^{-1}
Power Factor	n	25
Critical Current Density	J_{c0}	108 A.mm^{-2}
Characteristic Electric Field	E_0	10^{-4} Vm^{-1}
Kim's Model Arbitrary Parameter	B_0	0.0041 T
Kim's Model Arbitrary Parameter	m	0.5

4.2.2 Rotating Magnetic Fields

The magnetic flux density vector B is typically restricted from flowing in the same direction as the magnetic field intensity H in 1D magnetic fields. In rotating electrical devices, however, the magnetic field rotates on a 2D plane, with B and H vectors that may or may not be in the same direction. The magnetic field is applied to the superconducting domain's boundaries in this scenario. In the case of a 1D alternating field, a sine wave of the desired amplitude is introduced. The applied rotating magnetic field in the case of 2D rotating magnetisation, on the other hand, is just a combination of sine waveforms at the boundaries of two separate axes, as per the testing criteria which may be expressed using the following equations:

$$B_{1D(alt)} = B_0 \sin(\omega t) \tag{4.4}$$

$$B_{2D(rot)} = \begin{cases} B_0 \sin(\omega t) \\ B_0 \sin(\omega t \pm \emptyset)\,(1 - \exp\left(-\frac{t}{\tau}\right)) \end{cases} \tag{4.5}$$

where B_0 is the amplitude of the magnetic flux density, ω is the angular frequency, $\emptyset$ represents the phase shift angle, and τ is the time constant which is set as 0.05 s. A purely circular rotating field is created, which is usually obtained by shifting the phase angle of the second source by 90 degrees (i.e., π/2).

It should be noted that when a phase angle is moved along the axis, the magnetic field's starting value is not equal to zero, causing an issue with the initial values in FEA and preventing the model from converging. As a result, in order to produce a transitory start, an exponential step function is applied in the second field source in Equation (4.10). In order to explore the electromagnetic properties of HTS bulks subjected to rotating magnetic fields, various 2D rotating flux density vectors in the XOY, YOZ, and ZOX planes are used in this study. At 200 mT, a purely circular rotating magnetic field surrounding the sample can be seen in Figure 4.1, which depicts the *B* Loci of various flux density patterns utilised in this investigation.

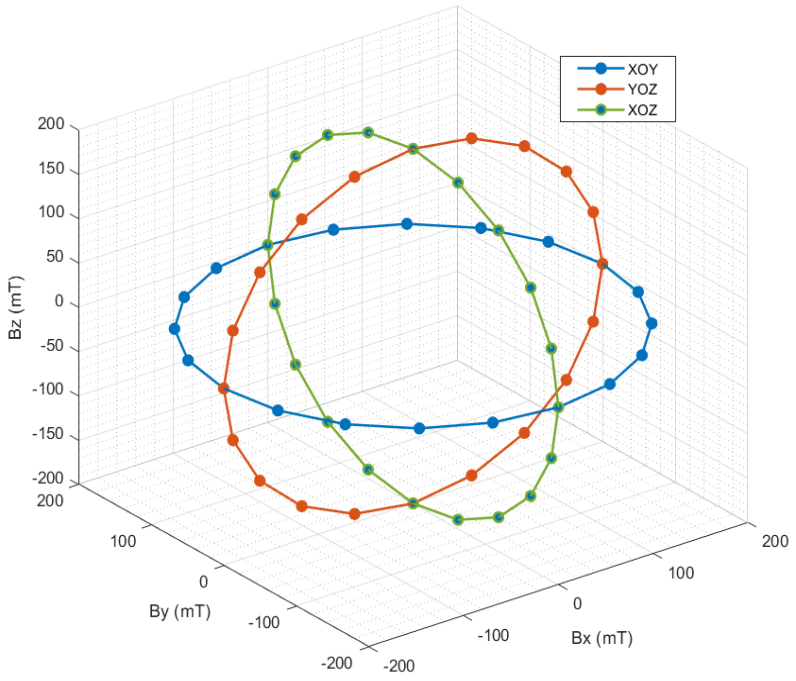

Figure 4.1: Loci of flux density for flux density vectors XOY, XOZ, and YOZ.

4.2.3 Model Validation

The same geometry was employed to perform this investigation in continuation with the benchmark study since the benchmark model of the cubic HTS sample is available for magnetisation of the cubic sample on the z-axis. In order to validate the model, a sinusoidal magnetic field with an amplitude of 100 mT, and frequency of 50 Hz is applied on the z-axis of the sample. The critical current density of the bulk superconductor is set as $J_{c0} = 108$ A/mm^2. The current density ratio J_z/J_{c0} along the x-axis at y = 2.07 mm and z = 1.1 mm is presented in Figure 4.2. As it can be observed, the simulation results are in good agreement with the

benchmark solution [4.22]. Hence, the 3D modelling approach used in this article is considered to be accurate.

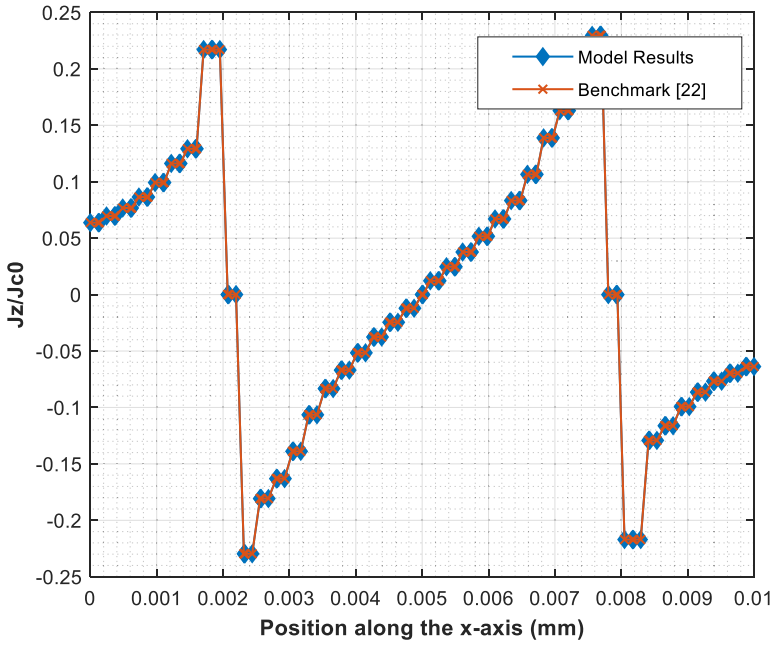

Figure 4.2: J_z/J_{c0} along the x-axis at y = 2.07 mm and z = 1.1 mm for the benchmark cubic bulk superconductor model and the model built in this study. The benchmark solution is obtained using MEMEP and the relevant data are extracted from benchmark.

4.3 Characterisation of Magnetic Properties of HTS Bulk Cubic Sample

This study presents a numerical investigation on the characterisation of HTS bulks subjected to rotating magnetic fields showing the AC loss and current density distribution in three-dimensional space. A 3D numerical model has been developed using H-formulation based on finite element analysis. The HTS cubic sample is magnetised with two-dimensional magnetic flux density vectors rotating in clockwise and anti-clockwise directions in the XOY, XOZ, and YOZ planes, respectively. The results are compared with the Benchmark of cubic bulk magnetisation with alternating fields. The geometry of the sample is shown in Figure 4.3.

HTS trapped field magnets are alternative to permanent magnets, but their investigation under rotating magnetic fields is not explicitly mentioned in the literature. Therefore, a thorough investigation of the movement of screening currents is indeed necessary. This study considers all finite-size effects with many layers of cells in the thickness. Since the 3D model

technique allows current to flow in all three dimensions (x, y, and z), consequently, there is J for all three components (J_x; J_y; J_z).

In this section electromagnetic response of the HTS bulk subjected to rotating magnetic fields in XOY, XOZ, and YOZ with the amplitude of 200mT is calculated using the model parameters mentioned in Section 4.2.1.

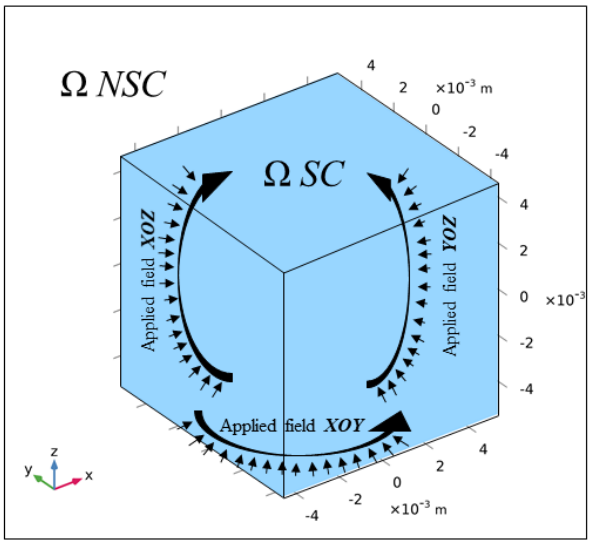

Figure 4.3: Geometry of the HTS bulk sample. Ω SC is the superconducting region, and Ω NSC is the non-superconducting air domain. The magnetic fields are applied in XOY, XOZ, and YOZ planes, respectively.

4.3.1 One Dimensional (1D) Magnetisation in Z-axis

Figures 4.4-4.6 show the real 3D current density distribution patterns when an alternating magnetic field of 20 mT is applied in z- axis. J_x and J_y components start to penetrate from the sides and continue all the way till y/d=20mm and x/d=20mm respectively and become equal to the J_c. J_z component on the other hand penetrates in the diagonal pattern starting from the edges of the sample, and vanishes up to z/d=0mm having value of 0.6 J_c.

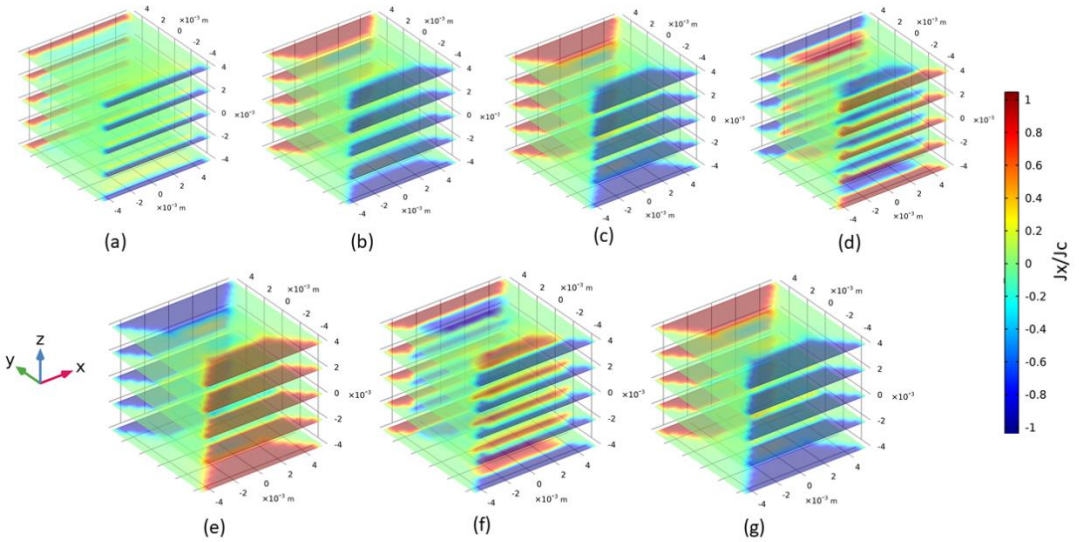

Figure 4.4: Component of current density J_x subjected to 200 mT 1D magnetic fields in z-axis at 1 ms (a), 3 ms (b), 5 ms (c), 10 ms (d), 15 ms (e), 20 ms (f), and 25 ms (g).

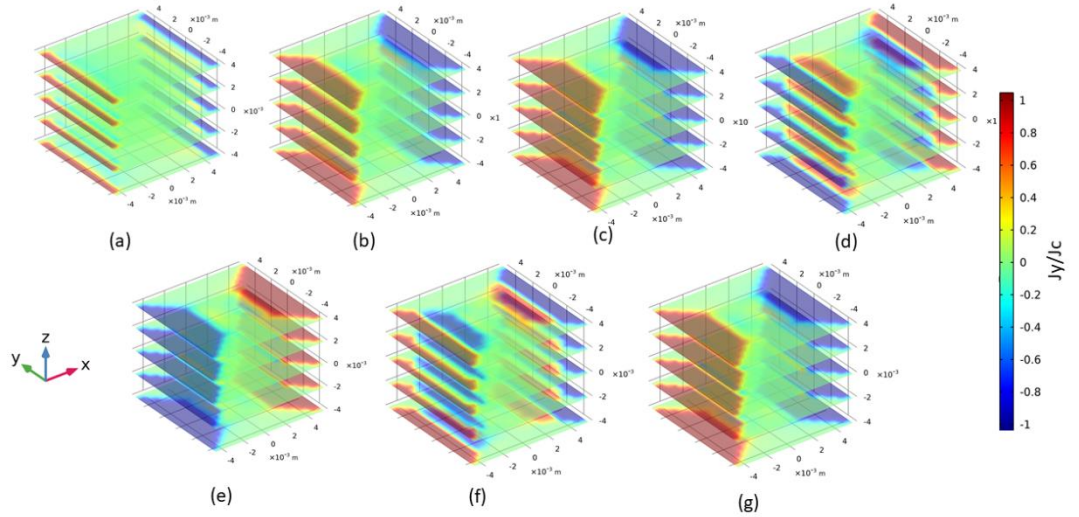

Figure 4.5: Component of current density J_y subjected to 200 mT 1D magnetic fields in z-axis at 1 ms (a), 3 ms (b), 5 ms (c), 10 ms (d), 15 ms, (e) 20 ms (f), and 25 ms (g).

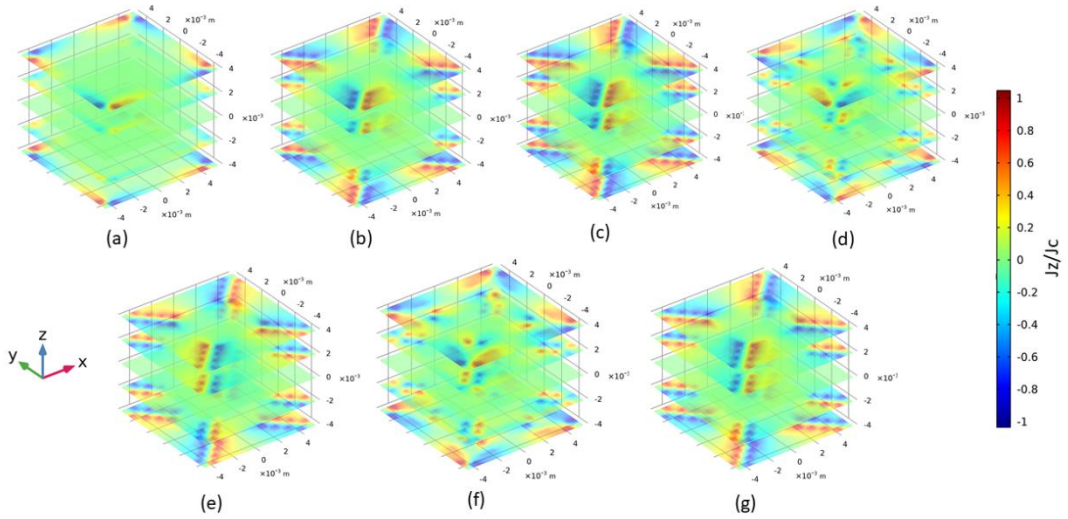

Figure 4.6: Component of current density J_z subjected to 200 mT 1D magnetic fields in z-axis at 1 ms (a), 3 ms (b), 5 ms (c), 10 ms (d), 15 ms (e), 20 ms (f), and 25 ms (g).

4.3.2 Two-Dimensional (2D) Magnetisation in XOY Plane

Figures 4.7-4.9 show the 3D current density patterns when a circularly rotating magnetic field of 20mT is rotated in the XOY plane. The J_x component starts to penetrate from the z-axis of the sample and goes up to z=20mm at 15ms, with screening currents circulating in the radius of 20mm. However, it settles at z=40mm with a value almost equal to 0.5 J_{c0}. J_y mostly remains on the surface around the z-axis, and a small current is penetrated up to 20mm at the z-axis. Moreover, J_y is zero at z=0mm throughout the magnetising process. The real rotating effect can be seen in the case of J_z where it starts from the surface of the Y-axis and rotates all the way to z=0mm. The current density, in this case, has completely penetrated in the sample, where the radius is decreased to zero along the magnetising process.

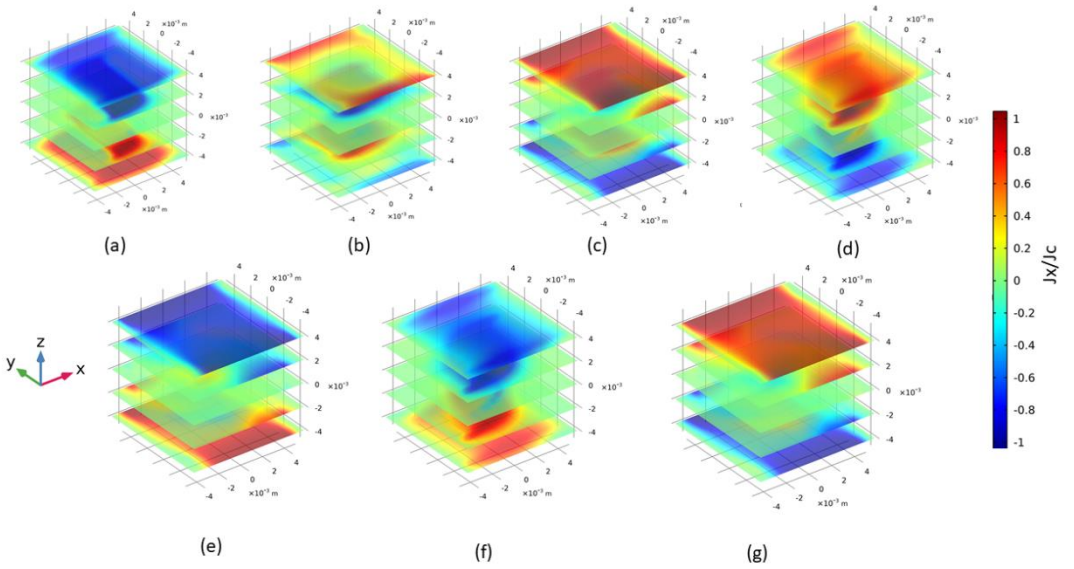

Figure 4.7: Component of current density J_x subjected to 200 mT 2D circular B in XOY plane at 1 ms (a), 3 ms (b), 5 ms (c), 10 ms (d), 15 ms (e), 20 ms (f), and 25 ms (g)

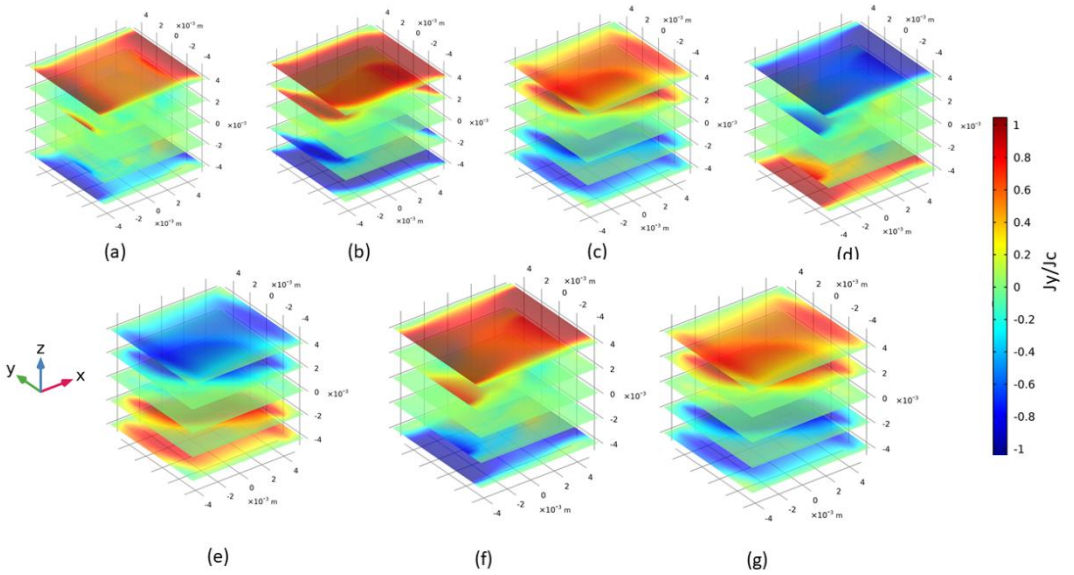

Figure 4.8: Component of current density J_y subjected to 200 mT 2D circular B in XOY plane at 1 ms (a), 3 ms (b), 5 ms (c), 10 ms (d), 15 ms (e), 20 ms (f), and 25 ms (g)

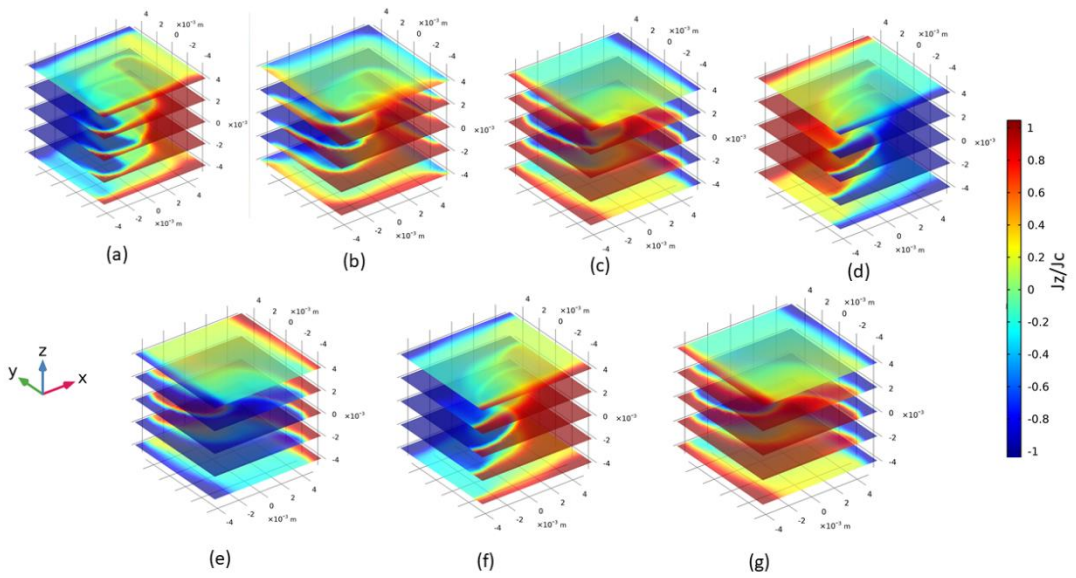

Figure 4.9: Component of current density J_z subjected to 200 mT 2D circular B in XOY plane at 1 ms (a), 3 ms (b), 5 ms (c), 10 ms (d), 15 ms (e), 20 ms (f), and 25 ms (g).

4.3.3 Two-Dimensional (2D) Magnetisation in XOZ Plane

Figures 4.10-4.12 shows the 3D current density patterns when a circularly rotating magnetic field of 20mT is rotated in the XOZ plane. The J_x component shows a similar distribution pattern as J_x in XOY plane. Here, however, it starts to penetrate from the y-axis of the sample and goes up to y=20mm at 15ms. It settles at y=40mm with a value almost equal to $0.5J_c$. Here J_y mainly rotates around the X-Z plane, starting from the sides of the x-axis and settling on the sides of the z-axis. In this case, the screening currents are rotated in a circular orientation, but it does not completely penetrate in-side the middle of the sample, unlike J_z in XOY. J_z stays mostly at the surface of the y-axis and penetrates only up to y=20mm.

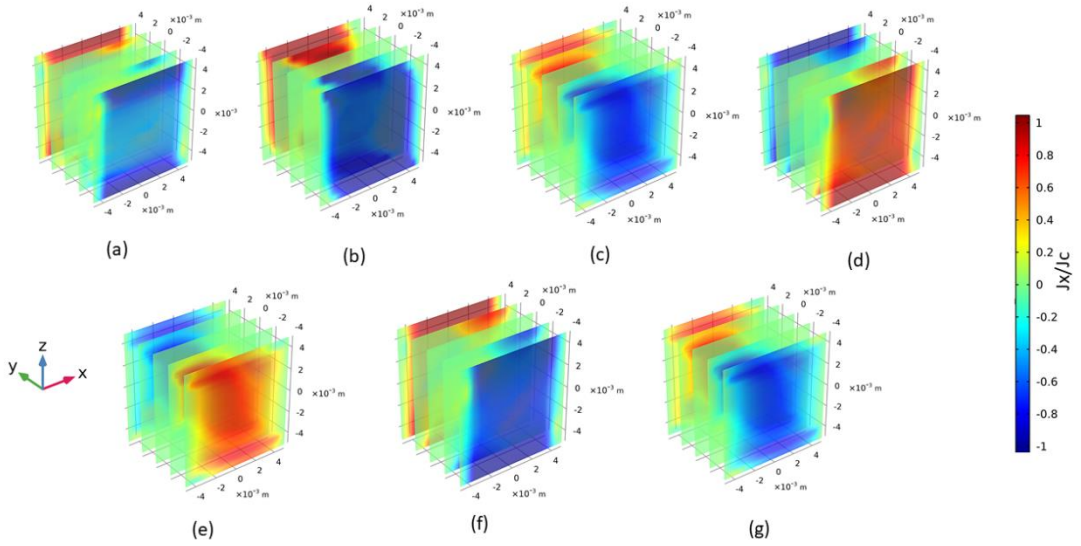

Figure 4.10: Component of current density J_x subjected to 200 mT 2D circular B in XOZ plane at 1 ms (a), 3 ms (b), 5 ms (c), 10 ms (d), 15 ms (e), 20 ms (f), and 25 ms (g).

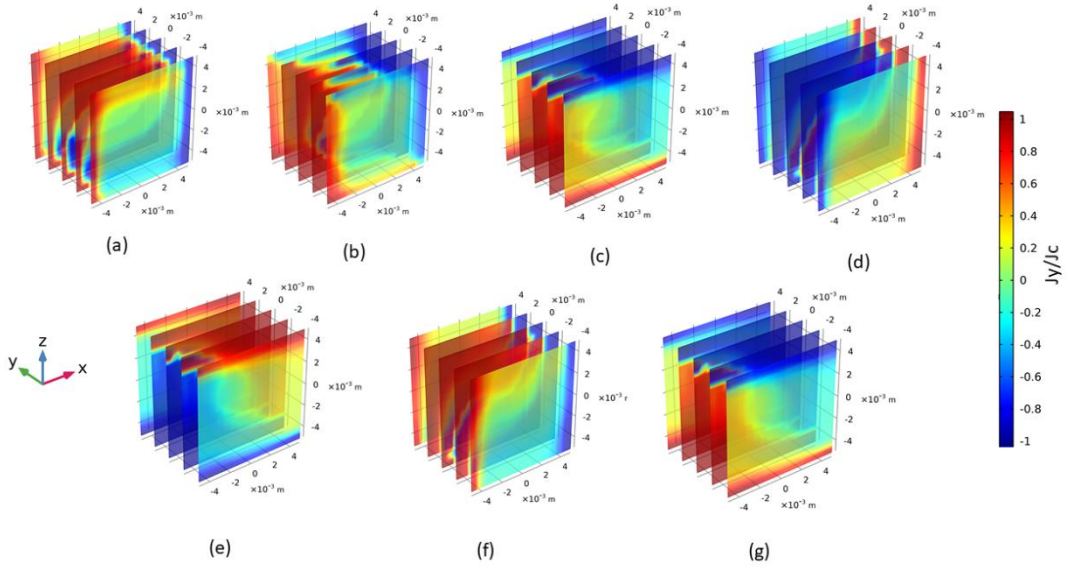

Figure 4.11: Component of current density J_y subjected to 200 mT 2D circular B in XOZ plane at 1 ms (a), 3 ms (b), 5 ms (c), 10 ms (d), 15 ms (e), 20 ms (f), and 25 ms (g).

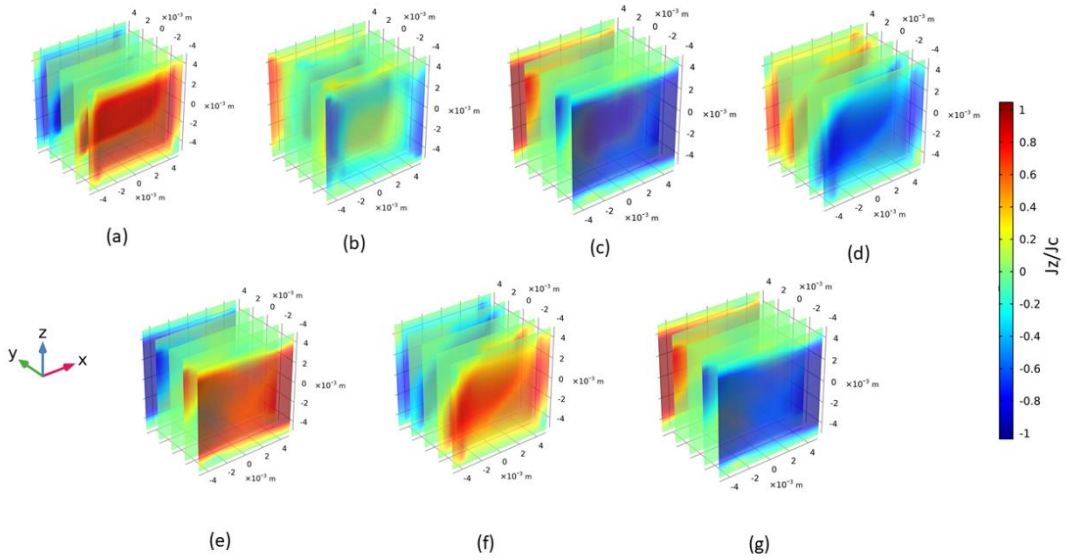

Figure 4.12: Component of current density J_z subjected to 200 mT 2D circular B in XOZ plane at 1 ms (a), 3 ms (b), 5 ms (c), 10 ms (d), 15 ms (e), 20 ms (f), and 25 ms (g).

4.3.4 Two-Dimensional (2D) Magnetisation in YOZ Plane

Figures 4.13-4.15 show the 3D current density patterns when a circularly rotating magnetic field of 20mT is rotated in the YOZ plane. Here J_x mainly rotates around the Y-Z plane, starting from the sides of the z-axis and settling on the sides of the y-axis, the screening currents are rotated in circular orientation, but these screening currents do not completely penetrate inside the middle of the sample, unlike J_z in the XOY plane. The J_y component mostly remains on the sides of the x-axis. However, the J_z component starts to penetrate from the x-axis of the sample, goes up to z=20mm, and ultimately settles at z=40mm with a value almost equal to J_c. J_z mostly remains on the surface around the z-axis and shows exactly the same penetrating behaviour as J_x in XOY.

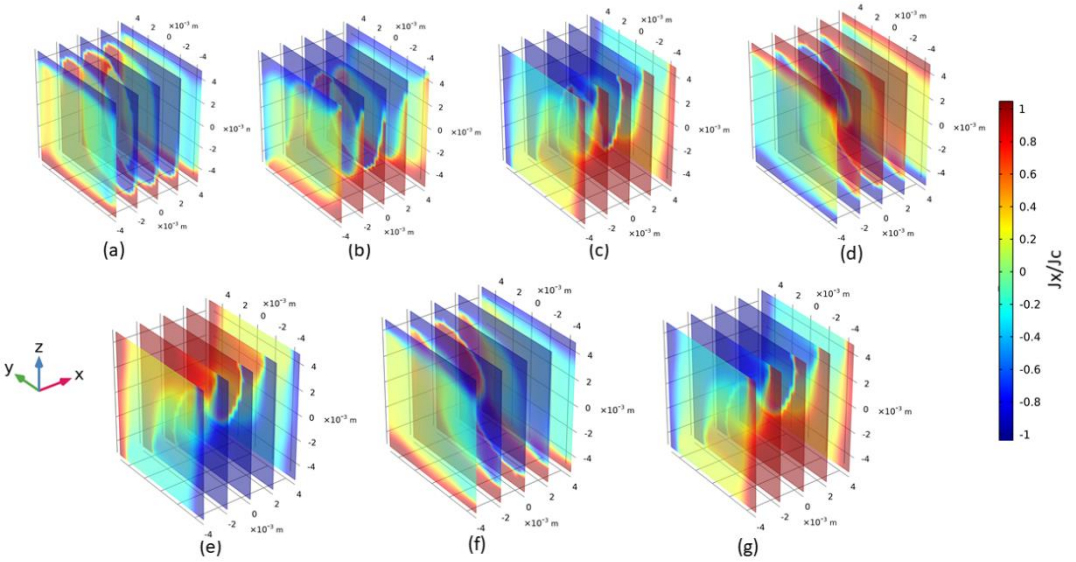

Figure 4.13: Component of current density J_x subjected to 200 mT 2D circular B in YOZ plane at 1 ms (a), 3 ms (b), 5 ms (c), 10 ms (d), 15 ms (e), 20 ms (f), and 25 ms (g).

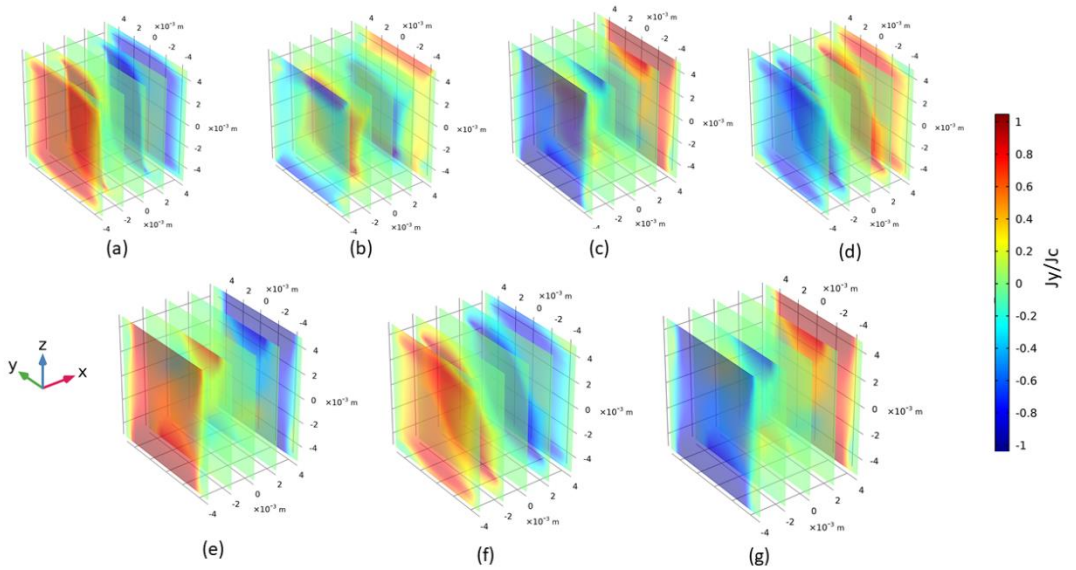

Figure 4.14: Component of current density J_y subjected to 200 mT 2D circular B in YOZ plane at 1 ms (a), 3 ms (b), 5 ms (c), 10 ms (d), 15 ms (e), 20 ms (f), and 25 ms (g).

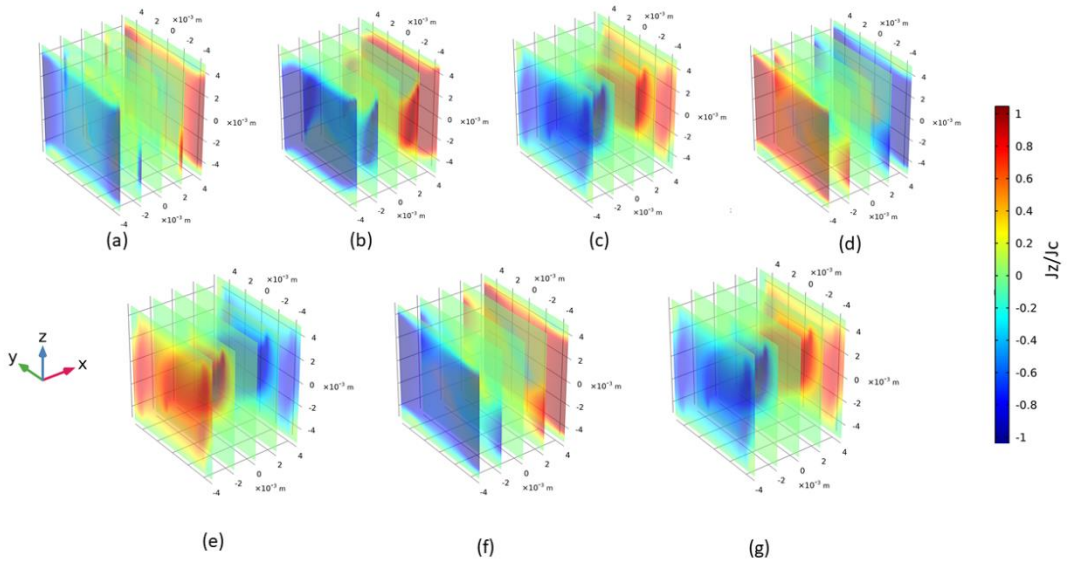

Figure 4.15: Component of current density J_z subjected to 200 mT 2D circular B in YOZ plane at 1 ms (a), 3 ms (b), 5 ms (c), 10 ms (d), 15 ms (e), 20 ms (f), and 25 ms (g).

4.3.5 AC Loss Distribution

Figures 4.16-4.19 show the AC loss distribution in the HTS bulk cubic sample when subjected to a rotating magnetic field of 20mT. In order to compare the results, the AC loss of 1D magnetisation in the z-axis is also given in Figure 4.16, followed by that in XOY, XOZ, and YOZ planes in Figure 4.17, Figure 4.18, and Figure 4.19, respectively at z=5mm. The AC loss in 1D magnetisation mainly appears in the sample's diagonals up to 3mm from each corner. The AC loss is circulated along the sides of the sample when the magnetic field is applied in XOY plane. However, the AC loss seems to be distributed in the middle of the sample as well in the cases of XOZ and YOZ. From the distribution patterns, it can be analysed that the AC loss is increased significantly when the HTS bulk sample is subjected to rotating magnetic fields in comparison with the one-dimensional alternating magnetic field. It should be noted that the loss distribution is captured at the same geometrical orientation to understand the pattern of distribution upon magnetizing in different axes.

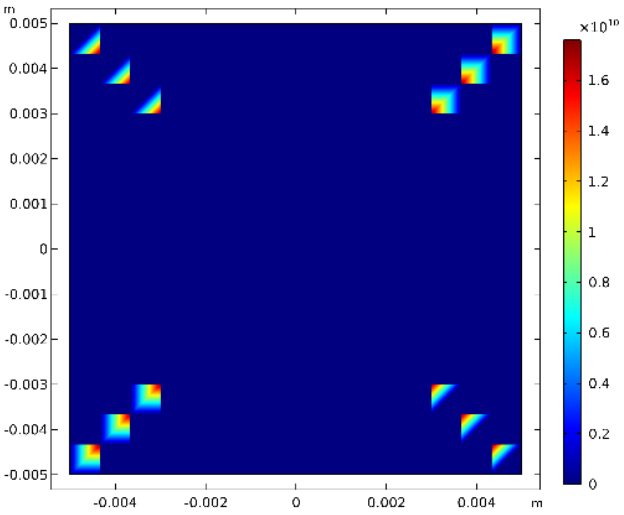

Figure 4.16: AC loss (W/m) distribution in 1-D Z-axis.

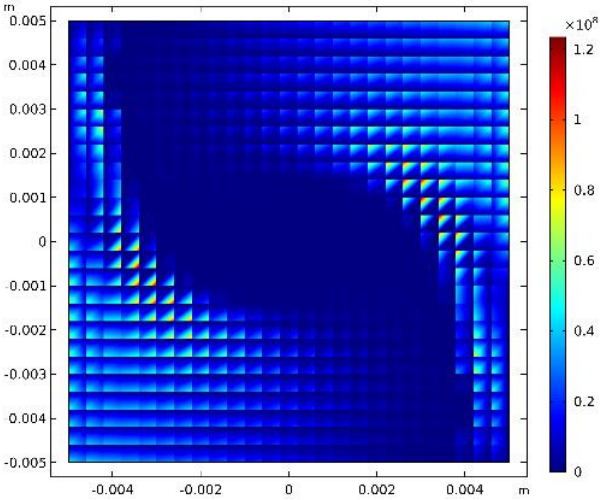

Figure 4.17: AC loss (W/m) distribution in XOY plane,

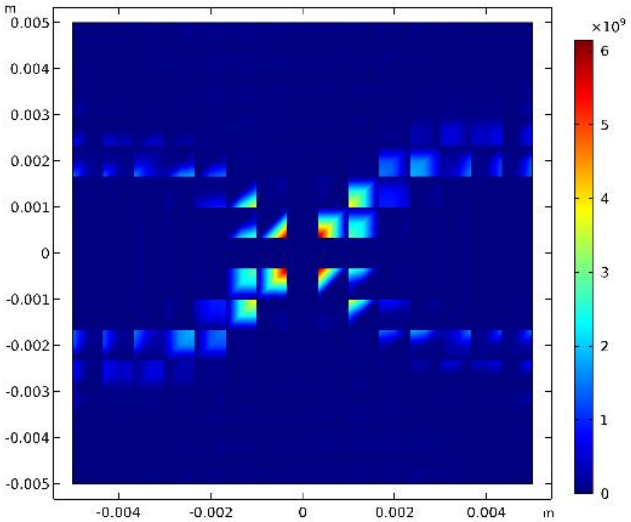

Figure 4.18: AC loss (W/m) distribution in XOZ plane.

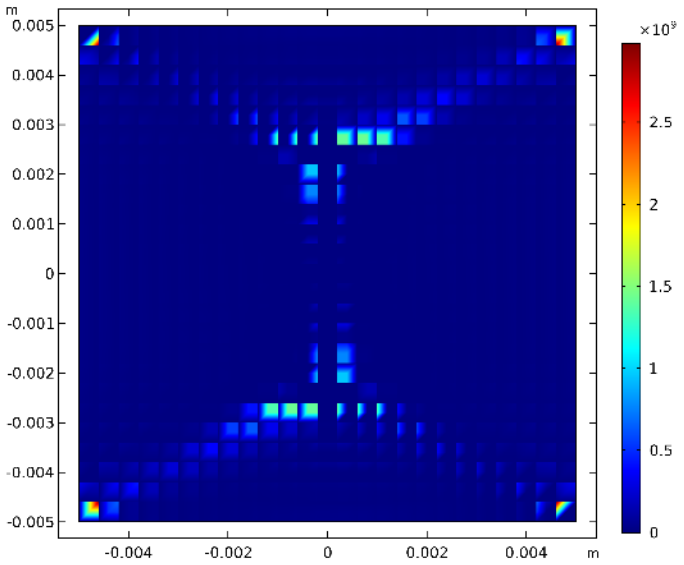

Figure 4.19: AC loss (W/m) distribution in YOZ plane.

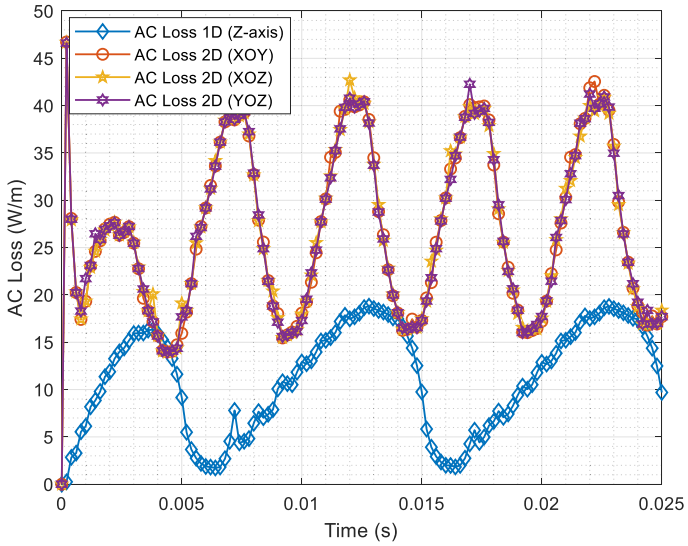

Figure 4.20: Instantaneous AC loss distribution at 200mT applied in z- axis, XOY plane, XOZ plane and YOZ plane.

4.3.6 Demagnetisation of HTS Bulk Under Rotating Magnetic Fields

HTS trapped field magnets have shown promising applications to be used as a substitute for permanent magnets in various large-scale applications. However, the application of external magnetic fields on HTS permanent magnets significantly decreases the trapped field. There are a lot of demagnetisation studies published on demagnetisation through transverse or cross-field demagnetisation, but demagnetisation through rotating magnetic fields is not reported anywhere. In this section, we have investigated the demagnetisation behaviour of HTS magnets under applied rotating magnetic fields in various orientations. The 3D model can produce

accurate results by considering a finite sample size, including end effects. The demagnetisation investigation has two parts. The first part is very important, where the sample will be magnetized to trap the magnetic field in order to become a trapped field magnet. In the second part, the trapped field magnet is demagnetized by rotating magnetic fields in different orientations.

For the first part of the study, the cubic sample is magnetized by Field Cooling Method, considering the sample is already cooled to its critical temperature [4.23]. The initial applied magnetic flux density is 1T with a ramp down rate of 10mT/s. Afterward, a relaxation time is initiated to stabilize the trapped magnetic field. Figure 4.21 shows the magnetic field trapped in the HTS bulk sample after the relaxation time. The trapped magnetic field of the sample is 0.27 T, which is computed at the centre of the top surface, similar to the Hall probe measurement. Parameters specific for demagnetisation are mentioned in Table II. The rest of the modelling parameters remain the same as per Table 4.2.

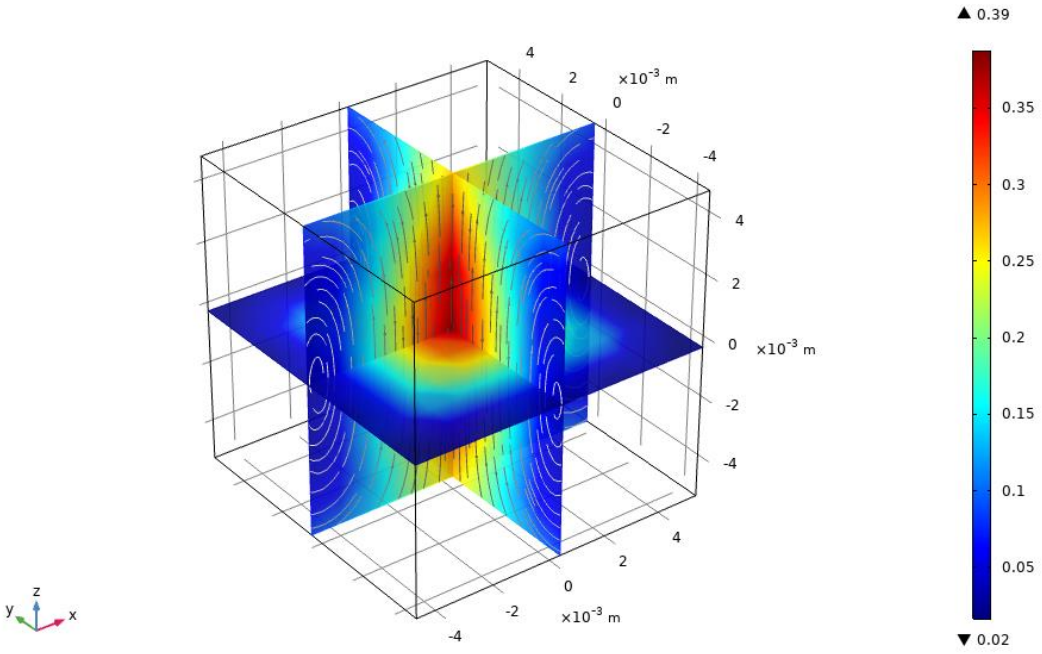

Figure 4.21: Trapped field (T) in HTS permanent magnet

Table 4.2 Model Parameters for Demagnetisation

Parameter	Value
Magnetising flux density	1 T
Ramp down rate of magnetising	0.01 T/s
Magnetising time	100 s
Time to allow for flux creep (Relaxation time)	100 s
Demagnetising time	5 s

Once the magnetic field is stabilised in the sample after relaxation time, the sample is exposed to various patterns of external magnetic fields of 0.1 T to observe the demagnetizing effect. In order to compare the demagnetisation through 1D magnetic fields, a transverse magnetic field is also applied in the y-direction. The effect of demagnetisation is presented in Figure 4.22.

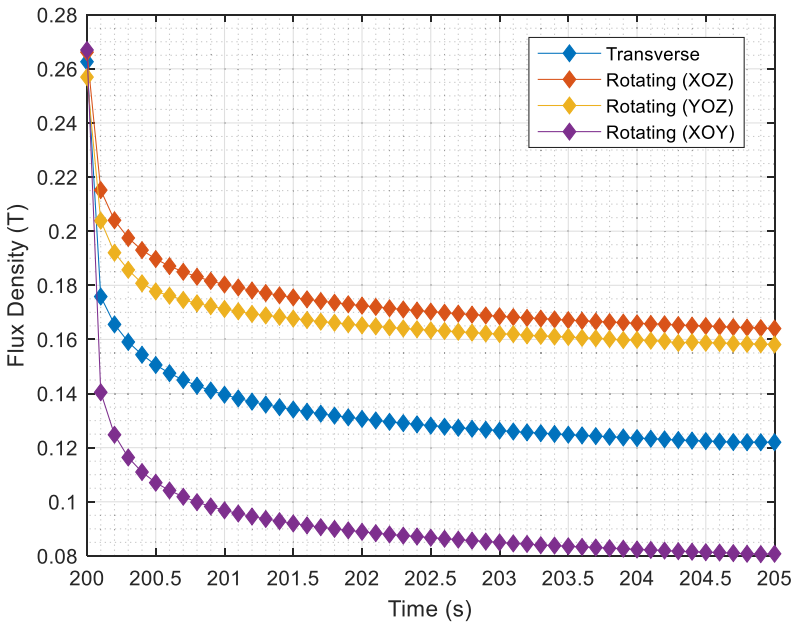

Figure 4.22: Demagnetisation in HTS trapped field subjected to rotating magnetic field

When the magnetic field is applied in the transverse direction, the sample is demagnetized to 0.12 T. The rotating magnetic fields in XOZ and YOZ orientations result in 0.17 T and 0.16 T, which are slightly higher than that in the transverse direction. It may be due to the fact that the sample is already magnetised in z-orientation, and the applied magnetic field can be parallel to the direction of the trapped field. However, when the field rotates on the

XOY plane, there is a significant decrease up to 0.8 T in the trapped field, mainly due to the application of a magnetic field perpendicular to the trapped magnetic field.

4.4 AC Loss Investigation Under Various Rotating Magnetic Flux Density Patterns

In this study, the magnetisation AC loss of a cubic HTS bulk sample of 40mm x 40mm x 5mm has been systematically modelled under various 1D alternating and 2D rotating flux density patterns up to 2 T. The geometry of the sample is shown in Figure 4.23. Since the rotating magnetic fields are mainly observed in rotating machines and HTS bulk can be a promising candidate for such applications, this investigation has been performed primarily at power frequency (50 Hz).

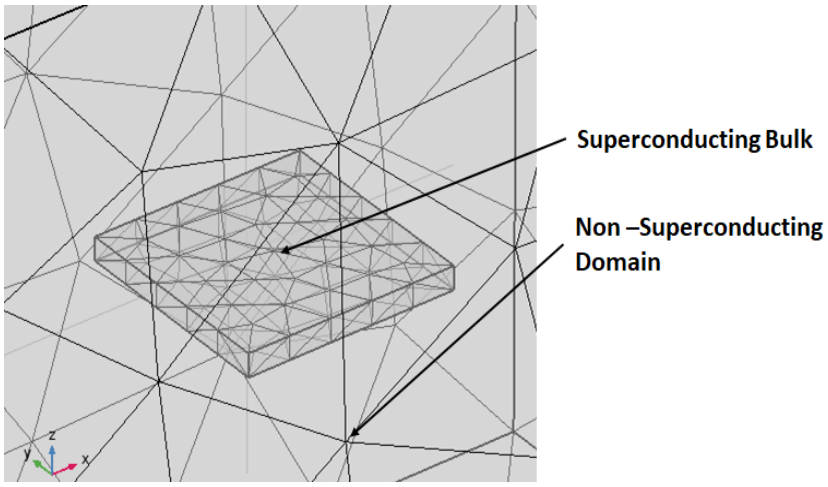

Figure 4.23: Geometry of the HTS bulk sample in the model.

Initially, the AC loss was obtained for alternating magnetic fields along the x-, y- or z-axis as shown in Figure 4.24. It can be seen that the AC loss in the z-direction is much higher than those in the x- and y- directions until 0.1 T, which is a common loss mechanism when HTS samples are subjected to perpendicular fields. However, the difference decreases significantly as the flux density increases up to 2 T. Furthermore, there is a slight difference between the AC losses in the x- and y-axes as well, where the AC loss in the x-axis is slightly higher than that in y-axis in the overall trend except at 0.25 T where the losses in the y-direction are slightly higher due to the anisotropy of HTS.

Figure 4.25 shows the AC loss under 2D rotating flux density vectors in the XOY, XOZ, and YOZ planes, respectively. It can be seen that the AC losses in XOZ and YOZ are higher than that in the XOY plane due to the involvement of the perpendicular field. However,

compared to the 1D AC loss in the z-axis, the 2D loss increases up to twice of the corresponding 1D loss until 0.1T, and then reduces significantly to negligible difference up to 2 T. Furthermore, the AC loss in XOY increases up to 4.2 times at 0.25 T compared to the AC losses at both x- and y-axes, however, the difference is significantly reduced until 2T, but still, there seems to be a 75% increase.

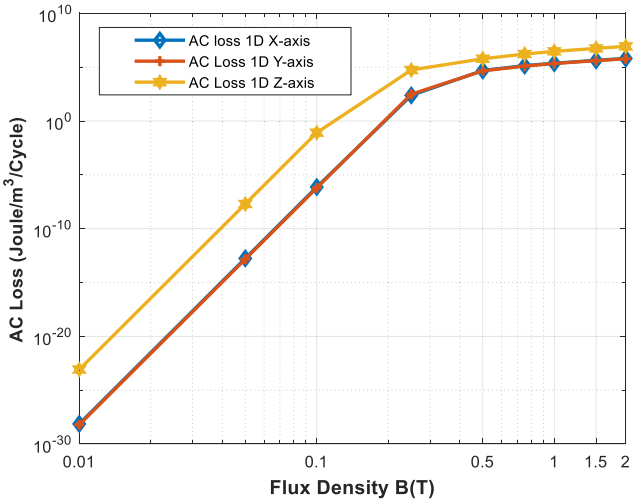

Figure 4.24: AC loss under 1D alternating fields.

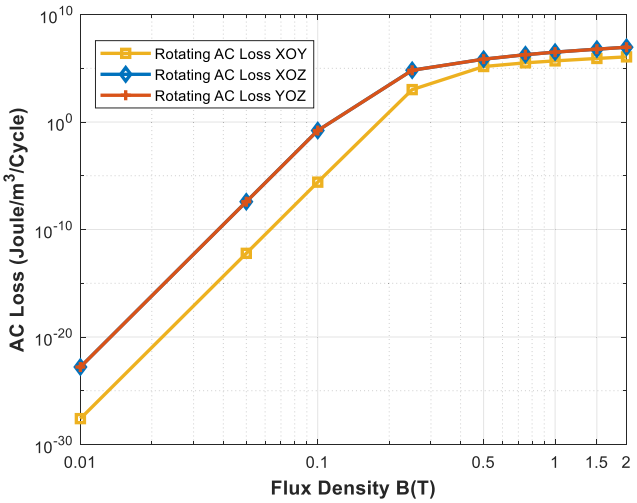

Figure 4.25: AC loss under various rotating magnetic flux density patterns.

In the above findings, the rotating losses in the XOY, XOZ, and YOZ planes are reported where the field rotates in the clockwise direction in a circular pattern. Figures 4.26-4.28 show a comparison of AC losses in these scenarios when the field rotates in the anti-clockwise direction. The rotating AC losses seem to be the same in both the clockwise and anti-clockwise directions for all three patterns up to 0.1 T, but there seems to be a slight

decrease in the loss when the field rotates in the anti-clockwise direction, which continues until 2 T. This slight reduction can be associated with the shifting of phase angle by -90 degrees (i.e. $\pi/2$) where the impact of the rotating field appears to be less at the start of each cycle.

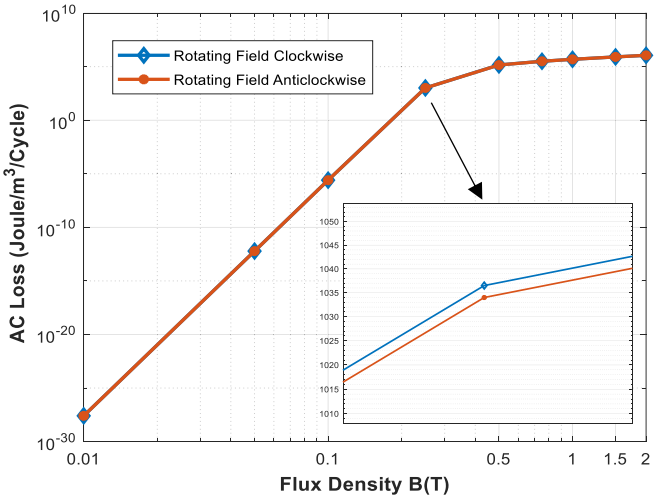

Figure 4.26: Comparison of AC losses with 2D rotating flux density in clockwise and anti-clockwise directions in the XOY plane.

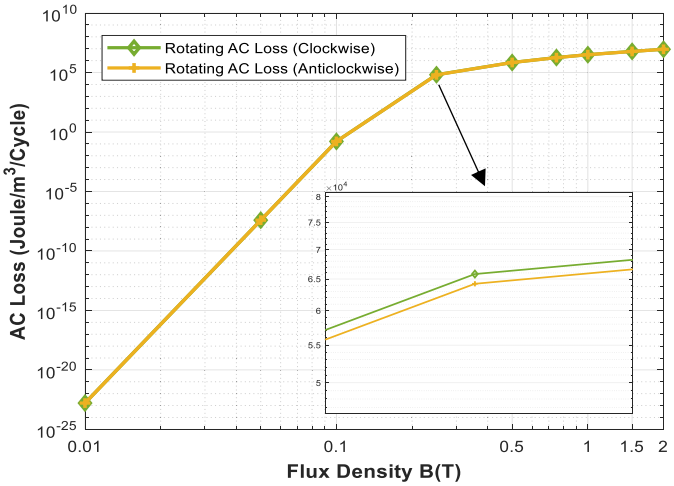

Figure 4.27: Comparison of AC losses with 2D rotating flux density in clockwise and anti-clockwise directions in the *XOZ*

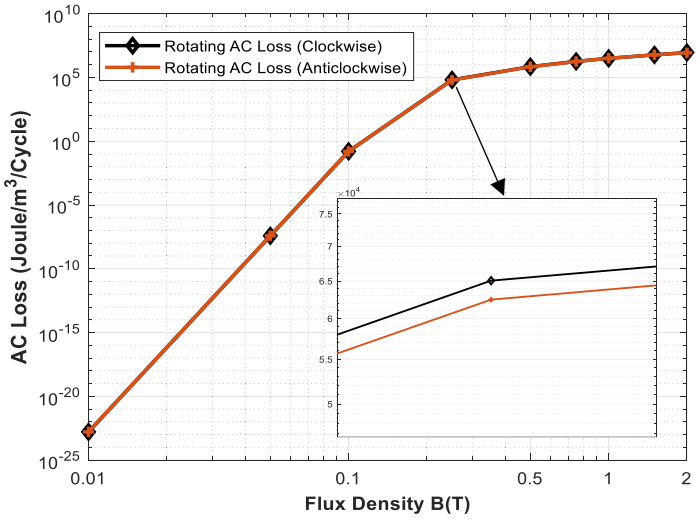

Figure 4.28: Comparison of AC losses with 2D rotating flux density in clockwise and anti-clockwise directions in the (a) *XOY* (b) *XOZ* and (c) *YOZ* planes.

4.5 Conclusions

In this investigation, we have analysed and characterised the electromagnetic properties of HTS bulk using 3D numerical modelling techniques under the exposure of rotating magnetic fields in XOY, XOZ, and YOZ planes. To explain all finite-size effects, complete 3D computation methods for nonlinear superconducting materials are required. Because the power devices are finite in size, the finite-size effects aid in understanding and optimizing superconductors in power applications. The interpretation of characterisation and measurement is also influenced by finite size effects. The 3D numerical model provides realistic predictions considering all finite-size effects with a huge number of degrees of freedom. The typical current density distribution J and AC loss distribution profiles are presented for all three components (J_x; J_y; J_z) under the influence of a rotating magnetic field in different orientations. The demagnetisation subjected to the similar rotating fields is also investigated to see how the HTS trapped field magnets are demonized, which is also a very important characteristic for the applications as an alternate candidate to permanent magnets. The performance of the model has been verified with the available benchmark of the HTS cubic bulk sample. The electromagnetic data presented in this study will provide a comprehensive understating of the material properties of HTS when subjected to rotating magnetic fields. The findings on the AC loss under various flux density patterns show that the losses are significant until 0.1T when the magnetic field rotates in the z-axis. However, the losses increase up to four times when the field rotates around the x- or y-axis. Furthermore, there appears to be a slight decrease in the

AC loss when the magnetic field rotates in the anti-clockwise direction, compared to the loss subject to the rotating field in the clockwise direction.

Although the numerical models are powerful tools to predict the performance of the HTS material, experimental techniques are also really important for the investigation of HTS electromagnetic properties. But still, there is a lack of robust experimental methods mainly to predict material properties under rotating magnetic fields, especially the AC loss. In upcoming chapters, such an experiment technique shall be proposed to predict the rotating AC loss mechanism in order to fully understand the material properties.

4.6 References

[4-1] W. A. Soomro, Y. Guo, H. Y. Lu, and J. X. Jin, "Advancements and impediments in applications of high-temperature superconducting material," in Proceedings *2020 IEEE International Conference on Applied Superconductivity and Electromagnetic Devices (ASEMD)*, 16-18 Oct. 2020 2020, pp. 1-4, doi: 10.1109/ASEMD49065.2020.9276278.

[4.2] M. Zhang, "A new world record for a superconducting trapped field magnet," *Superconductor Science and Technology,* vol. 32, no. 7, p. 070502, 2019/06/04 2019, doi: 10.1088/1361-6668/ab17e6.

[4.3] D. Zhou, M. Izumi, M. Miki, B. Felder, T. Ida, and M. Kitano, "An overview of rotating machine systems with high-temperature bulk superconductors," *Superconductor Science and Technology,* vol. 25, no. 10, p. 103001, 2012.

[4.4] R. Bause, M. D. Ainslie, M. Corduan, M. Boll, M. Filipenko, and M. Noe, "Electromagnetic design of a superconducting electric machine with bulk HTS material," *arXiv preprint arXiv:1903.08906,* 2019.

[4.5] H. Moon, Y. Kim, H. Park, M. Park, and I. Yu, "Development of a MW-class 2G HTS ship propulsion motor," *IEEE Transactions on Applied Superconductivity,* vol. 26, no. 4, pp. 1-5, 2016, doi: 10.1109/TASC.2016.2536660.

[4.6] W. Chen, Y. Xu, Z. Wang, L. Ren, J. Shi, and Y. Tang, "Levitation force computation of HTS/PM system based on H-formulation," *IEEE Transactions on Magnetics,* vol. 54, no. 11, pp. 1-5, 2018, doi: 10.1109/TMAG.2018.2847288.

[4.7] A. I. Braginski, "Superconductor electronics: status and outlook," *Journal of Superconductivity and Novel Magnetism,* vol. 32, no. 1, pp. 23-44, 2019, doi: 10.1007/s10948-018-4884-4.

[4.8] G. Zan *et al.*, "A biomimetic conductive super-foldable material," *Matter,* vol. 4, no. 10, pp. 3232-3247, 2021/10/06/ 2021, doi: https://doi.org/10.1016/j.matt.2021.07.021.

[4.9] G. Zan *et al.*, "Bioinspired nanocomposites with self-adaptive stress dispersion for super-foldable electrodes," *Advanced Science,* vol. 9, no. 3, p. 2103714, 2022, doi: https://doi.org/10.1002/advs.202103714.

[4.10] J. P. Smith *et al.*, "Flexible coaxial ribbon cable for high-density superconducting microwave device arrays," *IEEE Transactions on Applied Superconductivity,* vol. 31, no. 1, pp. 1-5, 2021, doi: 10.1109/TASC.2020.3008591.

[4.11] J. Huang, H. Wang, H. Wang, B. Zhang, X. Qian, and H. Wang, "Superconducting iron chalcogenide thin films integrated on flexible mica substrates," *IEEE Transactions on Applied Superconductivity,* vol. 29, no. 5, pp. 1-4, 2019, doi: 10.1109/TASC.2019.2906771.

[4.12] R. Gimaev, Y. Spichkin, B. Kovalev, K. Kamilov, V. Zverev, and A. Tishin, "Review on magnetic refrigeration devices based on HTSC materials," *International Journal of Refrigeration,* vol. 100, pp. 1-12, 2019/04/01/ 2019, doi: https://doi.org/10.1016/j.ijrefrig.2019.01.024.

[4.13] P. Vanderbemden *et al.*, "Remagnetisation of bulk high-temperature superconductors subjected to crossed and rotating magnetic fields," *Superconductor Science and Technology,* vol. 20, no. 9, p. S174, 2007.

[4.14] M. Qiu, L. Z. Lin, G. M. Zhang, Y. S. Wang, and L. Y. Xiao, "Flux dynamic behavior inside HTS bulks under rotating magnetic field," *IEEE Transactions on Applied Superconductivity,* vol. 12, no. 1, pp. 1163-1166, 2002, doi: 10.1109/TASC.2002.1018608.

[4.15] M. Qiu, H. K. Huo, Z. Xu, D. Xia, and L. Z. Lin, "Electromagnetic phenomena in HTS bulk subjected to a rotating field," *IEEE Transactions on Applied Superconductivity,* vol. 14, no. 2, pp. 1898-1901, 2004, doi: 10.1109/TASC.2004.830923.

[4.16] G. P. Lousberg, M. Ausloos, C. Geuzaine, P. Dular, P. Vanderbemden, and B. Vanderheyden, "Numerical simulation of the magnetisation of high-temperature superconductors: a 3D finite element method using a single time-step iteration," *Superconductor Science and Technology,* vol. 22, no. 5, p. 055005, 2009, doi: 10.1088/0953-2048/22/5/055005.

[4.17] N. Amemiya, S.-i. Murasawa, N. Banno, and K. Miyamoto, "Numerical modelings of superconducting wires for AC loss calculations," *Physica C: Superconductivity,* vol. 310, no. 1, pp. 16-29, 1998/12/01/ 1998, doi: https://doi.org/10.1016/S0921-4534(98)00427-4.

[4.18] G. Escamez *et al.*, "3-D numerical modeling of AC losses in multifilamentary MgB2 Wires," *IEEE Transactions on Applied Superconductivity,* vol. 26, no. 3, pp. 1-7, 2016, doi: 10.1109/TASC.2016.2533024.

[4.19] B. Shen, F. Grilli, and T. Coombs, "Overview of H-formulation: A versatile tool for modeling electromagnetics in high-temperature superconductor applications," *IEEE Access,* vol. 8, pp. 100403-100414, 2020.

[4.20] B. Shen, F. Grilli, and T. Coombs, "Review of the AC loss computation for HTS using H formulation," *Superconductor Science and Technology,* vol. 33, no. 3, p. 033002, 2020.

[4.21] C. P. Bean, "Magnetisation of hard superconductors," *Physical Review Letters,* vol. 8, no. 6, p. 250, 1962.

[4.22] H. M. WORKGROUP. http://www.htsmodelling.com/?wpdmpro=b5_results-3. (accessed on February 13th 2023).

[4.23] S. Zou, V. M. R. Zermeño, and F. Grilli, "Simulation of stacks of high-temperature superconducting coated conductors magnetized by pulsed field magnetisation using controlled magnetic density distribution coils," *IEEE Transactions on Applied Superconductivity,* vol. 26, no. 3, pp. 1-5, 2016, doi: 10.1109/TASC.2016.2520210.

CHAPTER 5 Numerical Investigation of HTS Coated-Conductors Under Rotating Magnetic Fields

5.1 Introduction

Since the first high-temperature superconductor (HTS) material was discovered in 1986, HTS materials, including HTS tapes and HTS bulks, have entered industrial applications after three decades of continuous development. HTS wires and tapes are now commercially available, thanks to recent improvements in production. As a result, HTS material has now been used in several large-scale power applications [5.1, 5.2]. HTS material makes it feasible to create small, light-weight, and efficient electrical machines by allowing for both a significant decrease in size and volume and an improvement in machine efficiency. The second generation of HTS tapes is known as coated conductors, or CC tapes, since they are made of a thin coating of superconductor that has been placed over a metallic substrate. Due to their excellent performance, HTS-coated conductors (HTS CCs) are among the most versatile superconducting materials [5.3-5.5]. However, maintaining cryogenic temperature, which is frequently accomplished by employing liquid nitrogen, to preserve its superconducting condition is a substantial challenge towards the commercialisation of these materials. The commercialisation of HTS CCs is also handicapped due to power dissipation when the material is exposed to the AC transport current or alternating magnetic field. The changing magnetic field causes the movement of vortices inside the superconducting material and a phenomenon known as superconducting alternating current (AC) loss. This heat caused by the vortex movement puts additional strain on the cryogenic cooling system and affects the efficiency of the superconducting machines [5.6]. This power loss needs to be removed to ensure the required critical temperature for keeping the material at superconducting mode. Such dissipation puts an additional burden on the cryogenic cooling system. Therefore, the HTS apparatus should be designed with very low power loss and a proper power loss model is crucial for such a design and performance optimisation.

When utilised in rotating machines, HTSCCs are subjected to both alternating and rotating magnetic fields. However, all previous property measurements and modelling were conducted under one-dimensional (1D) alternating AC magnetic fields generated by the current within the HTS conductor or external excitations. Some recent studies by the authors are related to rotating magnetic fields [5.7, 5.8] with HTS bulks [5.9], but a comprehensive analysis of HTSCCs is still needed. Therefore, to deeply comprehend the electromagnetic characteristics

for the effective design of HTS rotating machines, it is necessary to thoroughly explore the electromagnetic characteristics of HTSCCs under rotating magnetic fields.

Current HTS AC loss measuring methods [5.10], including the electrical approach and the calorimetric method, can only measure the AC loss caused by 1D alternating magnetic fields. To create rotating magnetic fields, various particular setups are required. Such arrangements, however, become complicated to handle rotating magnetic fields and a cryogenic environment simultaneously. Analytical models such as Norris and Brand models are also limited to calculating the AC loss in 1D [5.11]. On the other hand, numerical models are capable of overcoming these difficulties. They can forecast the HTS characteristics, including AC losses in various complicated environments and under different magnetic excitations [5.12]. The numerical modelling approach has improved over time to exhibit a significant correlation with experimental measurement [5.13], but this requires extensive software implementation and takes a lot of time to process.

This chapter presents a numerical investigation of electromagnetic characterisation of HTS CCs under rotating magnetic fields based on finite element analysis (FEA), such as AC loss and magnetic flux density distribution in the stacks of HTS CCs under rotating magnetic fields.

5.2 Model Description

In this study a finite element-based 2D H-formulation model was used to consider a homogenisation technique in [5.14, 5.15] to simulate a stack of second-generation high-temperature superconducting tapes subjected to alternating and rotating magnetic fields in the presence of an AC transport current and magnetic field. In order to simulate the electromagnetic behaviour of HTSCC, individual layers are modelled in the original stack, whereas the anisotropic homogeneous technique out-performs the traditional H-formulation method in terms of computation time. In order to preserve the general electromagnetic behaviour of the original stack while "washing out" the geometrical arrangement of the alternating interior structures of insulating, metallic, superconducting, and substrate layers, an anisotropic bulk equivalent of the stack has been developed. This technique requires less computation time compared to modelling the original stack with individual tapes.

When addressing the boundary conditions between the superconductor and other materials within COMSOL Multiphysics, several key considerations must be considered. These include accurately defining the material properties of the superconductor and other materials, implementing appropriate contact interfaces for interactions between different

materials, setting the necessary boundary conditions to capture the desired physical behavior at the interfaces, and incorporating transition or interfacial zones when dealing with gradual material transitions.

A vertical stack of 64 HTS CCs is considered as shown in Figure 5.1. Each tape is manufactured with the ion beam assisted deposition (IBAD) technique, composed of individual layers of silver, YBCO, and substrate, sandwiched with two copper layers, followed by an air gap separating the tape from the next layer. An equivalent anisotropic bulk model can be obtained by "washing out" the tapes' topological characteristics, as shown in Figure 5.2. As a result, the material specifications need to be adjusted.

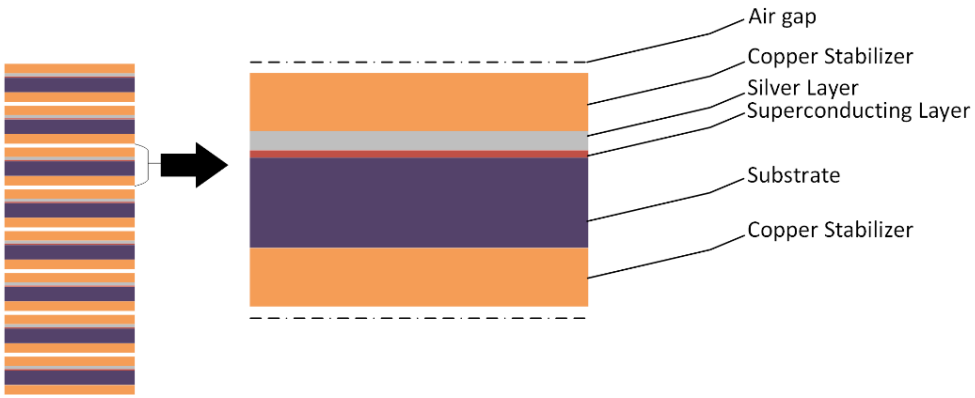

Figure 5.1: A vertical stack of HTS CCs and individual layers of sliver layer, superconducting layer, substrate, and two layers of copper stabilizers.

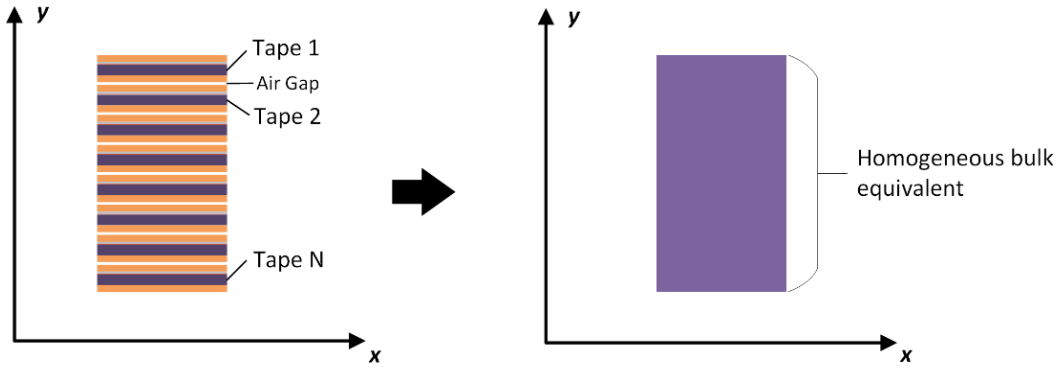

Figure 5.2: Homogeneous model of the vertical stack of CC, where the real topological characteristics of the tapes are "washed out".

Several FEA-based numerical frameworks are commonly employed for simulating the electromagnetic behaviour of High-Temperature Superconducting (HTS) materials [5.16, 5.17, 5.18, 5.19]. These frameworks include the A-V formulation, which utilizes magnetic vector

potential, the T-F formulation based on current vector potential, and the widely used H-formulation [5.16, 5.17, 5.18, 5.19]. The H-formulation incorporates electrical properties of superconductors by employing magnetic field strength as the dependent variable and nonlinear resistivity. It is renowned for its precision, good convergence, short computation time, and excellent agreement with experimental and analytical models such as the Ginzburg-Landau phenomenological model, Norris analytical model, and Brandt analytical model [5.13, 5.14, 5.20, 5.21]. Furthermore, the H-formulation enables self-consistent calculations of the magnetic field [5.22]. The model description of H-formulation is described in Chapters 3 and 4.

H-formulation model is a combination of Maxwell Ampere's Law, Faraday's Law, Constitutive law, Ohm's Law, and *E-J* Power Law. Combining these laws, one obtains the partial differential equation (PDE) in terms of the variable H, as follows:

$$\frac{\partial(\mu_0\mu_r H)}{\partial t} + \nabla \times (\rho \nabla \times H) = 0 \tag{5.1}$$

The above-mentioned PDE can be solved using the commercially available finite element software such as COMSOL Multiphysics [5.24]. Using Dirichlet boundary conditions, an external magnetic field may be applied around the sample's boundary in the air domain. The non-conducting regions are represented by high resistivity materials. A resistivity value of 1 $\Omega.m$ is commonly employed since it is sufficiently large, preventing current flow in non-conducting zones, and it does not significantly increase calculation time. Magnetically, the superconductor is modelled as a material with relative magnetic permeability μ_r = 1. Furthermore, when *J* has a parallel component to *B*, the direction of the current density relative to the magnetic field affects the critical current density, resulting in force-free effects. As a result, high-accuracy models based on $J_c(B)$ and anisotropy dependence are required. To account for the $J_c(B)$ dependency, Kim's model [5.25] is also used to consider such an isotropic behaviour, as shown below (5-2);

$$J_c(B) = \frac{J_{c0}}{\left(1 + \frac{|B|}{B_0}\right)^m} \tag{5.2}$$

Moreover, the H-formulation is considered to be a powerful tool for computation of the AC loss ranging from individual tapes to complex cables and large magnet windings [5.20, 21]. To calculate the AC loss, the dot production of vectors E and J is integrated over the domain of interest, as shown below:

$$Q = \frac{2}{T}\int_{0.5T}^{T}\int_{\Omega} E \cdot J \, d\Omega dt \tag{5.3}$$

where Ω represents the domain for calculating AC loss and T is the period of AC signal. The other relevant parameters used in the model are listed in Table 5.1.

Table 5.1: Model Parameters

Parameter	Symbol	Value
Insulation / air gap	h_l	200 μm
Copper layer	h_{cu}	40 μm
Substrate layer	h_c	50 μm
Silver layer	h_{ag}	2 μm
HTS (YBCO) layer thickness	h_{HTS}	1 μm
Unit thickness	D	293 μm
Tape width	a	4 mm
Air/insulation resistivity	ρ_{Ins}	1 Ω.m
Silver resistivity	ρ_{Ag}	2.70 nΩ.m
Copper resistivity	ρ_{Cu}	1.97 nΩ.m
Substrate resistivity	ρ_{Subs}	1.25 μΩ.m
Permeability of free space	μ_0	$4\pi \times 10^{-7}$ H.m^{-1}
Number of tapes in stack	C	64
Power factor	n	38
Critical current density	J_{c0}	108 A.mm^{-2}
Characteristic electric field	E_0	10^{-4} V m^{-1}
Kim's model arbitrary parameter	B_0	0.0041 T
Kim's model arbitrary parameter	m	0.5

Unlike the microscopic investigations on thin superconductors [5.26, 5.27], this study concentrates on macroscopic phenomenon of the HTS stack, particularly the overall AC loss in the stack. Therefore, some minor microscopic effects that do not greatly affect the overall AC loss can be neglected.

5.3 Rotating Magnetic Fields

In 1D magnetic fields, the magnetic flux density vector B is restrained to flow in the same direction as the magnetic field intensity H. However, in rotating electrical machines, the magnetic field rotates on a 2D plane, with B and H vectors that may not be pointing in the same direction. In order to set up a magnetic field around the HTS CC stack, an external magnetic field is supplied to the superconducting domain. In the case of a 1D alternating field, a sine

wave of the required amplitude is introduced. The applied rotating magnetic field in the case of 2D rotating magnetisation, on the other hand, is just a combination of sine waveforms at the two independent axes, according to the testing requirements, which may be described using the following equations:

$$B_{1D(alt)} = B_0 \sin(\omega t) \tag{5.4}$$

$$B_{2D(rot)} = \begin{cases} B_0 \sin(\omega t) \\ B_0 \sin(\omega t \pm \emptyset)\,(1 - \exp\left(-\frac{t}{\tau}\right)) \end{cases} \tag{5.5}$$

where B_0 is the magnetic flux density amplitude, ω is the angular frequency, and ϕ denotes the phase shift angle, and τ is a time constant of 0.05 s. A purely circular rotating field is produced, which is often achieved by adjusting the phase angle of the second source by 90 degrees (i.e., π/2). When a phase angle is shifted along the axis, the magnetic field's starting value is not equal to zero, which causes an issue with the initial values in FEA and prevents the model from converging. As a result, an exponential step function is used in the second field source in Equation (5.5) Figure 5.3 shows the representation of an HTS CC stack subjected to alternating and rotating magnetic fields while carrying a transport current.

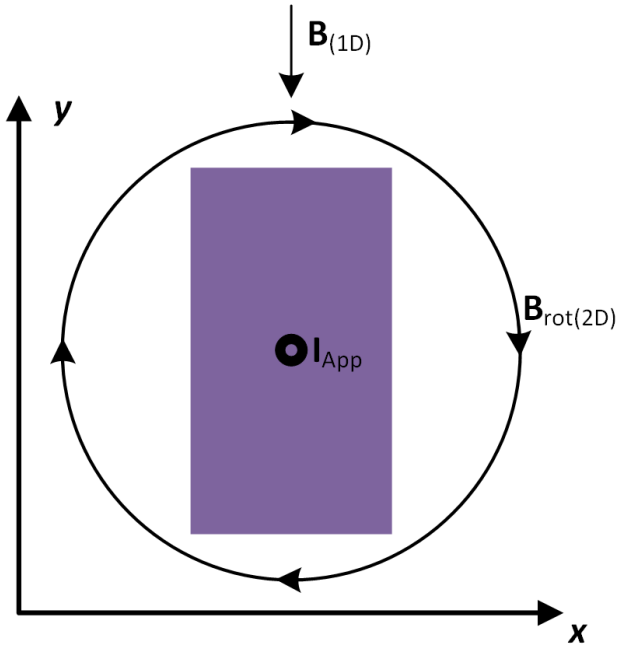

Figure 5.3: HTS CC stack subjected to alternating and rotating magnetic fields while transport current is applied.

5.4 AC Loss Analysis

The AC loss in HTSCC is one of the main characteristics that need to be studied. This paper studies the AC loss of a vertical stack of HTSCC comprising 64 tapes. The stack is subjected to various scenarios comprising alternating and rotating magnetic fields along with the transport current situation at the same time. Rotating magnetic fields are most commonly observed in rotating machines and the HTS bulk is a good option for such applications. Our work is focused mostly on power frequency (50 Hz). For the first case, we only apply the magnetic field across the tapes without any transport current. Magnetic fields of up to 2 T are applied in 1D alternating and the 2D rotating pattern as in Figures 5.4.

Furthermore, we tried to increase the transport current from 0 A up to 50 A in order to understand the loss mechanism in the HTS CCs by exposing them to alternating and rotating magnetic fields along with the transport current scenario. Figures 5.5-5.7 shows the AC loss with transport currents of 10 A, 20 A, and 50 A respectively.

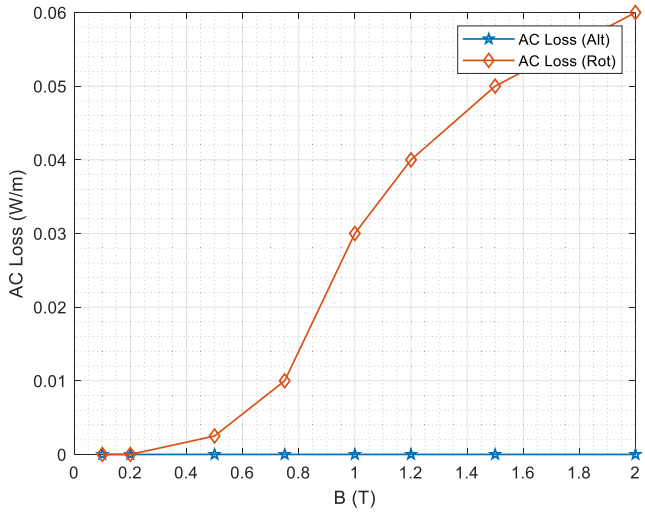

Figure 5.4: AC loss in HTS stack subjected to an alternating and rotating magnetic field without transport current.

It can be seen that with the transport current of 10 A, the AC loss is almost equal for both alternating and rotating magnetisations up to 20 mT. However, it increases significantly up to three times as the magnetic field is increased to 2 T, as shown in Figure 5.5. When a transport current is set to 20 A, the loss seems to be similar at 20mT, but at higher magnetic fields, the difference in the AC loss between alternating and rotating magnetic fields is reduced to 1.5 times as in Figure 5.6. Furthermore, when the transport current is increased to 50 A, the rotating and alternating AC losses become almost the same and there is negligible difference between the two cases, but still the rotating AC loss is higher than alternating AC loss as in

Figure 5.7. The main reason is that at higher currents, the AC loss is mainly due to transport current. It can be assumed that on such high AC loss, the stack may not be operating at superconducting state.

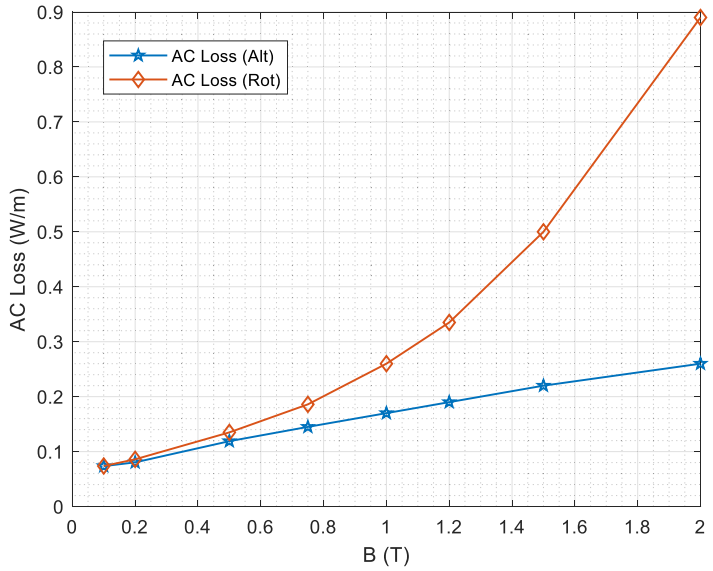

Figure 5.5: AC loss in HTS stack subjected to an alternating and rotating magnetic field with transport current of 10 A.

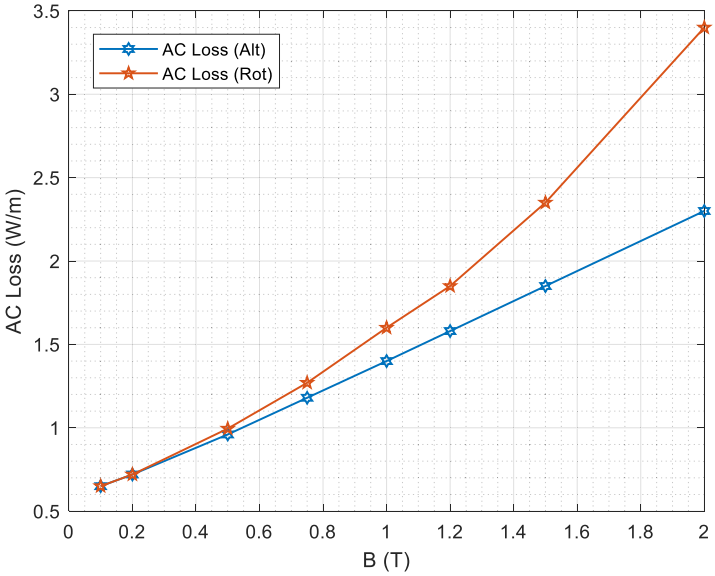

Figure 5.6: AC loss in HTS stack subjected to an alternating and rotating magnetic field with transport current of 20 A.

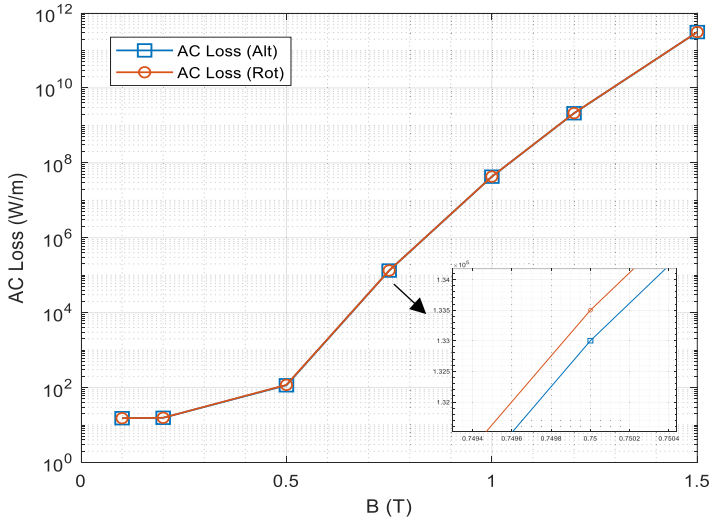

Figure 5.7: AC loss in HTS stack subjected to an alternating and rotating magnetic field with transport current of 50 A.

5.5 Flux Density Maps

Figures 5.8-5.10 show the magnetic flux density distribution maps of the HTS CC stack when a rotating magnetic field is applied with the amplitude of 20 mT. Figure 5.8 shows such distribution without any transport current scenario. At the start of the excitation, the field is distributed along the sides of the stack and reaches the middle of the stack vertically at 10 ms, and then it fades at the edges. Figure 5.9 shows the magnetic flux density distribution of the stack, but in this case a 20 A current is applied. It shows very similar behaviour as per the earlier case but here, a slight drift of the flux density to the left side. Figure 5.9 shows the flux density distribution when a rotating magnetic field of 20 mT is applied along with the transport current of 50 A. In this case, the flux density is distributed more towards the edges and rotating clockwise around the stack.

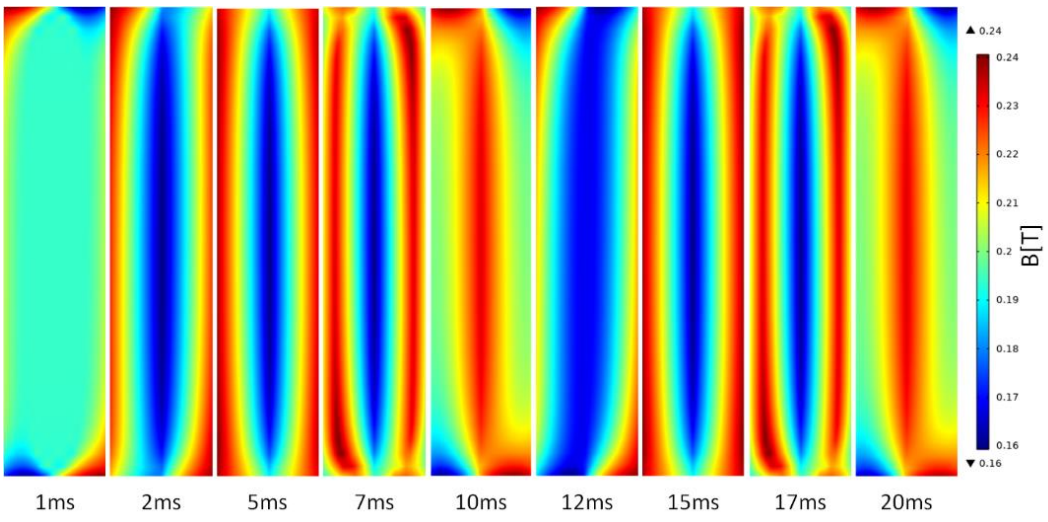

Figure 5.8: Magnetic flux density maps for stacks of HTS CC when subjected to rotating magnetic field of 20mT without any transport current.

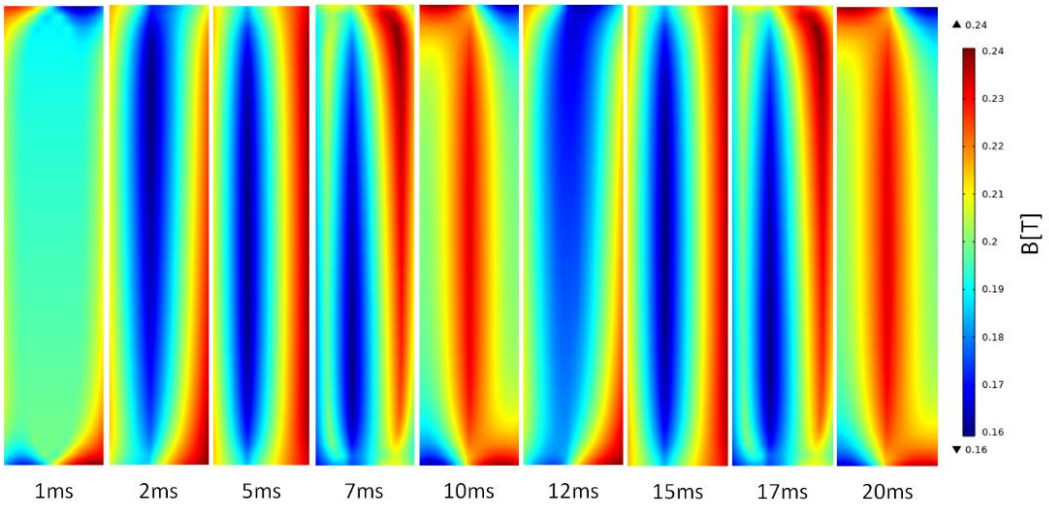

Figure 5.9: Magnetic flux density maps for stacks of HTS CC when subjected to a rotating magnetic field of 20mT while carrying a transport current of 20A.

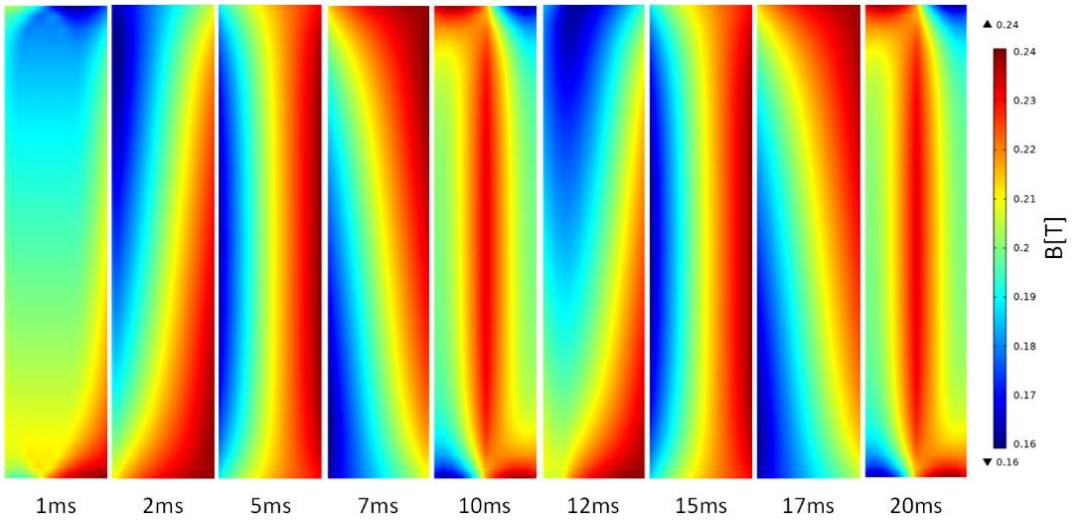

Figure 5.10: Magnetic flux density B maps for stacks of HTS CC when subjected to a rotating magnetic field of 20mT while carrying a transport current of 50A.

5.6 Conclusions

In this study, the electromagnetic behaviour of HTS CCs is investigated using numerical modelling techniques by applying rotating magnetic fields to the stack of HTS CCs. A FEM-based homogenous H-formulation anisotropic bulk model is used, which greatly reduces the model's computation time. The article predicts the behaviour of AC loss under rotating magnetic fields of various amplitudes, along with the transport current situation. Coloured maps of flux density distribution are also shown as a reference to demonstrate the real distribution of magnetic flux density in different time steps and transport currents. As the

AC loss investigations under rotating magnetic fields are not explicitly reported in the literature, this article highlights the preliminary investigation on the subject, which reveals that when HTSCCs are exposed to rotating magnetic fields, the AC loss can be significantly high, which may affect the cooling efficiency. Therefore, such loss model is essential for the design of future high-efficiency and high-power density electrical machines.

Moreover, this study also concludes the need to further investigate the detailed loss mechanism under rotating magnetic fields, such as AC loss separation in various layers of HTS tapes, and frequency dependence. Although numerical models are effective tools for predicting the performance of HTS materials, new analytical models considering the rotating magnetic fields and robust experimental setups are equally critical for investigating the electromagnetic characteristics of HTS materials.

5.7 References

[5-1] W. A. Soomro, Y. Guo, H. Y. Lu, and J. X. Jin, "Advancements and Impediments in Applications of High-Temperature Superconducting Material," *in Proceedings 2020 IEEE International Conference on Applied Superconductivity and Electromagnetic Devices (ASEMD)*, 16-18 Oct. 2020, pp. 1-4, doi: 10.1109/ASEMD49065.2020.9276278.

[5.2] M. Chen, L. Donzel, M. Lakner, and W. Paul, "High temperature superconductors for power applications," *Journal of the European Ceramic Society,* vol. 24, no. 6, pp. 1815-1822, 2004/01/01/ 2004, doi: https://doi.org/10.1016/S0955-2219(03)00443-6.

[5.3] N. Amemiya *et al.*, "AC loss reduction of YBCO coated conductors by multifilamentary structure," *Superconductor Science and Technology,* vol. 17, no. 12, pp. 1464-1471, 2004/11/03 2004, doi: 10.1088/0953-2048/17/12/018.

[5.4] B. Shen *et al.*, "Power dissipation in HTS coated conductor coils under the simultaneous action of AC and DC currents and fields," *Superconductor Science and Technology,* vol. 31, no. 7, p. 075005, 2018.

[5.5] M. Majoros, L. Ye, A. V. Velichko, T. A. Coombs, M. D. Sumption, and E. W. Collings, "Transport AC losses in YBCO coated conductors," *Superconductor Science and Technology,* vol. 20, no. 9, pp. S299-S304, 2007/08/23 2007, doi: 10.1088/0953-2048/20/9/s27.

[5.6] X. Xiao, Y. Liu, J. Jin, C. Li, and F. Xu, "HTS applied to power system: benefits and potential analysis for energy conservation and emission reduction," *IEEE Transactions on Applied Superconductivity,* vol. 26, no. 7, pp. 1-9, 2016, doi: 10.1109/TASC.2016.2594800.

[5.7] W. A. Soomro, Y. Guo, H. Y. Lu, J. G. Zhu, J. X. Jin, and B. Shen, "Numerical investigation of AC loss in HTS bulks subjected to rotating magnetic fields," in *Proceedings 2021 31st Australasian Universities Power Engineering Conference (AUPEC)*, 26-30 Sept. 2021, pp. 1-5, doi: 10.1109/AUPEC52110.2021.9597734.

[5.8] W. A. Soomro, Y. Guo, H. Lu, J. Zhu, J. Jin, and B. Shen, "Three-dimensional numerical characterisation of high-temperature superconductor bulks subjected to rotating magnetic fields," *Energies,* vol. 15, no. 9, p. 3186, 2022. [5.Online]. Available: https://www.mdpi.com/1996-1073/15/9/3186.

[5.9] M. D. Ainslie and H. Fujishiro, "Modelling of bulk superconductor magnetisation," *Superconductor Science and Technology,* vol. 28, no. 5, p. 053002, 2015.

[5.10] Y. Wang, X. Guan, and J. Dai, "Review of AC loss measuring methods for HTS tape and unit," *IEEE Transactions on Applied Superconductivity,* vol. 24, no. 5, pp. 1-6, 2014.

[5.11] B. Shen *et al.*, "Investigation of AC losses in horizontally parallel HTS tapes," *Superconductor Science and Technology,* vol. 30, no. 7, p. 075006, 2017.

[5.12] F. Grilli, E. Pardo, A. Stenvall, D. N. Nguyen, W. Yuan, and F. Gömöry, "Computation of losses in hts under the action of varying magnetic fields and currents," *IEEE Transactions on Applied Superconductivity,* vol. 24, no. 1, pp. 78-110, 2014, doi: 10.1109/TASC.2013.2259827.

[5.13] F. Grilli, "Numerical modeling of HTS applications," *IEEE Transactions on Applied Superconductivity,* vol. 26, no. 3, pp. 1-8, 2016.
[5.14] V. M. R. Zermeno, A. B. Abrahamsen, N. Mijatovic, B. B. Jensen, and M. P. Sørensen, "Calculation of alternating current losses in stacks and coils made of second generation high temperature superconducting tapes for large scale applications," *Journal of Applied Physics,* vol. 114, no. 17, p. 173901, 2013, doi: 10.1063/1.4827375.
[5.15] H. M. WORKGROUP. http://www.htsmodelling.com/?wpdmpro=b5_results-3. (accessed on January 15th 2023)
[5.16] G. P. Lousberg, M. Ausloos, C. Geuzaine, P. Dular, P. Vanderbemden, and B. Vanderheyden, "Numerical simulation of the magnetisation of high-temperature superconductors: a 3D finite element method using a single time-step iteration," *Superconductor Science and Technology,* vol. 22, no. 5, p. 055005, 2009/03/30 2009, doi: 10.1088/0953-2048/22/5/055005.
[5.17] N. Amemiya, S.-i. Murasawa, N. Banno, and K. Miyamoto, "Numerical modelings of superconducting wires for AC loss calculations," *Physica C: Superconductivity,* vol. 310, no. 1, pp. 16-29, 1998/12/01/ 1998, doi: https://doi.org/10.1016/S0921-4534(98)00427-4.
[5.18] G. Escamez *et al.*, "3-D numerical modeling of AC losses in multifilamentary MgB2Wires," *IEEE Transactions on Applied Superconductivity,* vol. 26, no. 3, pp. 1-7, 2016, doi: 10.1109/TASC.2016.2533024.
[5.19] J. Xia, H. Bai, J. Lu, A. V. Gavrilin, Y. Zhou, and H. W. Weijers, "Electromagnetic modeling of REBCO high field coils by the H-formulation," *Superconductor Science and Technology,* vol. 28, no. 12, p. 125004, 2015.
[5.20] B. Shen, F. Grilli, and T. Coombs, "Overview of H-formulation: A versatile tool for modeling electromagnetics in high-temperature superconductor applications," *IEEE Access,* vol. 8, pp. 100403-100414, 2020.
[5.21] B. Shen, F. Grilli, and T. Coombs, "Review of the AC Loss Computation for HTS using the H-formulation," *arXiv preprint arXiv:1908.02176,* 2019.
[5.22] F. Grilli, F. Sirois, V. M. R. Zermeño, and M. Vojenčiak, "Self-consistent modeling of the Ic of HTS devices: how accurate do models really need to be?," *IEEE Transactions on Applied Superconductivity,* vol. 24, no. 6, pp. 1-8, 2014, doi: 10.1109/TASC.2014.2326925.
[5.23] C. P. Bean, "Magnetisation of hard superconductors," *Physical Review Letters,* vol. 8, no. 6, p. 250, 1962.
[5.24] R. Brambilla, F. Grilli, and L. Martini, "Development of an edge-element model for AC loss computation of high-temperature superconductors," *Superconductor Science and Technology,* vol. 20, no. 1, pp. 16-24, 2006/11/20 2006, doi: 10.1088/0953-2048/20/1/004.
[5.25] D. X. Chen and R. B. Goldfarb, "Kim model for magnetisation of type-II superconductors," *Journal of Applied Physics,* vol. 66, no. 6, pp. 2489-2500, 1989.
[5.26] D. Saint-James and P. d. Gennes, "Onset of superconductivity in decreasing fields," *Physics Letters,* vol. 7, no. 5, pp. 306-308, 1963.
[5.27] M. Croitoru, A. Shanenko, Y. Chen, A. Vagov, and J. A. Aguiar, "Microscopic description of surface superconductivity," *Physical Review B,* vol. 102, no. 5, p. 054513, 2020.

CHAPTER 6 **Experimental Set-up for Measurement of AC Loss in HTSs Under Rotating Magnetic Field**

6.1 Introduction

The commercialisation of HTS is further hampered by dissipative interactions that occur when the superconductor is exposed to an alternating magnetic field. This phenomenon is characterised as superconducting alternating current (AC) loss, and it is caused by the movement of vortices inside the superconducting material [6.1], and it can place additional strain on the cryogenic cooling system. This power dissipation is affected by a variety of parameters, including the geometry of the material, the direction of the applied magnetic field, and the distribution of current density inside the material. As a result, it is critical to explore the electromagnetic characteristics of HTS bulks in order to ensure the viability of these materials.

Furthermore, while designing practical and commercial applications, a cryogenic cooling unit or a cryo-cooler is installed, which extracts the corresponding heat load for maintaining a constant temperature during the process. The AC losses may complicate the stability of the cryogenic system, which affects the overall efficiency of the device. Therefore, a deep understanding of the mechanism and magnitude of AC loss is enormously essential for the design and development of new superconducting machines.

When employed in rotating machinery, HTS permanent magnets may be subjected to both alternating and rotating magnetic fields. However, the majority of electromagnetic investigations in the literature focus on the characterisation of HTS bulk exposed to a one-dimensional alternating magnetic field. Due to the lack of a robust HTS rotating magnetic property testing apparatus, several experimental approaches documented in the literature, mostly on AC loss, rely solely on one-dimensional exposure. As a result, the electromagnetic characterisation of HTS bulks in rotating magnetic fields remains unknown and must be explored in order to completely understand electromagnetic features for the efficient design of HTS rotating machines.

There are some recent studies from the authors which focus on the numerical investigations of AC loss under rotating magnetic fields [6.2-6.4], where it was understood that the AC loss changes significantly under the exposure of rotating magnetic fields compared to one-dimensional magnetisation. These numerical models are powerful tools to predict the performance of the HTS material, but experimental techniques are also really important for the

investigation of HTS electromagnetic properties. There are some experimental techniques reported in the literature to measure the AC loss by the exposure of the AC magnetic fields or under the transport current situation. But, looking at the limitation of the existing methods, there is a lack of robust experimental methods to measure the material properties under rotating magnetic fields, especially the AC loss.

This chapter reports a new experimental technique to measure the AC loss of HTS under a rotating magnetic field. A square specimen tester (SST) is used to generate a rotating magnetic field around the sample, where AC loss can be measured using the field metric method.

6.2 Existing AC loss Measurement Techniques

In order to measure the AC loss of the superconductors experimentally, there are three common methods: the electric method [6.5], the magnetic method [6.6], and the calorimetric method [6.7]. These methods will be described below, along with their advantages and limitations, with the focus on the electrical method, which is widely used by researchers and does not require specialised equipment as compared to the other two methods.

6.2.1 Magnetic Method

In the magnetic method, there is specific standard equipment such as superconducting quantum interference devices (SQUIDs) and vibrating sample magnetometers (VSM). Furthermore, there are two approaches that are useful in order to determine the AC loss stated as follows.

6.2.1.1 Hysteresis Loop

SQUIDs and VSM are generally used to measure the hysteresis loop in superconductors, but this is applicable mostly for small samples or coils. Once the hysteresis loop is measured, the hysteresis loss can be easily obtained by integrating the hysteresis loop.

$$P_h = CA\mu_0 \oint H_e dM = -CA\,\mu_0 \oint M dH_e \tag{6.1}$$

where C is the effective cross-section area coefficient (C = 1 at low frequency), A is the geometrical cross-section area of the sample, μ_0 is the vacuum permeability, H_e is the applied

AC magnetic field strength, and M is the magnetisation which can be measured using the VSM and SQUIDs.

6.2.1.2 AC Susceptibility

The imaginary part of the complex AC susceptibility can also be used to derive the hysteresis loop. If both uniform DC magnetic flux density B_0 and AC magnetic flux density $B(t)$ are imposed on the superconducting sample, and AC magnetic flux density is in the form of sinusoidal $B(t) = B_m \sin(\omega t)$, then the total imposed magnetic flux density on the sample will be:

$$B(t) = B_0 + B_m \sin(\omega t) \tag{6.2}$$

where B_m is the amplitude, and $\omega = 2\pi f$ is the angular frequency of the AC magnetic field. Both DC and AC magnetic fields are imposed by external sources. The hysteresis loss dependence on the imaginary part of AC susceptibility can be calculated by:

$$P_h = CAf \frac{\pi B_m^2}{\mu_0} \chi'' \tag{6.3}$$

where χ'' is the imaginary part of the AC susceptibility χ. Hence, hysteresis loss can be obtained if the AC susceptibility is measured.

6.2.2 Electrical Method

AC loss, which is mainly hysteresis loss, is produced when a superconducting sample is exposed to an alternating field or carries a transport AC current. In order to measure such loss, the electrical method is the most commonly used approach, which involves electronic circuitry, pick-up coils, lock-in amplifier technique, or a combination of both pick-up coils and lock-in amplifier in case there is transport current as well as the externally applied voltage.

6.2.2.1 Pick-up Coils Method

When the superconductor is exposed to the AC magnetic source, energy is dissipated in the superconductor as a result of hysteresis or coupling losses. The magnetic energy dissipated in one cycle is referred to as magnetisation loss [6.7]. The magnetic movement

variation in the superconductor is measured by the voltages of the pick-up coils around the sample. The overall system comprises a magnetic source, a cryostat, HTS sample, a pick-up coil, a cancel or compensation coil along with a compensation circuit, isolation amplifiers, and data acquisition and processing system. The voltage difference between the pick-up coil and the compensation coil can be calculated as $V = V_p - kV_c$, where V_p and V_c are the induced voltages in pick-up and compensation coil, respectively in the presence of external applied magnetic field strength H_e, k is the adjustable coefficient to cancel the background loss. By measuring these voltages, AC loss can be derived as follows [6.8]:

$$P_h = -\frac{A_s}{V_s n_p}\frac{G}{T}\int_0^T (V_p - kV_c)H_e dt \tag{6.4}$$

where V_s and A_s are the volume and cross-sectional area around the main coil, G is the geometric correction factor, np is the number of turns per unit length of the pick-up coil, and T is the time period of the applied external magnetic field H_e. The geometrical correction factor G plays an important part in the measurement process, and it is really difficult to avoid geometrical error in the experimental set-up [6.8].

6.2.2.2 Lock-in-Amplifier Method

When an AC source transmits the current, the superconductor dissipates some of the energy due to flux creep or self-field loss [6.5]. The energy dissipated during each AC cycle is known as transport loss. Transport AC loss is expected to be a resistive load and can be estimated through an electrical method where the voltage in-phase with the current is measured [6.5]. Generally, the current signal is very large, while the voltage is very weak because superconductors operate at very high currents but negligible resistance. Due to nonlinear characteristics, the AC loss voltage signal does not have a good sine waveform. Therefore, it is challenging to measure the AC loss by the voltage signal that should be separated from noise. To eliminate the noise from the voltage signal, the lock-in amplifier technique is used, where a cancel coil is installed to reduce the noise. The reference current is derived through a non-inductive type resistor, which is connected in series with a superconductor.

A resistive reference signal for the lock-in amplifier is provided by the non-inductive resistor in order to measure the root mean square (RMS) value of the transport current I_{rms}. Hence, the RMS value of the loss voltage can also be measured by a lock-in amplifier, which can lead to the derivation of transport AC loss or self-field loss.

$$P = \frac{I_{rms} V_{rms}}{L} \tag{6.5}$$

where I_{rms} is the RMS value of transport current in the sample, V_{rms} is the RMS value of loss voltage, and L represents the length between two terminal voltages.

6.2.3 Calorimetric Method

When a superconductor is exposed to an external magnetic field or an AC current is transmitted, the resulting AC loss will create an adiabatic situation. The AC loss can then be measured by the rise of temperature or by measuring the volume of evaporated cryogen. The calorimetric method has been reported in four different ways; measuring the amount of liquid nitrogen that is evaporated from the cryostat, the measurement of the rise in temperature of the superconductor, measurement of the temperature difference in the flowing liquid nitrogen and the level of liquid nitrogen in the cryostat [6.7].

The calorimetric method has the advantage that it is not sensitive to unwanted alternating currents or magnetic field disturbances. However, the thermal influences from the external environment, such as ohmic dissipation in the current leads or head leakage from the cryostat, may affect the performance of the calorimetric method [6.7].

6.3 AC Loss Measurement Under Rotating Magnetic Field

The measurement techniques for AC loss analysis presented in the previous studies are all under one-dimensional (1D) alternating magnetic fields generated by the transport current in the HTS material itself or through external excitations. In 1D fields, the magnetic flux density vector, B, is restrained from flowing in the same direction as magnetic field strength, H. However, in power system applications such as three-phase transformers or electrical machines, the magnetic field is generally rotating with a two-dimensional pattern, where B and H are in a different direction or not even in the same plane. But unfortunately, the AC loss due to exposure to a rotating magnetic field cannot be investigated by existing experimental techniques due to the experimental limitations in the existing methods. The numerical studies on the AC loss show that the rotating AC loss may be much higher compared to 1D magnetic fields [6.9-6.11].

In order to investigate such behaviour of superconductors under rotating magnetic fields, a modified SST is used to generate a purely circular magnetic field. A precisely

fabricated liquid nitrogen box is installed in the middle of the tester, where a bulk sample is housed inside. In this investigation, a square sample of HTS bulk is used for the investigation. HTS bulks are originated from RE-Ba-Cu-O (RE stands for rare-earth element), such as Yttrium barium copper oxide (Y-Ba-Cu-O), and are fabricated using top-seeded melt growth technique. These materials can trap large magnetic fields at low temperatures, contrary to the traditional permanent magnets. Furthermore, the sample size and value of the critical current density can greatly improve the magnetic field strength trapped in HTS permanent magnets. These trapped field magnets are excellent candidates for developing small, light, and energy-efficient electrical machines with exceptional high-power densities, such as high-performance electric motors and HTS magnetic levitation, because to this unique characteristic. The geometry of this material makes it the ideal candidate for our investigation.

6.4 Square Specimen Tester (SST)

A square specimen tester presented by Brix *et al*. [6.12] is advantageous for detecting 2D power loss because of its flexible control mechanism, more uniform magnetic field, and greater precision than any other standard measurement device. In this study, a modified single-sheet SST [6.13, 6.14] is used to investigate the rotating dissipative AC loss characteristics of the HTS bulk sample. The SST comprises yokes composed of silicon steel sheets that are grain-oriented and vertically laminated. The tester features four wedge-shaped magnetic poles thanks to the construction of the yokes' forms. On the X- and Y-axes magnetic poles, two sets of excitation coils are linked in series to one another. Each coil has 300 turns of insulated copper wire that is 1.6 mm in diameter. A precisely fabricated liquid nitrogen box was installed in the middle of the taster to house the HTS sample submerged in liquid nitrogen. A square specimen of the material is positioned in the tester's centre. Figures 6.1 and 6.2 depict the equivalent block diagram of the 2-D experimental set-up and positioning of a liquid nitrogen box, respectively.

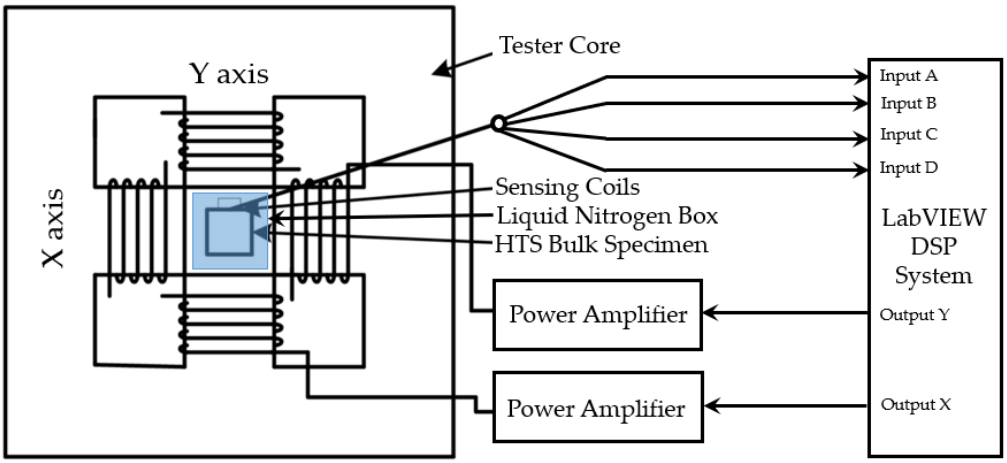

Figure 6.1. Equivalent block diagram of square specimen tester (SST).

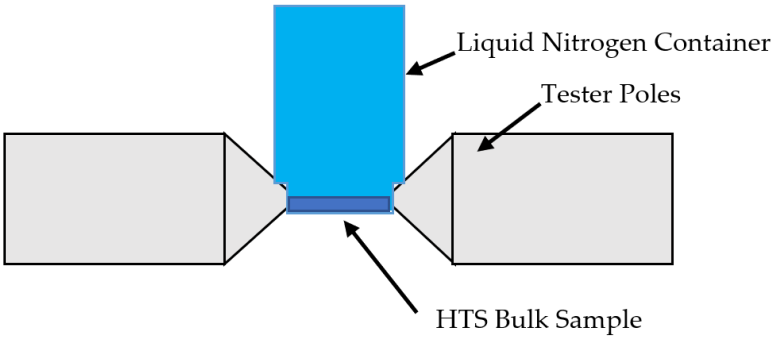

Figure 6.2. Arrangement of the HTS sample and liquid nitrogen box in SST.

The two sets of exciting coils are then excited to create the rotating magnetic field surrounding the sample. To create rotating magnetic fields, two-channel excitation signals with a 90° phase difference are produced using LabVIEW via the power amplifiers. The magnetisation in the specimen is induced by the tester's rotating magnetic field, and the induced magnetisations are then monitored along both axes by specially designed and calibrated B and H sensing coils, respectively. An FPGA-based digital processing system is used for both function generation and data acquisition.

6.5 AC Loss Measurement

In order to validate the effectiveness and performance of the SST, in this experiment set-up, a square sample of HTS bulk can be systematically tested under various B vectors rotating in a circular orientation. Specialised B and H-coils are used in order to determine the X- and Y- components of the flux density (B_x and B_y) and magnetic field strength (H_x and H_y), respectively.

Specially designed sensing coils that are positioned all over the specimen are used to measure the B and H. Using the field-metric approach, and the rotating AC loss is then worked out by measuring the component of B and H. These measured quantities are obtained by inducing the micro volt range voltage in the coils. To solve the low voltage measurement issues, both types of sensing coils are used with precision operational amplifiers.

To measure the B components, 20 turns of 0.1 mm enamel-insulated copper wire make up each coil. The induced voltage in the coils is then incorporated in the following equation, which is then used to obtain the components of B on each axis:

$$B_i = \frac{1}{K_{B_i}} \int V_{B_i} dt \quad (\mathrm{i} = \mathrm{x}, \mathrm{y}) \tag{6.6}$$

$$K_{B_i} = N_{B_i} A_{sp} \tag{6.7}$$

where V_{B_i} is the voltage induced in the coils, K_{B_i} is the coefficients of coil, which considers the number of turns and the cross-section area of the specimen [6.12].

To measure the H components, one coil is placed in the X-axis direction and the other in the Y-axis direction while the B-sensing coils are looped across the centre of the specimen. A 0.50 mm plastic former is twisted with 100 turns of 0.06 mm enamel insulated copper wire to create the H-sensing coil for each axis. The induced voltage in the coils is then incorporated in the following equation [6.13], which is then used to get the components of H on each axis:

$$H_i = \frac{1}{\mu_0 K_{H_i}} \int V_{H_i} dt \quad (i = x, y) \tag{6.8}$$

where μ_0 is the permeability of air, V_{H_i} are the induced voltages in the sensing coils, and K_{H_i} are the coil coefficients, obtained by calibrating the coils in the long solenoid method [6.13]. In order to determine the value of K_{H_i}, the sensing coils placed inside of a long solenoid. After the placement, the corresponding voltage induced across the sensing coil is measured by a

precision volt meter, and magnetic flux density inside the coil is measured using a Gauss meter. The coils are adjusted in such a way that a maximum voltage can be induced in each coil. Moreover, another way to calculate the flux density in the solenoid could also be utilised, which is computed from the measured excitation current and the solenoid's *B/I* ratio. The value of K_{H_i} is then calculated by the following equation.

$$K_{H_i} = \frac{Vs_{H_i}}{2\pi\mu_0 f H_m} \quad (i = x, y) \tag{6.9}$$

where H_m is the maximum field strength, f is the excitation frequency, and Vs_{H_i} is the peak voltage induced in the sensor. The solenoid coil is excited with various excitation currents and the corresponding K_{H_i} is calculated using (6.8) for each excitation. The average value is then taken from all of the calculated values. The calibration set-up can be shown in Figure 6.3, where *A* is the frame, *B* is the *H* coils to be calibrated, *C* is the Gauss meter probe, *D* is the connector for outputting the coil terminal voltage signals, E is the turn table for placing the coils, and *F* and *G* are the wheel rubber bands for adjusting the coil orientation.

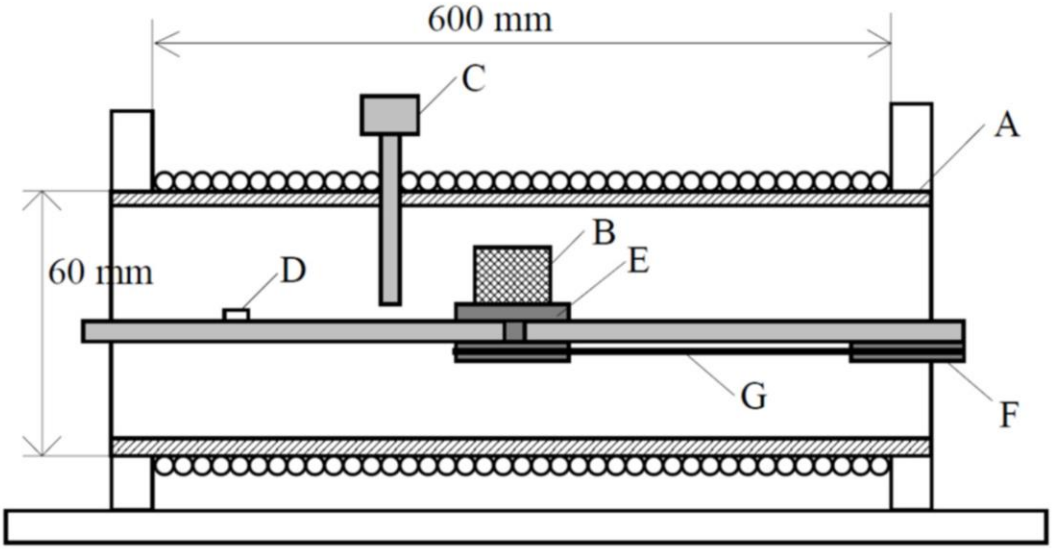

Figure 6.3. Calibration of H sensing coils using long solenoid Method.

From the measured X- and Y- components of magnetic flux density and field strength, the *B-H* relationship can be analysed. Moreover, these measured instantaneous values of *B* and *H* can yield additional information such as various loss contributions, the loci of *H* and *B* vectors, and harmonics etc. Furthermore, power dissipation which occurs when a rotating

magnetic field is applied to a magnetic material specimen, can be measured according to Poynting's theorem [6.13]:

$$P = \frac{1}{T\rho_m}\int_0^T \left(H_x \cdot \frac{dB_x}{dt} + H_y \cdot \frac{dB_y}{dt}\right) dt \tag{6.10}$$

where T is the time period of one magnetisation process, ρ_m is the sample mass density, and H_x, H_y and B_x, B_y are the X- and Y- components of H and B, respectively.

6.6 Misalignment of H Sensing Coils

The estimation of power loss deviates from its original values due to the misalignment of the H-sensing coils with the prescribed axis. By averaging the power losses in both the clockwise and anticlockwise rotating magnetic field directions, the impact of the misalignment of H-sensing coils on the power loss computation can be removed. Furthermore, by rotating the coordinate axes as indicated in Figure 6.4, the impact of misalignment of the H-sensing coils on the magnetic field strength can also be eliminated. The correction of misalignment can be done by following the equation [6.14].

$$\begin{bmatrix} C_x \\ C_x \end{bmatrix} = \frac{1}{\cos a_x \cos a_y + \sin a_x \sin a_y} \begin{bmatrix} \cos a_y & -\sin a_x \\ \sin a_y & \cos a_x \end{bmatrix} \begin{bmatrix} C'_x \\ C_x \end{bmatrix} \tag{6.11}$$

where a_x and a_y are the misalignment angles with X- and Y-axes, respectively, C_x and C_y are the corrected values, and C'_x *and* C_y are the corresponding measured values. Moreover, the misalignment angles are then calculated as follows.

$$a_x = \cos^{-1}\left(\pm A_x \sqrt{\frac{1 - A_y^2}{A_x^2 - A_y^2}}\right) \tag{6.12}$$

$$a_y = \cos^{-1}\left(\frac{\sin a_x}{A_y}\right) \tag{6.13}$$

where $A_x = C'_x / C'_y$ when only the X-axis coils are excited and $A_y = C'_x / C'_y$ when only Y-axis coils are excited.

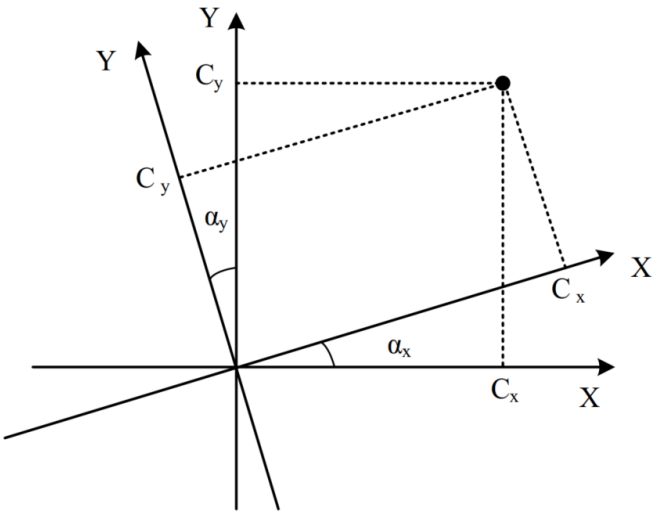

Figure 6.4: Correction of misalignment of the H sensing coils.

6.7 Conclusions

The AC loss measurement is no doubt, one of the most important aspect of the HTS characterisation. The existing methods about the AC loss computation only focus on the loss measurement under one-dimensional (1D) alternating magnetic fields generated by the transport current in the HTS material itself or through external excitations. However, with the limitations in the existing measurement systems, it is impossible to investigate the AC loss under the exposure of rotating magnetic fields. This article presents a new experimental setup in order to measure the AC loss in HTS material upon exposure to the rotating magnetic field. This method will be helpful in the further characterisation of HTS material, especially under the rotating magnetic fields, in order to design large scare HTS applications.

6.8 References

[6.1] M. Majoros, B. A. Glowacki, A. M. Campbell, G. A. Levin, and P. N. Barnes, "Transport AC losses in striated YBCO coated conductors," *Journal of Physics: Conference Series,* vol. 43, pp. 564-567, 2006/06/01 2006, doi: 10.1088/1742-6596/43/1/139.

[6.2] W. A. Soomro, Y. Guo, H. Lu, J. Zhu, J. Jin, and B. Shen, "Three-Dimensional Numerical Characterisation of High-Temperature Superconductor Bulks Subjected to Rotating Magnetic Fields," *Energies,* vol. 15, no. 9, p. 3186, 2022.

[6.3] W. A. Soomro, Y. Guo, H. Lu, J. Jin, B. Shen, and J. Zhu, "Numerical Investigation of High-Temperature Superconducting-Coated-Conductors Subjected to Rotating Magnetic Fields," *Solids,* vol. 3, no. 4, pp. 569-577, 2022.

[6.4] W. A. Soomro, Y. Guo, H. Y. Lu, J. G. Zhu, J. X. Jin, and B. Shen, "Numerical Investigation of AC Loss in HTS Bulks Subjected to Rotating Magnetic Fields," in *2021 31st Australasian Universities*

Power Engineering Conference (AUPEC), 26-30 Sept. 2021 2021, pp. 1-5, doi: 10.1109/AUPEC52110.2021.9597734.

[6.5] H. Daffix and P. Tixador, "Electrical AC loss measurements in superconducting coils," *IEEE Transactions on Applied Superconductivity,* vol. 7, no. 2, pp. 286-289, 1997, doi: 10.1109/77.614486.

[6.6] *Superconductivity-Part 8: AC loss measurements. Total AC loss measurement of round superconducting wires exposed to a transverse alternating magnetic field at liquid helium temperature by a pick-up coil method* (IEC Std. 61788-8, 2010, 2nd ed.). 2010.

[6.7] H. Huang, C. Zhang, and S. Yan, "Calorimetric measurement of AC losses of superconducting magnet," *Acta Physica Temperature Humilis Sinica,* vol. 3, no. 1, pp. 42-46, 1981.

[6.8] K. Kajikawa, M. Iwakuma, K. Funaki, M. Wada, and A. Takenaka, "Influences of geometrical configuration on AC loss measurement with pickup-coil method," *IEEE Transactions on Applied Superconductivity,* vol. 9, no. 2, pp. 746-749, 1999.

[6.9] Y. G. Guo, J. G. Zhu, and J. J. Zhong, "Measurement and modelling of magnetic properties of soft magnetic composite material under 2D vector magnetisations," *Journal of Magnetism and Magnetic Materials,* vol. 302, no. 1, pp. 14-19, 2006/07/01/ 2006, doi: https://doi.org/10.1016/j.jmmm.2005.08.023.

[6.10] Y. Guo, J. G. Zhu, J. Zhong, H. Lu, and J. X. Jin, "Measurement and modeling of rotational core losses of soft magnetic materials used in electrical machines: A review," *IEEE Transactions on Magnetics,* vol. 44, no. 2, pp. 279-291, 2008.

[6.11] P. C. Sarker, Y. Guo, H. Y. Lu, and J. G. Zhu, "Measurement and Modeling of Rotational Core Loss of Fe-Based Amorphous Magnetic Material Under 2-D Magnetic Excitation," *IEEE Transactions on Magnetics,* vol. 57, no. 11, pp. 1-8, 2021.

[6.12] W. Brix, K. Hempel, and F. Schulte, "Improved method for the investigation of the rotational magnetisation process in electrical steel sheets," *IEEE Transactions on Magnetics,* vol. 20, no. 5, pp. 1708-1710, 1984.

[6.13] J. G. Zhu, "Numerical modelling of magnetic materials for computer aided design of electromagnetic devices," PhD Thesis, University of Technology Sydney, 1994.

[6.14] J. G. Zhu and V. S. Ramsden, "Two dimensional measurement of magnetic field and core loss using a square specimen tester," *IEEE Transactions on Magnetics,* vol. 29, no. 6, pp. 2995-2997, 1993.

CHAPTER 7 **Experimental Investigation of AC Loss in HTS Bulks Subjected to Alternating and Rotating Magnetic Fields**

7.1 Introduction

HTS-trapped field magnets could be exposed to alternating and rotating magnetic fields when used in rotating machines. But most electromagnetic studies in the literature concentrate on characterizing HTS material only under one-dimensional alternating magnetic fields. Numerous experimental methodologies published on AC loss, only emphasize on one-dimensional exposure of AC magnetic fields due to the unavailability of reliable testing methods under rotating magnetic field conditions. Few studies have been published that provide some information on the magnetic movement [7.1, 7.2] and the levitational force [7.3], but a comprehensive experimental study on AC loss has not been presented. The electromagnetic characteristics of HTS materials in rotating magnetic fields need to be investigated in order to fully comprehend electromagnetic characteristics for the effective design of HTS rotating machines. Recent works by the authors [7.4-7.6] concentrate on numerical analyses of AC loss due to rotating magnetic fields, where it was discovered that such AC loss differs dramatically from one-dimensional magnetisation when exposed to rotating magnetic fields. Although these numerical models are effective in determining how the HTS material will behave, experimental methods are equally crucial for examining the HTS electromagnetic characteristics.

The experimental methods for AC loss analysis described in the earlier research, such as Electrical Method [7.7], Magnetic Method [7.8], and Calorimetric Method [7.9] are also carried out in the presence of one-dimensional (1D) alternating magnetic fields formed by the transporting current or by external excitations. In contrast, the magnetic field rotates in a two-dimensional pattern in applications like three-phase transformers or electrical machines, where B and H may not be in the same direction. Because of the experimental restrictions in existing methods, it is not possible to evaluate the AC loss caused by exposure to rotating magnetic fields.

The authors have presented a unique experimental approach for measuring AC loss in rotating magnetic fields in [7.10], where only the experimental set up has been proposed. The details of the experimental approach have been described in detail in Chapter 6. In this chapter, a detailed investigation of the AC loss measurement is presented using this novel experimental

setup. This detailed characterisation would be beneficial for the further design of large scale high-efficient superconducting rotating machines.

7.2 HTS Bulk Sample

In this investigation, a square sample of Melt textured RE-$Ba_2Cu_3O_7$-x with RE_2BaCuO_5 excess HTS bulk is used for the investigation. HTS bulks originated from RE-Ba-Cu-O (RE stands for rare-earth element), such as Yttrium barium copper oxide (Y-Ba-Cu-O), and are fabricated using the top-seeded melt growth technique. These materials can trap large magnetic fields at low temperatures, contrary to the traditional permanent magnets. Furthermore, the sample size and value of the critical current density can greatly improve the magnetic field strength trapped in HTS permanent magnets. These trapped field magnets are excellent candidates for developing small, light, and energy-efficient electrical machines with exceptional high-power densities, such as high-performance electric motors and HTS magnetic levitation, because to this unique characteristic. The geometry of this material makes it the ideal candidate for our investigation. Two customised samples with the dimension of 40mm x 40mm x 10mm and 40mm x 40mm x 5mm were procured to suit the tester specimen requirement. The corresponding images of the specimens are shown in Figure 7.1.

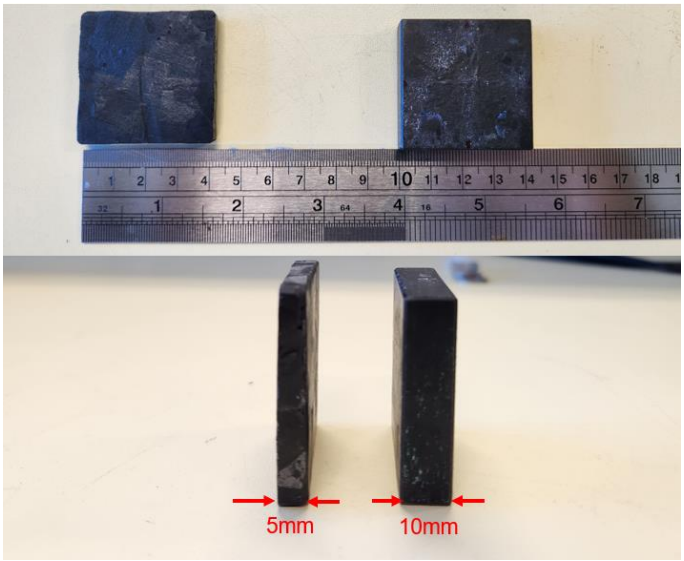

Figure 7.1. HTS specimens for used in the experiment

7.3 Results and Discussion

A square sample of Melt textured RE-$Ba_2Cu_3O_7$-x with RE_2BaCuO_5 excess HTS bulk sample is exposed to alternating and rotating magnetic fields with various amplitudes and frequencies. Two samples of different thicknesses are used in this study. The results are also compared with those from the numerical modelling. The details about the numerical model has been presented in earlier chapters, Figure 7.2 shows the numerical equivalent of HTS Bulk sample.

A new measurement approach recently described in [7.10] has been extended to study the AC loss behaviour in the HTS bulks. A square HTS bulk specimen was prepared by incorporating sensing coils for sensing components of *B* and *H*. To maintain the specimen in the superconducting area, it is carefully inserted in the specimen slot and immersed in liquid nitrogen. The level of liquid nitrogen is kept constant to maintain the desirable cryogenic condition required for superconductivity. Figure 7.3 depicts a view of the experimental setup showing different equipment and components.

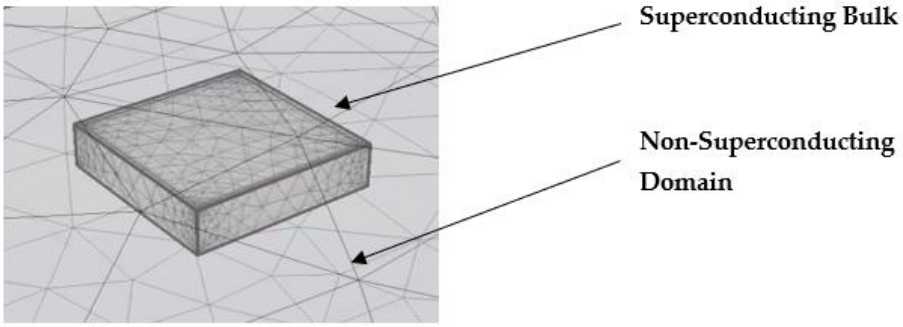

Figure 7.2 Numerical equivalent HTS Bulk sample.

Figure 7.3. An image of the tester during the experiment.

Once the experimental setup is deployed and the cryogenic condition is sustained, the setup is organised for the measurements. When the specimen is subjected to an external field, the loss is absorbed instantly, resulting in an adiabatic state. In this experiment, the HTS sample is entirely immersed in liquid nitrogen, and the volume is continuously sustained in the container by frequently pouring the liquid nitrogen over the sample.

To study the AC loss characteristics in detail, the HTS specimen is subjected to various alternating and rotating magnetic flux density patterns with different amplitudes and frequencies. Furthermore, the results are also put in comparison with those from the numerical modelling methods. In order to confirm the rotation of the magnetic field in a purely circular form, Figure 7.4 depicts an example of the controlled loci of B and corresponding loci of H at 90mT magnetic flux density and 50Hz frequency in the specimen with 10mm thickness. The loci of H are not circular when compared to the loci of B because the permeability differs with the value of B. Furthermore, the maximum values of H_x and H_y are not the same because the material responds differently when magnetised in the X and Y directions.

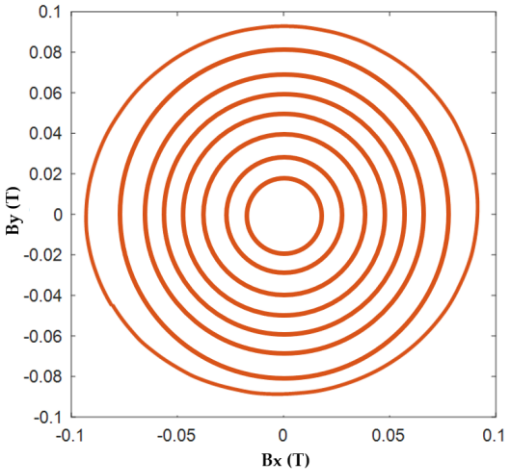

(a)

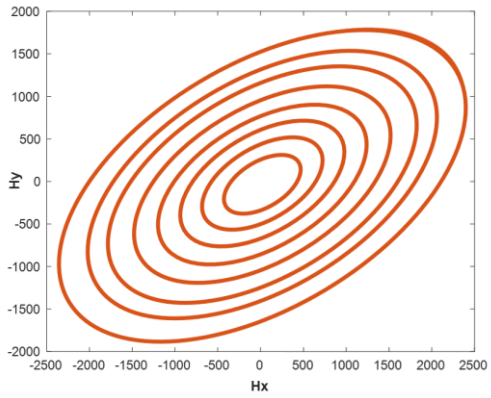

(b)

Figure 7.4. Loci of (a) Magnetic flux density (B) and (b) Magnetic fields strength (H) with 90mT magnitude of B in the specimen with 10mm thickness.

Figure 7.5 shows more comprehensive loss variations when the HTS sample with a thickness of 10mm is exposed to various alternating and rotating magnetic fields up to 90mT. In order to compare the loss under rotating excitations, one-dimensional loss measurements are also obtained. In this case, only the coils in the particular orientations are excited to magnetise the sample in the X- or Y-axis, as described in section 2. The loss under one-dimensional magnetic fields shows a traditional increment when the sample is exposed to higher fields. The subsequent results are also compared with the loss computed from numerical modelling, which shows similar behaviour. Furthermore, the sample is exposed to various rotating magnetic fields in circular patterns, where both of the tester coils are excited, as explained in Section 7.2. The results show that the AC power dissipative loss under rotating magnetic fields is significantly higher compared to the AC loss in one-dimensional AC loss, and it is logarithmically increasing with higher amplitudes of the magnetic fields. The two-dimensional experimental results also agree with the numerical investigations presented in earlier studies.

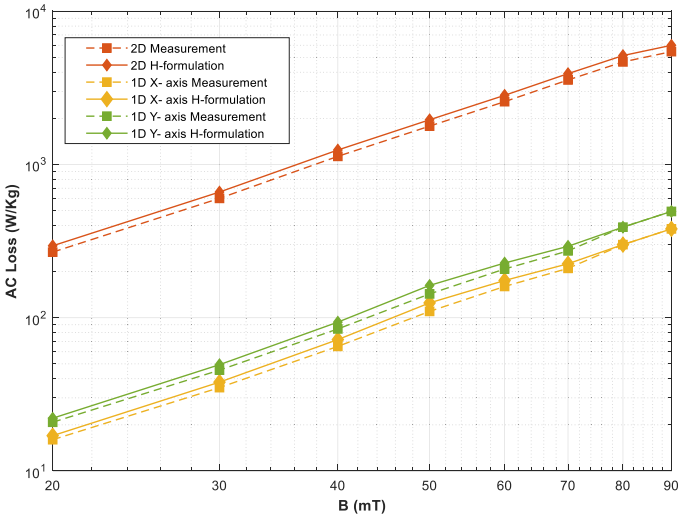

Figure 7.5. HTS AC loss variations at various alternating and rotating magnetic fields in specimen with thickness of 10mm.

When the HTS bulks are considered in the rotating machines, this loss will add a significant burden on the cooling system, which will ultimately affect the cryogenic efficiency of the application. Therefore, such rotating loss must be considered while designing such largescale applications. Moreover, the one-dimensional losses in X-axis and Y-axis differ from each other, which mainly relates to the traditional anisotropic behaviour of the HTS material.

As the rotating magnetic field is a main phenomenon in the rotating machines, the direction of the rotating magnetic field and the speed at which the magnetic field is rotating are also of significant importance when the HTS material needs to be characterised for the rotating applications. Figure. 7.6 shows the AC loss when the specimen is subjected to the rotating magnetic fields in clockwise and anticlockwise orientations. The increasing trend is similar in both of orientations, but there is also a slight difference in the case, which relates to the anisotropic nature of the HTS material. Figure 7.7 shows the loss variation with the frequency of the rotating magnetic field. In this case, a 20mT applied magnetic field rotates with a frequency of up to 200 Hz. The results show that AC power dissipation loss also increases significantly as the frequency of the applied magnetic fields is increased.

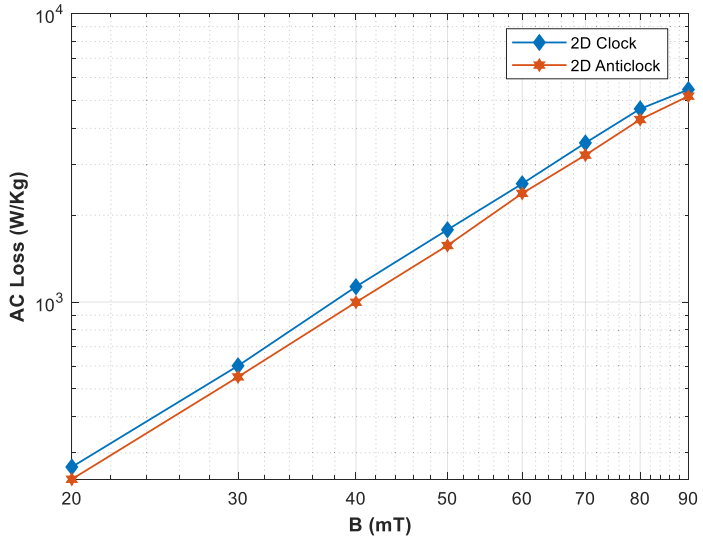

Figure 7.6. Comparison of measured AC loss subjected to rotating magnetic fields with clockwise and anticlockwise orientation in specimen with a thickness of 10mm.

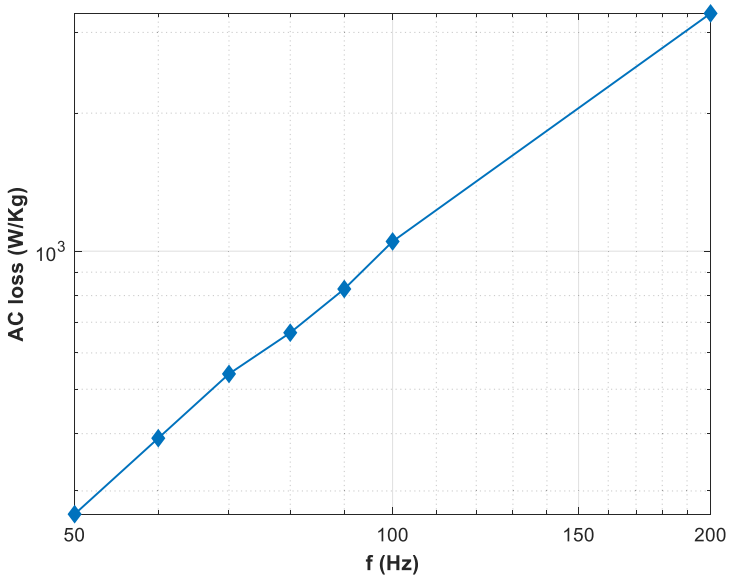

Figure 7.7. AC loss measured under rotating magnetic fields with multiple frequencies at 20mT in the specimen with thickness of 10mm

In order to compare the loss results with a different sample, The HTS specimen with 5mm thickness is also analysed in depth to understand its AC loss characteristics by exposing it to alternating and rotating magnetic flux density patterns with varying amplitudes and frequencies. Figure 7.8 displays a more comprehensive representation of the loss variations when the 5mm thick HTS sample is subjected to various alternating and rotating magnetic fields with a maximum strength of 80mT. it is worth noticing that the new 5mm thickness sample could only be magnetised until 80mT with the available testing system. Once again, to compare the loss under rotating excitations, one-dimensional loss measurements are also

performed. In this process, only the coils in specific orientations are activated to magnetise the sample along the X-axis or Y-axis, as outlined in Section 7.2. When the sample is exposed to higher magnetic fields, the loss under one-dimensional magnetic fields displays a typical increase. Additionally, the sample is subjected to various rotating magnetic fields in circular patterns, with both testing coils activated, as outlined in Section 7.2. The results reveal that the AC power dissipation loss under rotating magnetic fields is significantly higher than the AC loss under one-dimensional magnetic fields and increases logarithmically with higher amplitudes of the magnetic fields. The results from the two-dimensional experiments are also consistent with previous numerical studies.

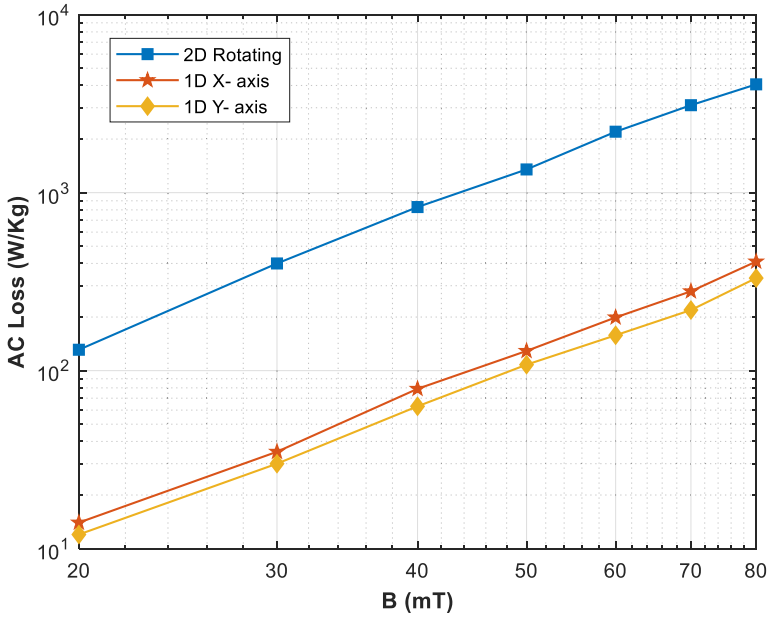

Figure 7.8: HTS AC loss variations at various alternating and rotating magnetic fields in specimen with thickness of 5 mm

Figure 7.9 presents a comparison of the AC loss for specimens with varying thicknesses when exposed to rotating magnetic fields of different magnitudes. The comparison demonstrates that the loss is noticeably higher in the sample with a thicker dimension, and the loss difference remains pronounced at higher levels of magnetisation. This comparison highlights the correlation between the specimen thickness and the AC loss when exposed to rotating magnetic fields, indicating that the thicker the specimen, the higher the AC loss. The results suggest that the AC loss increases as the magnitude of the rotating magnetic fields increases, and the difference in AC loss between the specimens with different thicknesses becomes even more pronounced as the magnetisation level increases.

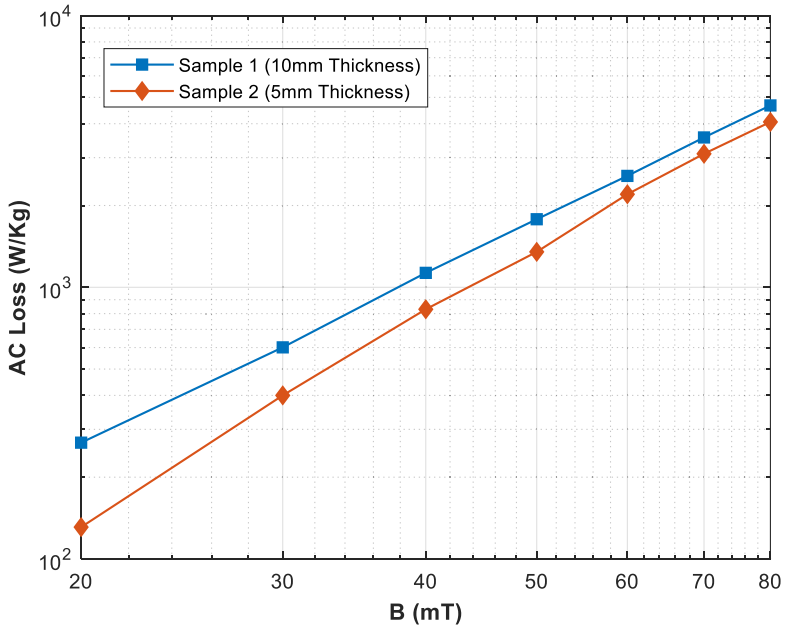

Figure 7.9. AC loss comparison of specimens with different thicknesses upon the exposure of a rotating magnetic field.

7.4 Conclusions

The measurement of AC loss is a crucial aspect of HTS characterisation. Most studies focus on the measurement and calculation of AC loss in one-dimensional (1D) alternating magnetic fields generated by either the transport current or external magnetic excitations. However, when HTS materials are integrated into rotating machines, they are subjected to rotating magnetic fields, which can contribute to AC loss. This additional AC loss can have a negative impact on the cryogenic cooling efficiency of HTS machines.

AC loss measurement is crucial for understanding the performance of HTS materials under different magnetic field conditions. In one-dimensional magnetic fields, the AC loss is primarily caused by the movement of the vortices within the superconductor. This movement creates friction and leads to the dissipation of the AC power, which is reflected in the AC loss measurement. However, when HTS materials are used in rotating machines, they are exposed to rotating magnetic fields, which can cause additional AC loss, which is not captured in one-dimensional measurements. The impact of rotating magnetic fields on AC loss can be significant and can affect the overall performance of HTS machines. The rotating magnetic fields can induce additional AC losses that are not captured in one-dimensional measurements. This additional AC loss can decrease the cryogenic cooling efficiency of the HTS machines, which can lead to reduced performance and increased energy consumption. Therefore, it is

important to consider the impact of rotating magnetic fields on AC loss when evaluating HTS materials for use in rotating machines.

This study provides a detailed investigation of the AC loss measurement under various scenarios. The results are compared with those from finite element-based H-formulation. A square bulk HTS sample is used for this investigation which is submerged in liquid nitrogen. The AC loss is obtained at circularly rotating flux density patterns of various amplitudes and is also compared with the AC loss under one-dimensional alternating flux density, where the rotating loss seems to be significantly higher. The loss variation has also been analysed at various frequencies, where a significantly increasing trend is observed as the frequency is increased up to 200 Hz. Furthermore, the AC loss is compared between two different specimens to examine the differences in loss due to specimen size. The comparison of AC loss between two specimens of different sizes provides valuable information about the relationship between specimen size and AC loss. This comparison can help to understand the influence of specimen size on AC loss and provide insights into how to optimise HTS material properties to minimise AC loss.

In comparing experimental results with calculated values for AC loss in high-temperature superconductors (HTS), discrepancies often arise due to various factors. These factors include deviations from idealized material properties, non-uniform magnetic field penetration, thermal effects, sample geometry and fabrication, and limitations in experimental measurements. The actual material properties of HTS may differ from the assumptions made in calculations, leading to higher losses in experiments. Non-uniform magnetic field distributions and temperature variations within the superconductor can further contribute to the observed discrepancies. Additionally, complex sample geometries and fabrication processes may impact the AC loss. Inherent limitations in experimental measurements, such as uncertainties in techniques, equipment, and environmental factors, can introduce errors. To enhance the agreement between experimental and calculated results, a comprehensive analysis of these factors is crucial, including refining theoretical models, optimizing experimental setups, considering additional loss mechanisms, and minimizing sources of error in measurements. Collaborative efforts and meticulous examination of the experimental setup can provide valuable insights into the specific reasons behind the observed discrepancies.

The results presented in this chapter offer a deeper understanding of the material characterisation of high-temperature superconductors (HTS). The findings indicate that the losses are significantly higher when the HTS specimens are exposed to rotating magnetic fields, as compared to one-dimensional alternating magnetic fields. This information is crucial for the

design of future large-scale HTS applications, where the additional power dissipation must be considered while planning the cryogenic cooling systems for these machines. The higher losses observed under rotating magnetic fields have important implications for the design of HTS systems and the optimisation of cryogenic cooling. The results of these studies can be used to determine the optimal HTS material properties and design, to minimize AC loss and improve the performance of HTS machines. This information is critical for the development of large-scale HTS applications, where the additional power dissipation could significantly affect the cryogenic cooling efficiency.

In addition, the results presented in this chapter provide valuable insights into the underlying mechanisms that contribute to AC loss in HTS materials. This information can be used to develop improved models for AC loss in HTS materials and to optimize the HTS material properties and design for minimum AC loss. The findings will also be beneficial for the optimisation of HTS materials and the design of cryogenic cooling systems to improve the performance of HTS machines and advance the development of HTS technology.

7.5 References

[7.1] P. Vanderbemden *et al.*, "Remagnetisation of bulk high-temperature superconductors subjected to crossed and rotating magnetic fields," *Superconductor science and technology,* vol. 20, no. 9, p. S174, 2007.

[7.2] M. Qiu, L. Z. Lin, G. M. Zhang, Y. S. Wang, and L. Y. Xiao, "Flux dynamic behavior inside HTS bulks under rotating magnetic field," *IEEE Transactions on Applied Superconductivity,* vol. 12, no. 1, pp. 1163-1166, 2002, doi: 10.1109/TASC.2002.1018608.

[7.3] M. Qiu, H. K. Huo, Z. Xu, D. Xia, and L. Z. Lin, "Electromagnetic phenomena in HTS bulk subjected to a rotating field," *IEEE Transactions on Applied Superconductivity,* vol. 14, no. 2, pp. 1898-1901, 2004, doi: 10.1109/TASC.2004.830923.

[7.4] W. A. Soomro, Y. Guo, H. Lu, J. Zhu, J. Jin, and B. Shen, "Three-Dimensional Numerical Characterisation of High-Temperature Superconductor Bulks Subjected to Rotating Magnetic Fields," *Energies,* vol. 15, no. 9, p. 3186, 2022. [7.Online]. Available: https://www.mdpi.com/1996-1073/15/9/3186.

[7.5] W. A. Soomro, Y. Guo, H. Lu, J. Jin, B. Shen, and J. Zhu, "Numerical Investigation of High-Temperature Superconducting-Coated-Conductors Subjected to Rotating Magnetic Fields," *Solids,* vol. 3, no. 4, pp. 569-577, 2022.

[7.6] W. A. Soomro, Y. Guo, H. Y. Lu, J. G. Zhu, J. X. Jin, and B. Shen, "Numerical Investigation of AC Loss in HTS Bulks Subjected to Rotating Magnetic Fields," in *2021 31st Australasian Universities Power Engineering Conference (AUPEC)*, 26-30 Sept. 2021 2021, pp. 1-5, doi: 10.1109/AUPEC52110.2021.9597734.

[7.7] H. Daffix and P. Tixador, "Electrical AC loss measurements in superconducting coils," *IEEE Transactions on Applied Superconductivity,* vol. 7, no. 2, pp. 286-289, 1997, doi: 10.1109/77.614486.

[7.8] *Superconductivity-Part 8: AC loss measurements. Total AC loss measurement of round superconducting wires exposed to a transverse alternating magnetic field at liquid helium temperature by a pickup coil method* (IEC Std. 61788-8, 2010, 2nd ed.). 2010.

[7.9] H. Huang, C. Zhang, and S. Yan, "Calorimetric measurement of AC losses of superconducting magnet," *Acta Physica Temperature Humilis Sinica,* vol. 3, no. 1, pp. 42-46, 1981.

[7.10] W. A. Soomro, Y. Guo, H. Lu, J. Jin, B. Shen, and J. Zhu, "Experimental Setup for Measurement of AC Loss in HTS under Rotating Magnetic Field," *Energies,* vol. 15, no. 21, p. 7857, 2022.

CHAPTER 8 **Conclusions, Challenges and Future Works**

8.1 Conclusions

The measurement of AC loss is one of the most significant aspects of the High-Temperature Superconductor (HTS) characterisation. Most investigations concentrate on AC loss measurement and calculation in one-dimensional (1D) alternating magnetic fields created by either the transport current or by external magnetic excitations. However, when the HTS materials are incorporated into the rotating machines, they are exposed to the rotating magnetic fields. This exposure could complement the AC loss, which will ultimately affect the cryogenic cooling efficiency of the HTS machines. In this study, the properties of HTS materials, particularly the AC loss, have been investigated under the rotating magnetic field. The main investigations of this thesis are listed as follows:

1- Analysis and characterisation of the basic electromagnetic properties of HTS bulk using numerical modelling techniques under the exposure of rotating magnetic field in XOY, XOZ and YOZ planes. The typical current density distribution J for all three components (J_x; J_y; J_z) and AC loss distribution is presented. The demagnetisation subjected to similar rotating fields is also investigated to see how the HTS-trapped field magnets are demonised. This electromagnetic data presented in this study will provide a comprehensive understating of the material properties of HTS when subjected to rotating magnetic fields.
2- A systematic investigation of AC loss is performed by numerical modelling technique based on FEA and H-formulation when an HTS bulk sample is subjected to various alternating and rotating flux density patterns up to 2 T.
3- The electromagnetic behaviour of HTS CCs using numerical modelling techniques by applying rotating magnetic fields to the stack of HTS CCs. A homogenous bulk model is created to consider the finite-size effects. The model predicts the behaviour of AC loss under rotating magnetic fields of various amplitudes, along with the current transport situation. Coloured maps of flux density distribution are also presented as the reference to show the actual distribution of magnetic flux density in various timesteps and transport currents.

4- The AC loss measurement is, no doubt, one of the most important aspects of the HTS characterisation. The existing methods only focus on loss measurement under one-dimensional (1D) alternating magnetic fields generated by the transport current in the HTS material itself or through external excitations. However, with the limitations in the existing measurement systems, it is impossible to investigate the AC loss under the exposure of rotating magnetic fields. This thesis presents a new experimental setup in order to measure the AC loss in HTS material upon exposure to the rotating magnetic field. The experimental results show consistency with the modelling results. This method will be helpful in the further characterisation of HTS material, especially under the rotating magnetic fields, in order to design large scarce HTS applications.
5- A detailed investigation of the AC loss measurement under various scenarios. The results are compared with those from finite element-based H-formulation. Two square bulk HTS samples are used for this investigation which are submerged in liquid nitrogen. The AC loss is obtained at circularly rotating flux density patterns of various amplitudes and is also compared with the AC loss under one-dimensional alternating flux density. The loss variation has also been analysed at various frequencies, where a significantly increasing trend is observed as the frequency is increased up to 200 Hz. The results presented in this thesis showcase further insights into the material characterisation, which shows that the losses are actually higher in the case of exposure under rotating magnetic fields. These results will be beneficial for the design of future large-scale HTS applications, where the additional power dissipation could be considered while planning the cryogenic cooling systems for such machines.

8.2 Challenges

HTS material is a relatively new field of research that has gained a lot of attention in recent years due to its potential for revolutionising various applications ranging from power transmission to medical imaging. Despite its potential, the characterisation of HTS materials is challenging and requires specialised equipment, resources, and expertise. At the University of Technology Sydney (UTS), this research was conducted for the first time worldwide, and it has been a challenging journey to establish a robust HTS material characterisation process.

One of the major challenges in HTS material characterisation is the limited availability of resources, both in terms of equipment and materials. HTS materials are expensive, and there is limited availability of these materials, making it difficult to obtain them for research

purposes. Additionally, the specialised equipment required to perform HTS characterisation is also limited, and in some cases, it may not be readily available at the university. This has led to the need to develop innovative solutions to overcome these resource constraints.

Another significant challenge in HTS material characterisation is the experimental feasibility, which involves the safe handling of liquid nitrogen (LN2) used in the cooling process. LN2 is extremely cold, and its handling requires specialised safety procedures, which were developed and approved by the authorities at UTS. The safety procedures involved in HTS material characterisation also include the storage, transport, and decanting of liquid nitrogen, which is time-consuming and requires specialised training.

The HTS material characterisation process is also time-consuming due to the need for precise measurements and the cryogenic cooling of the sample. The HTS materials must be kept at very low temperatures for proper characterisation, which can take several hours or even days. This prolonged cooling process adds to the time required to perform the HTS material characterisation.

To sum up, the characterisation of HTS materials is a challenging task that requires specialised equipment, resources, and expertise. At UTS, this research is being performed for the first time worldwide, and the researchers have faced several challenges along the way, including limited availability of resources, experimental feasibility, and time-consuming cooling processes. Despite these challenges, we have overcome these obstacles by developing innovative solutions and establishing safety procedures approved by the authorities. These results provide a foundation for further research in the field of HTS materials and their characterisation, which may have a significant impact on various applications in the future.

8.3 Future Works

HTS materials are a relatively new field of research and are attracting increasing attention from scientists and engineers. Despite the great advances that have been made in recent years, there is still much to learn about these materials, especially with respect to their performance under rotating magnetic fields. In this essay, we will explore some of the key areas of research that are likely to be of interest in the future of HTS material characterisation.

1. One of the major challenges in HTS material characterisation is understanding the behaviour of different types of materials. Currently, HTS materials come in two main forms: bulks and tapes. Bulks are typically large pieces of HTS material that are used

to make electromagnets, while tapes are thin strips that are used to make power transmission cables. Both types of HTS materials have their own unique set of properties, and it is important to study these materials under rotating magnetic fields in more detail so that we can better understand their performance under rotating magnetic fields.

2. Another area of future research is the study of HTS materials under higher rotating magnetic fields. Currently, the experimental studies performed in this thesis are at magnetic fields of around 90mT, due to experimental and resource constraints. But there is a need to study the performance of HTS materials at much higher magnetic fields. This will allow us to better understand these materials' limits and determine whether they can be used in high-power applications.

3. Another important area of research is the study of HTS materials under different frequencies. It is important to study the behaviour of HTS materials at different frequencies so that we can better understand their performance. This will also allow us to determine whether HTS materials can be used in applications that require higher frequencies.

4. Finally, another area of future research is the study of HTS materials under 3D rotating magnetic fields. Currently, some studies have been performed under two-dimensional rotating magnetic fields, but there is a need to study the behaviour of HTS materials under 3D rotating magnetic fields. This will allow us to better understand the behaviour of these materials in more complex magnetic environments and to determine whether they can be used in applications that require 3D rotating magnetic fields.

In conclusion, the study of HTS materials under rotating magnetic fields may be a rapidly growing area of research. There is still much to learn about these materials, and the study of different types of materials, higher magnetic fields, different frequencies, and 3D rotating magnetic fields is likely to be of great interest in the future. With the right investment in research and development, HTS materials could play a significant role in a variety of high-power applications and could revolutionise the way we think about the design of future large-scale HTS applications.

The End